Alma Mater Studiorum – Università di Bologna

DOTTORATO DI RICERCA IN

FISICA

Ciclo 36

Settore Concorsuale: 02/B1 – FISICA SPERIMENTALE DELLA MATERIA

Settore Scientifico Disciplinare: FIS/03 – FISICA DELLA MATERIA

KINETICS OF PHOTOGENERATED CARRIERS IN NANOSTRUCTURED SEMICONDUCTOR HETEROJUNCTIONS FOR SOLAR WATER SPLITTING

Presentata da: Pierpaolo Vecchi

Coordinatore Dottorato

Prof. Alessandro Gabrielli

Supervisore

Prof. Luca Pasquini

Co-supervisore

Dr. Raffaello Mazzaro

Esame finale anno 2024

Abstract

This thesis aims to investigate the fundamental processes governing the performance of different types of photoelectrodes used in photoelectrochemical (PEC) applications, such as unbiased water splitting for hydrogen production. Unraveling the transport and recombination phenomena at a semiconductor/electrolyte interface is certainly not trivial, especially when dealing with nanostructured and surface-modified heterojunctions. To approach this difficult task, the work presented here first focus on a much simpler system, consisting of a hydrogen-terminated p-silicon photocathode in acetonitrile, that can be considered as a standard reference case for PEC studies. This interface was able to provide access to all four bias conditions, i.e., accumulation, flat band, depletion, and inversion, predicted by the Schockley-Read-Hall model. Steady-state and time-resolved excitation at long wavelength provided clear evidence of the formation of an inversion layer and revealed that the most optimal photovoltage, as well as the longest electron – hole pair lifetime occurs when the reduction potential for the species in solution lies within the unfilled conduction band states. Understanding more complex systems is not as straight-forward and a complete characterization that combine time- and frequency-resolved techniques is needed to deconvolve the intricate charge carrier kinetics inside the photoelectrode. Intensity modulated photocurrent spectroscopy and transient absorption spectroscopy are used here on WO_3/$BiVO_4$ heterojunctions whose surface was modified by Co-Fe based overlayers. First, by selectively probing the two layers of the heterojunction, the occurrence of interfacial recombination is identified. Then, the addition of the overlayer resulted in passivation of surface states and charge storage at the active sites in cobalt atoms, resulting in suppression of recombination in time scales that go from picoseconds to seconds and higher charge separation efficiency. Finally, the charge carrier kinetics of several different Cu(In,Ga)Se_2 (CIGS)-based architectures used for water reduction was investigated by intensity modulated photocurrent spectroscopy. The CIGS absorber layer used as a photovoltaic cell or as a photocathode in solution exhibits the same absorption and charge generation properties, but the efficiency of the PEC system

is severely limited by charge transfer from the surface to the solution. A NiMo binary alloy is deposited on the CIGS photocathode surface, showing a remarkable enhancement in the transfer rate of electrons in solution, that makes this electrocatalyst for hydrogen evolution a valid competitor of rare-earth-based catalysts. An additional device using a NiMo dark cathode assisted by an external CIGS photovoltaic module displayed the optimal absorption and charge separation properties of the heterostructure and a highly performing interface with the solution given by the electrocatalyst. The complete characterization of the proposed nanostructured heterojunctions allows to combine their unique PEC properties with the appropriate surface modification to enhance the performance and reach more efficient unbiased solar water splitting.

Contents

List of Abbreviations

AC	alternating current
AM 1.5G	air mass 1.5 global
AZO	aluminum doped zinc oxide
bpy	2,2'-bipyridine
CB	conduction band
CIGS	Cu(In,Ga)Se2
CPE	constant phase element
CSE	charge separation efficiency
CT	charge transfer
DC	direct current
DRT	distribution of relaxation times
ECSA	electrochemically active surface area
EIS	electrochemical impedance spectroscopy
EQE	external quantum efficiency
FESEM	field emission scanning electron microscopy
FF	fill factor
FLP	Fermi-level pinning
FRA	frequency response analyzer
FTO	fluorine-doped tin oxide
FWHM	full width at half maximum
GC	glassy carbon
GL-DRT	gaussian Lasso distribution of relaxation times
HER	hydrogen evolution reaction
HRTEM	high-resolution transmission electron microscopy
IBG	intra bandgap
IMPS	intensity modulated photocurrent spectroscopy
IPCE	incident photon-to-current conversion efficiency
IR	infrared
KWW	Kohlrausch-Williams-Watts
L-DRT	Lasso distribution of relaxation times
LED	light-emitting diode
LFP	laser flash-photolysis
LHE	light harvesting efficiency
LSV	linear sweep voltammetry
MOSFET	metal-oxide-semiconductor field-effect transistor
MV	methyl viologen
OCP	open circuit potential
OER	oxygen evolution reaction
PB	Prussian blue
PC	photocatalysis
PEC	photoelectrochemical
PMT	photomultiplier tube
PV	photovoltaic
PV-E	photovoltaic assisting electrolyser
RCM	rate constant model

RHE	reversible hydrogen electrode
SCL	space-charge layer
SRH	Schockley-Read-Hall
STH	solar-to-hydrogen
TAS	transient absorption spectroscopy
TBA	tetrabutylammonium
TE	transfer efficiency
TRIR	time resolved infrared
UV	ultraviolet
VB	valence band
WD-IMPS	wavelength-dependent intensity modulated photocurrent spectroscopy
XRD	X-ray diffraction

Introduction

1.1 Background and Motivations

The growing global demand for sustainable, carbon-neutral energy sources has sparked extensive research into renewable technologies, offering an alternative to the excessive consumption of fossil fuels in today's rapidly expanding world economy.[1] Solar energy stands out as the ultimate renewable resource, with the Earth receiving approximately 120,000 TW of solar irradiation annually, surpassing the total energy consumption of the world.[2] While photovoltaic (PV) systems are the most widely used solar technology for converting sunlight into electricity,[3] solar energy faces a challenge due to its intermittent nature, necessitating the development of efficient and continuous power supply technologies.

Hydrogen gas (H_2) plays a vital role in the renewable energy landscape due to its CO_2-free combustion and high gravimetric energy density (141.9 MJ kg^{-1}). However, over 90% of the current H2 production comes from fossil fuels, primarily steam methane reforming.[4] Solar water splitting has emerged as a promising method for clean and efficient hydrogen production since the pioneering work of Fujishima and Honda in 1972.[5] This process harnesses solar energy to decompose water into hydrogen and oxygen through an electrochemical process, offering a way to store renewable energy as chemical bonds. Solar water splitting can occur through three configurations: photocatalysis (PC), an electrolyser assisted by a PV module (PV-E), and photoelectrochemical (PEC) water splitting (Figure 1.1).

In PC water splitting (Figure 1.1a), suspended semiconductor powders like TiO_2 or $SrTiO_3$ in an aqueous solution absorb sunlight, generating charge carriers that drive water reduction and oxidation reactions.[6–8] However, this method's main limitation lies in the semiconductor's need to drive both reactions, leading to a low solar-to-hydrogen (STH) conversion efficiency due to limited absorption

of wavelengths beyond 400 nm and challenges in separating H_2 and O_2 gases produced in the same colloidal suspension.

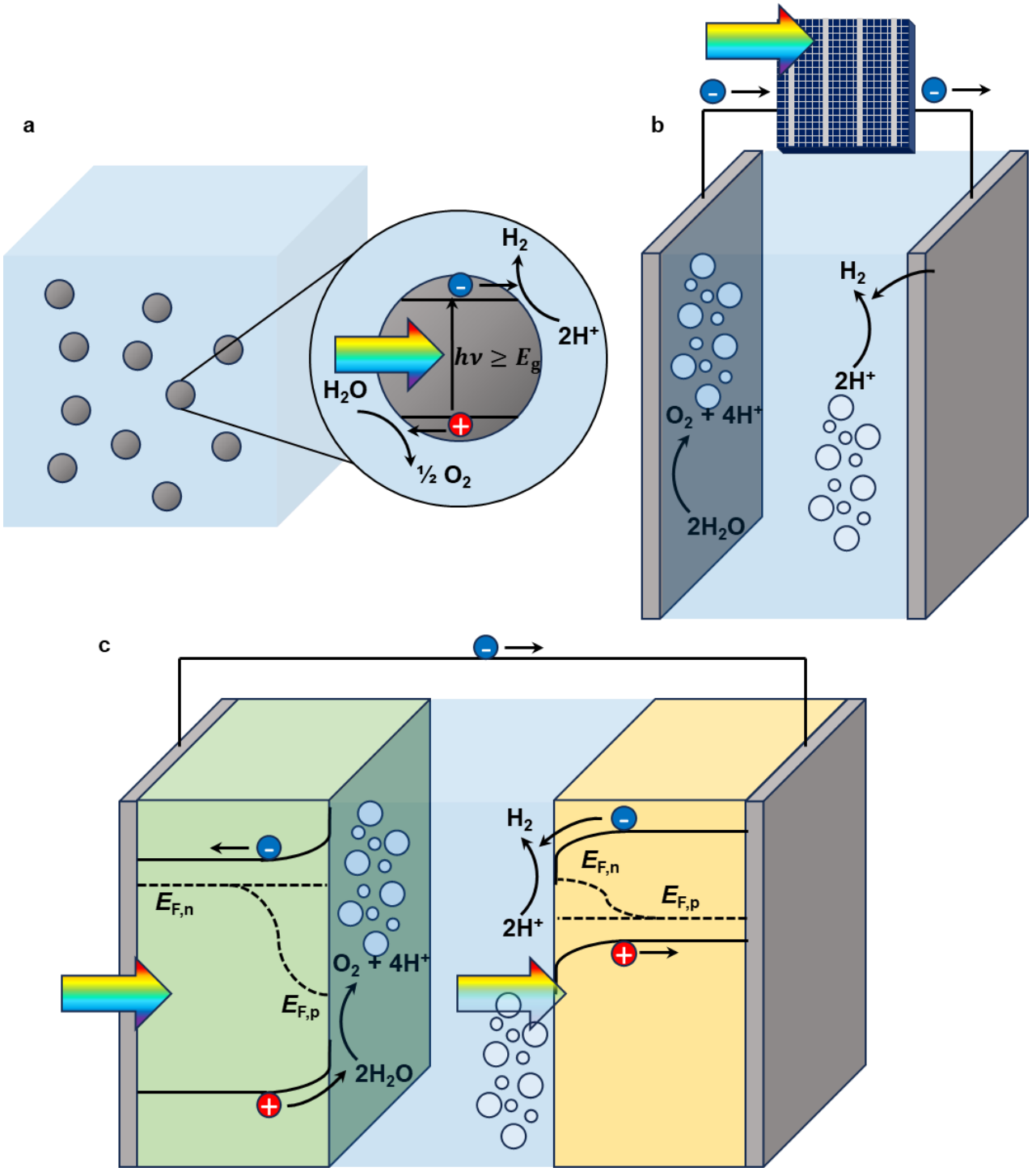

Figure 1.1: *Schematic of the three possible configurations for solar water splitting: a) photocatalysis, b) electrolyser assisted by a photovoltaic cell, c) photoelectrochemical water splitting*

PV-E water splitting (Figure 1.1b) offers higher STH efficiency than PC water splitting. By integrating commercial PV modules with electrolysers, hydrogen production systems can be easily scaled up.[9] Nevertheless, the high costs associated with PV modules and electrolysers make PV-E water splitting less economically viable than steam methane reforming.

PEC water splitting (Figure 1.1c) presents several advantages, including high theoretical STH efficiency, simple fabrication, product separation, and low overall cost.[10–12] In PEC, two semiconducting photoelectrodes generate hydrogen and oxygen gases at the photocathode and photoanode, respectively, avoiding explosive H_2/O_2 mixtures and reducing device complexity and cost by integrating the light absorber and catalyst.

The pursuit of efficient and economically viable photoelectrodes lies at the core of PEC water splitting research. Various semiconductor materials have been explored, ranging from simple single-junction materials to more complex nanostructured heterojunctions, to optimize the absorption of solar photons and enhance charge separation and transport properties. Additionally, the incorporation of co-catalysts and modifying agents has shown great potential to improve the overall efficiency of the process. However, no single photoelectrode has been able to drive overall water splitting with a high STH efficiency. In fact, wide bandgap photoelectrodes offer a good onset potential but low photocurrent, while photoelectrodes with narrow bandgaps show high photocurrent, but insufficient driving force to lower the onset potential for the reaction. Therefore, external electric energy is still needed to accomplish water splitting. Other candidates for the next-generation technology in solar water splitting consist of two photoelectrodes with different bandgaps, a photoanode and a photocathode, that drive separately the oxygen evolution reaction (OER) and hydrogen evolution reaction (HER), respectively, allowing to reach unbiased water splitting.[10,11]

Despite its promise, PEC water splitting faces challenges, such as the need for photoelectrodes with tunable bandgaps, high stability, and low recombination rates to efficiently utilize solar energy.

Additionally, cost-effective and scalable manufacturing processes are crucial for large-scale deployment of this technology.

1.2 Fundamentals of photoelectrochemical cells for unbiased water splitting

Water splitting is a reaction that requires a standard free energy change ΔG of 237.2 kJ mol^{-1} or a 1.23 eV per electron to split one molecule into H_2 and ½ O_2 under standard conditions.[13,14] The water splitting reaction in acidic media is described by the following Equations:

$$4H^+ + 4e^- \rightarrow 2H_2 \quad (1.1)$$

$$2H_2O \rightarrow O_2 + 4H^+ + 4e^- \quad (1.2)$$

while the water splitting reaction in alkaline media is:

$$4H_2O + 4e^- \rightarrow 2H_2 + 4OH^- \quad (1.3)$$

$$4OH^- \rightarrow O_2 + 4H_2O + 4e^- \quad (1.4)$$

Here, Equations 1.1 and 1.3 describe the HER, while Equations 1.2 and 1.4 describe the OER.

In solar-driven water splitting, the semiconductor needs to satisfy several criteria: (i) the bandgap needs to be larger than 1.23 eV, (ii) the generated photovoltage needs to be larger than 1.23 eV, and (iii) the conduction band energy E_{CB} and the valence band energy E_{VB} must span the electrochemical potentials of the HER ($E°(H^+/H_2)$) and the OER, ($E°(O_2/H_2O)$) to achieve unassisted solar water splitting.[15] Using two individual photoelectrodes (photoanode and photocathode) is a favorable way to achieve co-evolution of H_2 and O_2, and surface modification with catalysts also has a crucial role in accelerating the surface reaction kinetics of solar water splitting.[16]

When using PEC cells for unbiased water splitting, the combined photovoltage generated by the two photoelectrodes must exceed the thermodynamic water splitting voltage of 1.23 V and the additional overpotential to account for kinetic losses. To obtain the STH efficiency η_{STH}, one should characterize

independently the photoanode and the photocathode in a three-electrode configuration and measure the photocurrent-voltage (j/V) curve (Figure 1.2). From the intersection of the two curves, one can estimate the efficiency as:

$$\eta_{\mathrm{STH}} = \frac{j_{\mathrm{op}} \times 1.23\ \mathrm{V} \times \eta_{\mathrm{F}}}{P_{\mathrm{in}}} \tag{1.5}$$

where P_{in} is the power density of the incident light, which is usually the air mass 1.5 global (AM 1.5G) solar spectrum with 100 mW cm^{-2}, j_{op} is the intersection in current density of the two j/V curves, and η_{F} is the Faradaic efficiency of the reaction.

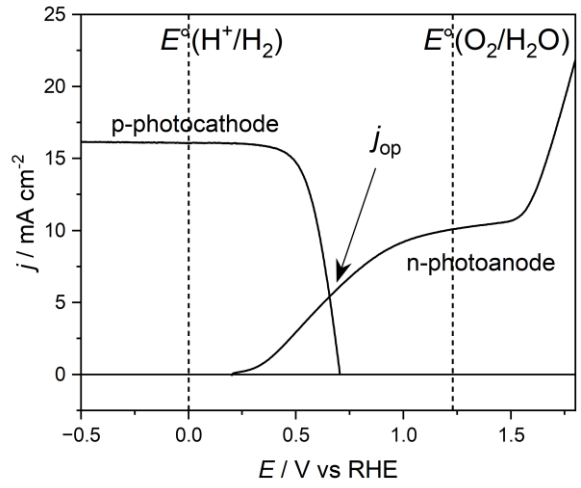

Figure 1.2: *Overlaid photocurrent density-potential characteristic of a p-type photocathode and an n-type photoanode.*

The Schockley-Queisser limit predicts using detailed equilibrium principles the maximum theoretical efficiency of single-junction solar cells at about 30%,[17] while it reaches a value of 42% for tandem solar cells.[18] The tandem structure has attracted a lot of attention for the same reason also for solar water splitting devices, to pursue higher STH efficiency and to overcome the voltage limitations of a single photoelectrode. When designing a tandem cell for unbiased water splitting, usually a wide bandgap photoanode is coupled with a narrow bandgap photocathode, and the matching of the two bandgaps is a crucial factor to consider.[19,20] In fact, the incident light initially passes through the

front photoelectrode and then reaches the back photoelectrode (Figure 1.1c), so different wavelengths are absorbed by the two materials. The predicted maximum STH efficiency is around 29.7% for a bandgap combination of 1.60 eV/0.95 eV,[10] while another work estimated a value of 28.9% considering overpotential and light absorption of water.[12] The STH efficiency for PEC tandem cells measured from experiments is still far below its theoretical maximum and this discrepancy is explained by several factors: poor activity of the photoelectrodes, slow kinetics at the surface, light loss and voltage drop at the ion-selective membrane that separates the anodic and cathodic compartments, ion mass transport losses in the electrolyte, and parasitic light absorption of water. The aim of this thesis is to investigate the kinetics processes of the photogenerated charges that limit the efficiency of a PEC system for unbiased water splitting.

1.3 Overview of the thesis

The efficiency of a PEC cell greatly depends on the performance of each photoelectrode, so extensive research has been done on tandem cells that are decoupled into two photoelectrodes for independent optimization. This thesis shows a complete characterization of several systems that can be used as photoelectrodes in a PEC tandem cells and is structured as follows: chapter 2 describes the materials studied in this thesis, introduces the concept of an ideal interface, shows different alternatives for photoelectrodes in a real working device and their limitations and strategies to improve their efficiency, including surface modification with cocatalysts; chapter 3 describes transient absorption spectroscopy (TAS) and intensity modulated photocurrent spectroscopy (IMPS) and shows how time- and frequency-resolved techniques can provide an in depth understanding of the kinetics of photogenerated carriers at the electrode/electrolyte junction over a considerable time span, in particular using a Lasso regression on the distribution of relaxation times[21] of the system to deconvolve bulk and surface processes at the semiconductor/electrolyte junction; chapter 4 presents the results of a PEC characterization of H-terminated p-Si photocathodes in acetonitrile, that shows evidence of inversion conditions resulting in large photovoltages for multi-electron transfer;[22]

chapter 5 shows a complete structural, optical and photoelectrochemical characterization of a $WO_3/BiVO_4$ heterojunction and highlights efficiency losses at the interface between the two semiconductors by means of wavelength-dependent IMPS;[23] in chapter 6, the effect of CoFe mixed overlayers on the kinetics of the $WO_3/BiVO_4$ heterojunction is explored with an *operando* TAS and IMPS study, which demonstrated that this type of surface modification enables charge separation efficiency enhancement and suppression of recombination;[23] finally, chapter 7 presents an innovative IMPS study involving different CIGS-based architectures to drive the hydrogen evolution reaction, in particular emphasizing how the performance of the same absorber material operating as a photocathode immersed in an electrolytic solution is greatly limited compared to when it is used as an external photovoltaic cell assisting a dark cathode.

2 Semiconductors for water splitting

In tandem PEC cells, the performance of each photoelectrode significantly influences the STH efficiency, as depicted in Figure 1.2. The onset potential, saturated photocurrent, and fill factor are key parameters in the photoelectrode evaluation, and extensive studies have focused on how to improve these properties in several photoelectrodes.

Typically, photoanodes usually employ n-type semiconductors, where photogenerated holes migrate from the bulk to the surface and drive the OER. This step is considered the bottleneck for water splitting, as generating one oxygen molecule requires four electron-proton coupling reactions, which usually have sluggish kinetics. $BiVO_4$, Fe_2O_3, TiO_2, WO_3, and ZnO are widely investigated photoanodes for water oxidation.[24] Despite their impressive theoretical efficiencies, practical experiments reveal low photocurrent and onset potential, limiting the efficiency of the photoanode.

In tandem PEC cells, p-type semiconductors have a critical role as the back photocathode. Common materials for photocathodes are narrow bandgap semiconductors, such as amorphous and crystalline silicon, chalcopyrite ($Cu(In,Ga)Se_2$, $CuInS_2$), Cu_2O, and perovskite. Here, band bending facilitates efficient electron extraction, which is essential to achieve efficient charge separation and transfer at the semiconductor/electrolyte junction. However, a significant challenge lies in achieving large photovoltages, which are usually limited by low-energy band bending.[25]

The next sections delve further into the materials investigated in this thesis. It starts by exploring the concept of an ideal interface for fundamental studies in electrochemistry, focusing on hydrogen-terminated p-silicon in acetonitrile. Shifting the research focus toward nanostructured photoelectrodes, the following sections describe two heterojunctions: a $WO_3/BiVO_4$ heterojunction for the anodic compartment and a chalcopyrite-based photocathode, $Cu(In,Ga)Se_2$ (CIGS), forming an heterojunction with CdS for the cathodic compartment. The chapter concludes with an overview

of catalysts for oxygen and hydrogen evolution, with a focus on cobalt and iron-based overlayers and on nickel-molybdenum binary alloys.

2.1 Hydrogen terminated p-silicon in acetonitrile as an ideal interface

Among the semiconductors used for PEC water splitting, silicon has appeared as one of the most promising candidates because of its abundance and small bandgap of 1.1 eV that gives the ability to harvest photons from a large portion of the solar spectrum. In the 1970s, devices based on silicon/electrolyte junctions were developed in order to convert light to electricity and for the photogeneration of storable chemical fuels in the form of electrolytic products. The integrity of the silicon surface has been the main focus during the development of these devices, as its degradation leads to severe decrease in efficiency.

Regarding the OER, n-type Si can be used as photoanode, but its surface undergoes anodic degradation under operating conditions. On the other hand, p-Si employed as photocathode for the HER does not undergo the formation of silicon oxides, as it operates under reductive conditions and in strongly acidic solutions. The position of the conduction band edge of p-type Si is not only favorable relatively to the H^+/H_2 redox potential, but also to different proton-assisted multielectron reduction potentials for CO_2. In alkaline solutions the dissolution of Si becomes more significant and proper protection is required for developing stable and high-performance p-Si photocathodes.

A strategy that is generally useful in elucidating the basic processes at the silicon/electrolyte interface is the use of non-aqueous liquid phases, as the poorer solvating properties of these solvents typically lead to greater electrode stability. Non-aqueous solutions offer many advantages in carrying out and understanding simple electrochemical processes, such as an extended range of available potentials, the possibility to explore numerous reversible one-electron transfer reactions without kinetic complications, and fewer difficulties with surface phenomena.

2.1.1 Physics of semiconductor/liquid contacts

For brevity only a lowly doped p-type semiconductor is described in this section, but the same description could be used on an n-type semiconductor. Figure 2.1a shows the energy band diagram of the semiconductor before equilibrium with the solution, where E_{VB}, E_{CB}, and E_F are the energy of the valence band maximum, of the conduction band minimum, and of the Fermi level, respectively. The energy bandgap E_g is given by the difference between E_{CB} and E_{VB}. The electrolyte solution contains a redox couple (consisting of the acceptor A^+ and the donor A) having electrochemical potential $-qE°(A^+/A)$, where $E°$ is the Nernst potential of the redox pair (A^+/A). When the solid is placed in contact with the solution (Figure 2.1b) a net interfacial charge transfer occurs between the two phases, as the Fermi level (E_F) of the electrode align with the redox potential of the solution. A space-charge layer (SCL) is generated in the silicon close to the interface, resulting in an excess negative charge, arising from the ionized dopant atoms in the semiconductor, while the solution has an excess of positive charge, and the potential drop is in the thin (< 10 Å) Helmholtz layer. The thickness of the SCL, *W*, increases with diminishing doping level and is on the order of 10 nm – 1 μm for non-degenerate semiconductors (10^{14} – 10^{18} atoms cm^{-3}). Under these conditions of equilibrium, the band bending presents an effective barrier with height $q\phi_B$ that prevents the flow of majority carriers (holes) from the semiconductor to the electrolyte, and small faradaic currents are observed. By applying a potential, it is possible to change the potential drop across the solid: a positive bias will decrease the amount of band bending, until the flatband potential E_{FB} is reached. An applied bias more positive than E_{FB} produces a surface accumulation layer, that results in rapid interfacial charge transfer via majority carriers, similar to what is observed at a metal/electrolyte interface.

2.1.2 Energetics of semiconductor/liquid junctions under illumination

The free energy produced by a semiconductor/electrolyte junction does not reach the theoretical energy limit dictated by the interfacial energetics discussed above. Instead, it depends on the kinetics of the charge carriers in the photostationary state that results after illumination of the

semiconductor/electrolyte interface with photons of energy greater than the bandgap (E_g). In solid-state physics, the free energy is given by the difference between hole and electron quasi-Fermi levels ($E_{F,p}$ and $E_{F,n}$) under illumination (Figure 2.1c). These energy levels are just a description of the electrochemical potential of one carrier type at a time under non-equilibrium conditions (in this case, under illumination), using Fermi – Dirac statistics to describe separately the populations of electrons and of holes. The degree of splitting between the two quasi-Fermi levels is the photovoltage (V_{ph}) generated by the junction and it determines the photoelectrochemical reaction driven by the system.

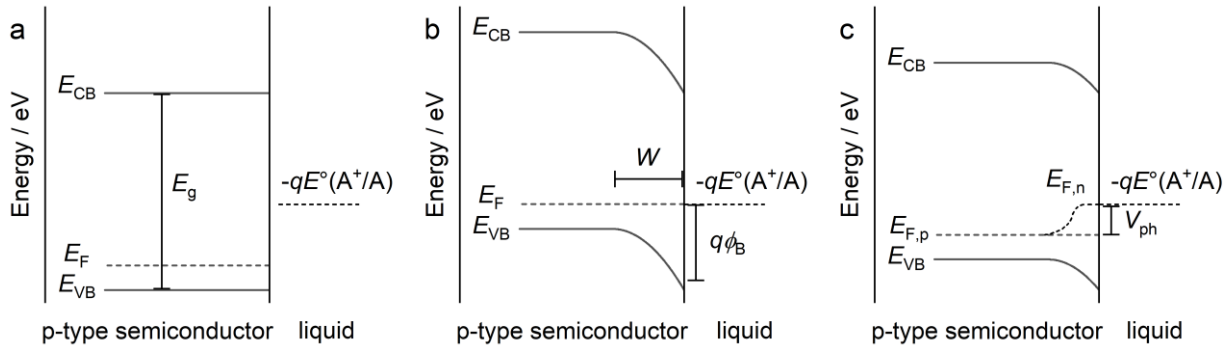

Figure 2.1: *Band energetics of a semiconductor/liquid contact in three cases: a) before equilibration between the two phases; b) after equilibration, but in the dark; c) in quasi-static equilibrium under steady-state illumination. In b) $q\phi_B$ is the barrier height, and its magnitude determines the theoretical maximum energy that can be extracted from a separated electron-hole pair at the junction. In c), where steady-state illumination yields non-equilibrium electron and hole populations, $E_{F,n}$ is the electron quasi-Fermi level and $E_{F,p}$ is the hole quasi-Fermi level. The voltage generated by the junction under illumination V_{ph} is given by the difference between – $qE°(A^+/A)$ and $E_{F,p}$.*

2.1.3 Non-ideal behavior

Surface states is a term that usually refers to localized states whose energy is in the forbidden bandgap of the semiconductor. The presence of these intra bandgap (IBG) states results in non-ideal behaviors that can limit the efficiency of the system, as they promote surface recombination processes, charge storage and trapping. For example, a thin layer of silicon dioxide (SiO_2) on native silicon is responsible for introducing surface defects that limit the PEC performance of Si photocathodes.[26] Understanding and controlling the relevant kinetic processes that affect the photovoltage is essential

in the design of efficient semiconductor photoelectrodes. These kinetic processes govern the respective electron and hole concentrations at the interface under quasi-equilibrium conditions and can be summarized in: (i) recombination in the bulk, (ii) recombination in the depletion region, (iii) tunneling through the electric potential barrier near the surface, (iv) thermionic emission, that allows to thermally surmount the interfacial potential barrier, and (v) recombination at defects at the semiconductor/liquid interface. For well-surface passivated silicon single crystals, all these mechanisms can be suppressed except for bulk recombination, while in other cases surface recombination and charge transfer across the interface dominates the recombination processes.

In 1986, researchers at Bell Labs reported that a hydrofluoric acid etch of a Si(111) crystal provided a surface that was remarkably inactive from an electronic point of view – by removal, or passivation, of surface states.[27] Infrared spectroscopy revealed that the surface was terminated with Si-H bonds that were stable in air for minutes.[28] The H-termination maintained the tetrahedral coordination of the Si atoms and removed the "dangling bonds" that serve as recombination centers for photogenerated electron-hole pairs.[28,29] Indeed, the surface recombination velocity reported in this seminal work was the lowest ever measured[27] and since then hydrogen-terminated silicon has become a "standard" in surface science studies. A review of the photoelectrochemical literature reveals that such ideal electronic interfaces have received surprisingly little attention for multi-electron transfer catalysis even though they have enabled high efficiencies in regenerative solar cells based on one-electron redox mediators.[30,31]

The hydrogen-terminated p-silicon/acetonitrile interface serves as an indispensable reference case for photoelectrochemical studies due to its simplicity and versatility. Unlike other types of photoelectrodes, this ideal interface lacks the complexity associated with surface or interfacial defects. Consequently, it provides a clearer and more straightforward understanding of the fundamental charge carrier kinetics at the semiconductor-electrolyte interface described in Figure 2.1. Furthermore, the absence of a catalyst in this system allows for a direct assessment of the

semiconductor's intrinsic photoelectrochemical properties. This reference case provides a baseline for evaluating the performance of other photoelectrodes and highlights the importance of controlling surface morphology and passivation in achieving high photoelectrochemical efficiency. Despite the benefits of this interface, its practical implementation in large-scale photoelectrochemical water splitting devices faces limitations in terms of efficiency and scalability and introduce the necessity to explore alternative materials.

To address these limitations, the research presented in this thesis also focuses on nanostructured photoelectrodes, such as $WO_3/BiVO_4$ photoanodes and CIGS/CdS photocathodes. These heterojunctions offer unique advantages, including enhanced light absorption, improved charge carrier separation, and tailored band alignment, which can lead to increased PEC performances. However, the presence of surface and interfacial defects in these nanostructured systems also introduces additional complexities, requiring innovative approaches to optimize charge carrier dynamics and overall efficiency.

2.2 $WO_3/BiVO_4$ photoanodes

Inorganic semiconductor photoelectrodes are the most promising materials for PEC water splitting, due to their suitable electrical properties, ease of fabrication and stability. Among the n-type semiconductors, tungsten trioxide (WO_3) received attention for its earth abundance, high electrical conductivity, and high chemical stability especially at low pH.[32] Its bandgap varies between 2.5 and 2.8 eV, so it is able to absorb 12% of the solar spectrum, it has a moderate length of hole diffusion of 150 nm and excellent electron transport properties, with a mobility of 12 $cm^2\ V^{-1}\ s^{-1}$.[32–34] The VB edge is positive enough for water oxidation, but the CB minimum is not negative than the HER redox potential, so it can only be used as a photoanode.

Bismuth vanadate ($BiVO_4$) is another promising material, with a smaller bandgap of 2.4 to 2.6 eV, good band edge positions, and stability. Despite the good band alignment to drive the water oxidation

reaction, that would give a maximum photocurrent of 7.5 mA cm^{-2} under AM 1.5G illumination, its poor electron transport properties and sluggish surface kinetics severely limit its efficiency.[35] Even though these materials are very promising, their PEC water splitting efficiency is too low to be competitive with other materials. Pairing WO_3 with $BiVO_4$ forming a n-n heterojunction (Figure 2.2) has proven remarkable performances compared to the individual materials due to the absorption properties of $BiVO_4$, efficient charge transport property of WO_3 and excellent matching of the energy bands for charge separation at the heterojunction.[36–42]

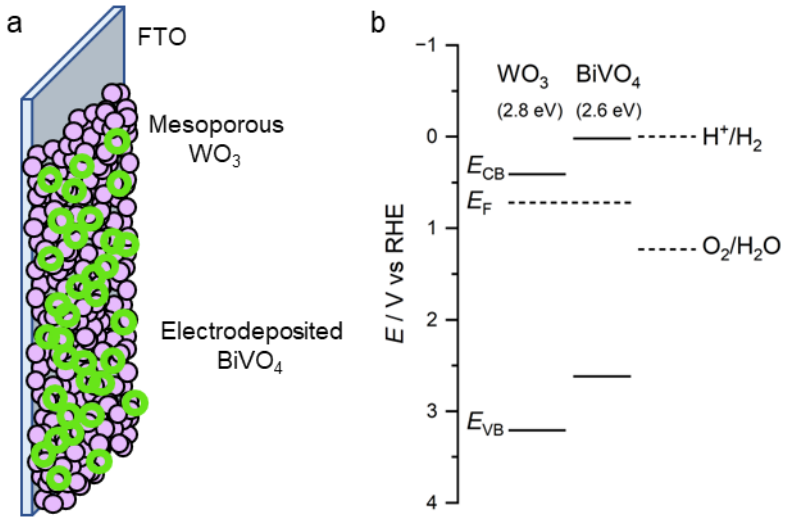

Figure 2.2: *a) schematic of a mesoporous WO_3/$BiVO_4$ photoanode and b) corresponding energy band diagram*

Another advantage of these materials comes from the possibility of synthetizing a nanostructured photoelectrode, to increase the surface area and provide more active sites for catalytic reactions, while also enabling facile charge transport throughout the material. The nanostructuring of the heterojunction can be achieved through various techniques, such as electrodeposition,[43] spin coating,[44] sol-gel,[45] or hydrothermal[46] methods, allowing precise control over its morphology and properties.

Despite the exceptional performance of WO_3/$BiVO_4$ heterojunctions, challenges persist, such as optimizing the surface engineering and mitigating charge carrier losses at the heterojunction. Along

with finding new methods for nanostructuring the morphology, surface treatments with deposition of overlayers, interfacial buffer layers, and doping $BiVO_4$ are strategies that can be employed to improve charge transfer kinetics and reduce interfacial resistance.[47] Furthermore, the complexity of the described system needs a deeper understanding of the dynamics of surface states and defects, which is crucial for further enhancing the performance and stability of the heterojunction under prolonged water splitting operations.

2.3 CIGS/CdS photocathodes

The chalcopyrite $Cu(In,Ga)Se_2$ (CIGS) is a good candidate for photocathodes, as it gathered considerable interest as an efficient absorbing layer in photovoltaic cells alternatively to silicon, and the position of its energy bands are well aligned to drive the HER. A CIGS-based photovoltaic cell (Figure 2.3) can be then used as a photocathode with slight changes in the architecture of the device.

The substrate needs to be insulating and stable throughout the deposition of all layers. Generally, soda-lime glass is used, as its coefficient of thermal expansion is close to CIGS and limits thermal stresses during the deposition of films, and it spontaneously supplies sodium to improve the performance of the cell.[48] A molybdenum film is then deposited on the glass by sputtering, with thicknesses around 500 nm.[49] Mo is a good material as back contact for charge collection, as an interfacial layer of $MoSe_2$ forms between Mo and CIGS which acts as an excellent ohmic contact.[50] The CIGS absorbing layer is a p-type semiconductor material, whose intrinsic doping comes by the formation of defects such as copper vacancies, and the indium/gallium ratio tunes the bandgap between 1.0 eV ($CuInSe_2$) and 1.7 eV ($CuGaSe_2$) and generally a Ga/(Ga + In) ratio of 0.3 is used, corresponding to a gap around 1.1-1.2 eV.[51] The high absorption coefficient enables its use in thin layers, generally with thicknesses of the order of 2 μm. Extrinsic doping of the material also can come from sodium or potassium migrating from the glass substrate. The buffer layer is cadmium sulfide (CdS) deposited by chemical bath deposition and is a n-type semiconductor forming the p-n junction with CIGS, allowing better charge separation and also passivating surface defects of the absorber.[52]

After that, the window layer limit electron losses and collect the carriers and consists of intrinsic zinc oxide (ZnO) and aluminum-doped zinc oxide (ZnO:Al or AZO), that are deposited by sputtering with thicknesses around 50 nm and 200-400 nm, respectively.[53] Finally, a protective layer is usually required when this heterostructure is used as photocathode in harsh environments and driving the HER. The best candidate is a thin (10-20 nm) layer of titanium dioxide (TiO_2),[54] as its large bandgap of 3.1 eV makes it almost transparent and is highly resistant to corrosion under harsh PEC operating conditions.

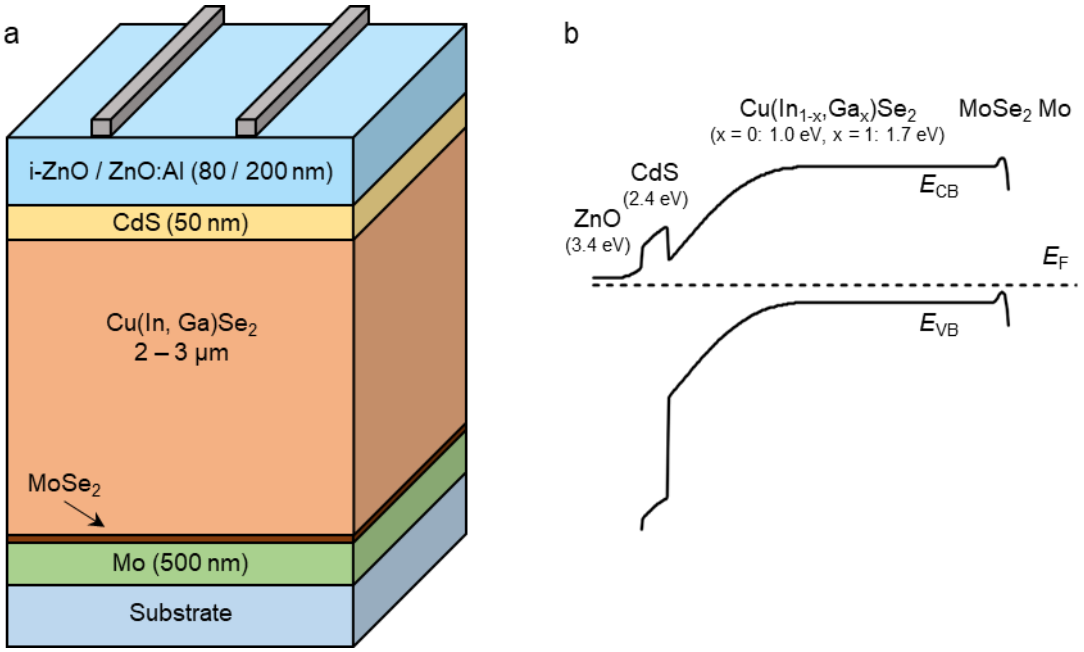

Figure 2.3: *a) schematic of a CIGS-based device structure and b) corresponding energy band diagram*

Even though the CIGS/CdS/ZnO/AZO/TiO_2 heterojunction offers promising performance, challenges remain in terms of optimizing catalyst integration to further enhance its functionality and maintaining stability under extended PEC operation conditions. The precise engineering of catalyst compositions, loadings, and interfacial interactions is essential for achieving high catalytic efficiency and minimizing degradation. Additionally, understanding the interplay between different materials and interfaces is crucial for improving charge carrier dynamics and reducing recombination losses.

2.4 Enhancing water splitting efficiency through surface modification

Although several materials have appropriate band-edge positions to drive OER and HER, the kinetics on the bare semiconductor surface generally limit the efficiency of the overall water splitting reaction. Overcoming this limitation requires a stronger driving force, i.e., an overpotential, to drive the desired reaction. A metallic catalyst deposited discontinuously onto the surface is effectively “transparent” and does not alter the light absorption properties of the semiconductor but can improve the kinetic of the reaction.

The identification of efficient electrocatalysts for the two half reactions (OER and HER) is crucial for developing efficient solar water splitting devices. This chapter focuses on the pivotal role of cobalt iron oxide, cobalt iron Prussian blue, and a nickel-molybdenum binary alloy in PEC water splitting, specifically driving the OER and HER reactions under illumination, when coupled with the appropriate photoelectrodes. While the term "photocatalyst" is often associated with materials that directly participate in light-induced reactions, the term "catalyst" is employed here to emphasize the function of these materials in facilitating the electrochemical processes at the photoelectrode/electrolyte interface.

2.4.1 Catalysts for oxygen evolution reaction (OER)

The water oxidation half-reaction requires four-electron transfer for oxygen production, which is more difficult than the two-electron HER due to the higher energy barrier and slower reaction kinetics.[16,55] A general mechanism for the OER on metal oxides in acidic solutions is given by the following Equations:

$$^{*}\mathrm{OH} + \mathrm{H_2O} \rightarrow [\mathrm{HO^{*}OH}] + \mathrm{H^{+}} + \mathrm{e^{-}} \quad (2.1)$$

$$[\mathrm{HO^{*}OH}] \rightarrow \mathrm{HO^{*}OH} \quad (2.2)$$

$$\mathrm{HO^{*}OH} \rightarrow \mathrm{O^{*}OH} + \mathrm{e^{-}} + \mathrm{H^{+}} \quad (2.3)$$

$$2O^{*}OH \rightarrow 2^{*}OH + O_2 \quad (2.4)$$

The primary discharge of either water (in acid) or hydroxide (in base) to oxidize a surface-active site (asterisk) is the first step (Equation 2.1). The result is an intermediate species, described by the square brackets. After further chemical conversion to a more stable surface species (Equation 2.2), the surface is oxidized further (Equation 2.3). An oxygen molecule is finally formed from the reaction of two highly oxidized surface sites (Equation 2.4). This mechanism makes no distinction between the oxygen intermediates that arise from the oxide lattice or from the water species. Indeed, the oxide lattice can participate in the oxidation, as seen in isotopically labeled RuO_2 and $NiCo_2O_4$ evolving isotopologues of O_2.[56–59]

In the last decades several strategies have been applied to photoanodes to improve the charge transfer in solution by surface decoration with OER catalysts.[60–64] In particular, these cocatalysts could accelerate photogenerated hole transfer, provide more active sites at the surface, overcome the reaction overpotential, suppress photo-corrosion, and reduce surface recombination, which are all effective ways to promote the water oxidation reaction.

Up to now, noble-metal (Ru and Ir) oxides, transition metal (Fe, Co, Ni *etc*.) oxides/hydroxides/hydroxyl oxides, C-based nonmetal materials, coordination polymers, and molecule catalysts have been widely used as OER catalysts to improve the surface kinetics of photoanodes during water oxidation. Transition metal-based materials became popular as they offered significant improvements in material costs and preparation methods, while more recently complexes based on Ru, Ir, Fe, Co, Ni, and Cu showed high activity and tunability, together with their ability to be integrated in more complex molecular assemblies attached to the surface of photoelectrode.[65,66]

OER catalysts offer a feasible way to efficiently transfer the photogenerated holes from the valence band to the surface of the photoanode and improve the charge separation efficiency. Co_3O_4 nanoparticles could extract photogenerated holes from a $BiVO_4$ photoanode, significantly enhancing

the photocurrent by affecting both bulk and surface kinetics, especially after incorporation of Fe^{3+} ions into the pristine metal oxide.[67–70] Cobalt phosphide (CoPi) also improved the PEC performance of a Fe_2O_3 photoanode, due to accelerated water oxidation kinetics and improved hole injection efficiency,[71–73] while a ultrathin NiFe-layered double hydroxide was able to shorten the transfer distance of holes at WO_3 nanorods.[74]

Another beneficial effect of OER catalysts is the suppression of surface recombination, as they can mitigate the activity of surface states that act as recombination centers for charge carriers. Examples of this effect are seen in works on IrO_x catalyst on Fe_2O_3 photoanodes,[75] or on $BiVO_4$ photoanodes decorated with CoPi, or cobalt iron Prussian blue.[23,76] Finally, OER catalysts can improve the water oxidation activity, for example by providing more active sites as shown in a work on $Co(OH)_x$ on Bi_2WO_6 photoanodes.[77] Of particular interest is a study on $CoFeO_x$ on $BiVO_4$ that enhanced the water oxidation reaction by reducing the overpotential.[78]

Another strategy to improve OER is introducing oxygen vacancies that enhance charge carrier transfer ability and H_2O absorption, or using nitrogen as a dopant, as it induces less lattice distortion than oxygen in metal oxides/hydroxides.[79,80] Prussian blue analogues with chemical formula of $M_3[M'(CN)_6]_2\ nH_2O$ (M and M' represent transition metal elements, e.g., Co^{2+}, Fe^{2+}, Fe^{3+}, Ni^{2+}, *etc*.) are excellent alternatives with non-oxide coordination, and several benchmark studies showed their stability and robustness.[81–83] However, they show lower current densities compared to metal oxides, probably due to the low number of active Co sites, as the cobalt atoms are connected to six N atoms of the cyanide group except the ones on the surface and in the vacancies created to provide charge balance. Cobalt hexacyanoferrate, the cobalt-iron analogue of Prussian blue (CoFe-PB), is a robust, effective, and inexpensive electrocatalyst that show low water oxidation onset potential and enhanced PEC performance. The origin of the increased efficiency is still debated, but recent studies suggest an enhancement of charge separation efficiency within the semiconductor that enables the

generation of long-lived photogenerated holes, rather than improved water oxidation kinetics,[23] underlying possible charge accumulation on the co-catalyst.

2.4.2 Catalysts for hydrogen evolution reaction (HER)

Three possible principal steps are involved in the HER process for the reduction of proton in acidic media or water molecules in alkaline media to hydrogen molecules on the surface of an electrode.[84] The first step is the Volmer reaction (Equations 2.5 and 2.6 for acidic and alkaline media, respectively), where a proton reacts with an electron and generates and adsorbed hydrogen atom (H^*) on the surface (M). The proton sources are the hydronium cation (H_3O^+) and the water molecule in acid and alkaline solutions, respectively. Then, there are two possibilities for the next step: either another proton diffuses to the H^* and reacts with a second electron to form H_2 through the Heyrovsky step (Equations 2.7 and 2.8 for acidic and alkaline media, respectively), or two H^* in the vicinity combine on the surface of the electrode to evolve H_2 through the Tafel step (Equation 2.9).[85] The overall HER is:

$$H_3O^+ + M + e^- \rightarrow M - H^* + H_2O \quad (2.5)$$

$$H_2O + M + e^- \rightarrow M - H^* + OH^- \quad (2.6)$$

$$H^+ + e^- + M - H^* \rightarrow H_2 + M \quad (2.7)$$

$$H_2O + e^- + M - H^* \rightarrow H_2 + OH^- + M \quad (2.8)$$

$$2M - H^* \rightarrow H_2 + 2M \quad (2.9)$$

The interaction between the catalyst and these reactive intermediates should not be too weak, as too few intermediates (H^*) would bind to the surface of the catalyst, slowing down the reaction, nor too strong, as the reaction products (H_2) would fail to dissociate and stop the reaction by blocking the active sites.

Noble metals like Pt, Pd, Ru, Ir, and Rh demonstrate excellent catalytic properties towards the HER, with a moderate M–H bond strength that results in optimized adsorption and desorption of hydrogen, especially for platinum.[86] Despite their excellent catalytic properties, high cost and limited availability are the main drawback for widespread applications of these state-of-the-art HER catalysts. Electrocatalysts based on earth-abundant elements are promising alternatives, but they are susceptible to corrosion under strong acid or alkaline conditions. Metallic nickel has shown the best catalytic activity for HER among various nonprecious metals and through voltammetry techniques their performances follow the order: Ni > Mo > Co > W > Fe > Cu.[87] Recently, nickel-based binary alloys have been investigated due to high performance and low cost.[88] NiMo has the best catalytic activity in alkaline conditions, followed by NiZn, NiCo, NiW, NiFe, NiCr.[89] In a study from Baek *et al*., NiMo was coupled to a CIGS photocathode and showed a remarkable onset potential of 0.5 V and short circuit photocurrent density as high as 15 – 25 mA cm^{-2} under various pH conditions, which is very encouraging as it is comparable to the performance of Pt- coated CIGS.[54]

Stability and long-term performance are primary concerns for earth-abundant-based HER catalysts and degradation can come from corrosion, catalyst poisoning by solution impurities, and changes in the electrode composition and morphology during HER. These effects can occur over long- or short-time scales, as with hydrogen absorption in Ni, which begins immediately and progresses as the electrode continues to be used.[90,91] These three degradation mechanisms depend on electrolyte composition, pH, and specific operating conditions (temperature, applied potential, current density). Ni-based binary alloys are easily corroded under strong alkaline conditions, so a common solution is to add a protective layer of graphitic carbon.[92]

2.5 Hybrid photoelectrodes

Hybrid photoelectrodes comprised of a narrow bandgap semiconductor with an integrated molecular catalyst are actively being investigated for the generation of fuels from chemical feedstocks and sunlight.[93,94,103,95–102] The interfacial electron transfer processes that govern the efficiency of

such hybrids are understood through a model that requires isoenergetic transfer between the catalyst and photogenerated carriers at the fixed energetic position of the conduction or valence band edge.[104–107] This model was first described in the 60s by the combined theoretical work of Marcus and Gerischer,[104,105] and continues to be disseminated in modern research publications and text books of electron transfer theories.[106,107] This energetic requirement is suitable for optimization of single electron transfers of importance to regenerative solar cells,[30] yet remains challenging for important multi-electron catalysis such as water oxidation and carbon dioxide reduction.

To appreciate challenges associated with multi-electron transfer photocatalysis at a semiconductor-electrolyte interface, consider the hypothetical electrostatic potential alignment shown in Scheme 2.1, where the energetic positions of the conduction band edge ($V_{CB} = E_{CB}/q$) and reduction potentials (E^o) of a molecular catalyst are rigidly fixed relative to one another. A generic catalytic cycle comprised of a resting state, Cat, that undergoes two sequential one-electron transfers for the net two-electron catalytic reduction of CO_2 to CO is further considered.[93] In this hypothetical representation, the first reduction potential, $E°(Cat^{n/n-1})$, is within the forbidden bandgap of the semiconductor and energetically closer to the semiconductor Fermi level, $V_F = E_F/q$, than is $E°(Cat^{n-1/n-2})$. Upon equilibration, interfacial charge transfer occurs until V_F aligns with $E°(Cat^{n/n-1})$. Due to the low density of carriers in the semiconductor, essentially all of the potential drop occurs in the semiconductor, as depicted by the band bending in Scheme 2.1. The energetic position of V_{CB} relative to $E°(Cat^{n/n-1})$ at the semiconductor-electrolyte is unchanged. Activationless isoenergetic transfer is expected when V_{CB} lies energetically above $E°$ by a magnitude equal to the reorganization energy.[104,105]

Transfer of the second electron is energetically unfavored for an electron at V_{CB} as shown in Scheme 2.1. Transfer from a non-thermalized electron is possible,[108] but prior research has shown that such "hot" interfacial electron transfer is highly inefficient due to strong electron-phonon interactions.[107,109–112] Instead, efficient electron transfer would require a semiconductor with a more negative V_{CB} (closer to the vacuum level). Even if an alternative semiconductor material was

identified for the second reduction, this material would necessarily have band edge positions less favorable for the first reduction. Hence, optimization of single electron transfers at semiconductor-electrolyte interfaces may be achieved through energetic alignment,[30,31] but the requirements of fixed band edge positions present significant challenges for optimization of multi-electron transfer catalysis.

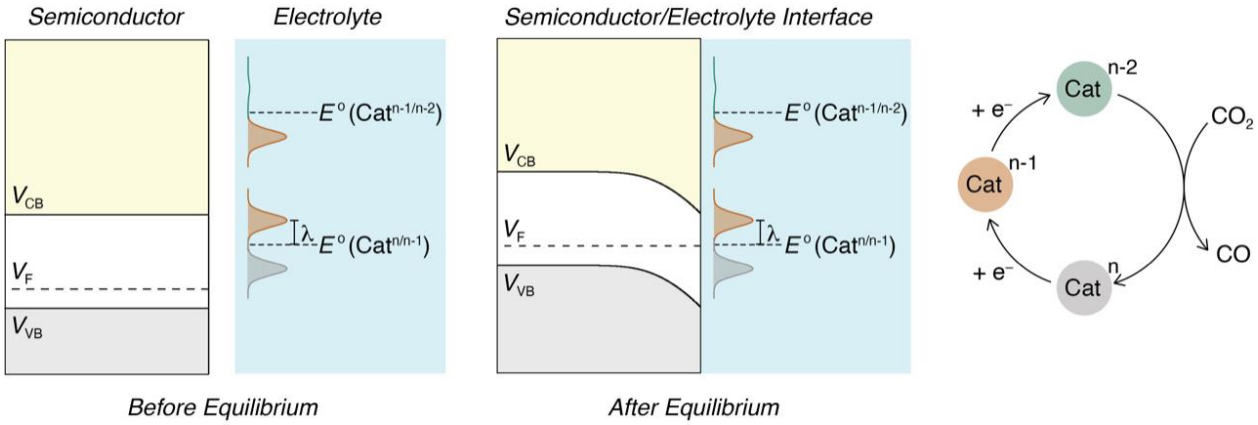

Scheme 2.1: *Hypothetical interfacial energetics at a semiconductor electrolyte interface for a generic catalytic two-electron reduction of CO_2 to CO. Before equilibrium, $E^{o}(Cat^{n/n-1})$ lies within the forbidden bandgap while $E^{o}(Cat^{n-1/n-2})$ is within the continuum of unfilled conduction band states. At equilibrium, the Fermi energy (V_F) is equal to $E^{o}(Cat^{n/n-1})$ and a depletion layer shown by band bending serves to sweep conduction band electrons toward the catalyst and valence band holes toward the semiconductor bulk. With a model where the band edge positions are fixed, the first reduction in the catalytic cycle is ideal and would generate the largest photovoltage. In contrast, the second reduction – with $E^{o}(Cat^{n-1/n-2})$ above the conduction band edge, V_{CB} – is expected to be highly inefficient.*

The energetic alignment shown for the first reduction in Scheme 2.1 is most optimal for interfacial electron transfer and for generation of a large photovoltage.[105,113,114] In contrast, electron transfer is not expected to be efficient for the second reduction because the potential falls outside the forbidden bandgap.[113] This is important as the photovoltage is the maximum Gibbs free energy available from bandgap excitation. In chapter 4, the assumption of fixed band edge positions is shown to be incorrect for multi-electron transfer at H-terminated p-Si electrolyte interfaces. The largest photovoltage will be indeed realized when the E^{o} is within the continuum of conduction band states, like that shown for $E^{o}(Cat^{n-1/n-2})$.

3 Characterization techniques

A wide variety of spectroscopic and microscopic techniques providing structural and mechanistic information can be employed depending on the system under investigation and the required spatial and temporal resolution. Spectroscopic investigations of heterogeneous systems with time-resolved techniques focus on the mechanistic aspects of the light-driven processes, such as light absorption, charge separation, charge transfer, and different recombination paths both in the bulk and on the surface. In the following chapter transient absorption spectroscopy (TAS) and intensity modulated photocurrent spectroscopy (IMPS) are described. A particular focus is on *operando* setups as they report on the charge carrier kinetics inside photoelectrodes under controlled operating conditions, while the OER or the HER are taking place (in solution, under illumination, and with applied bias).

3.1 Principles and applications of transient absorption spectroscopy (TAS)

This chapter explores the fundamental principles and applications of transient absorption spectroscopy (TAS), a powerful technique used to study the dynamics of short-lived electronic and vibrational excited states in various systems. TAS is an invaluable tool in the study of transient species and photoinduced processes in various scientific disciplines, including physics, chemistry, materials science, and biochemistry, as it provides insights into the dynamics of excited states over a wide range of time scales, from seconds down to attoseconds.

In TAS, a sample is irradiated with a short-duration laser pulse (pump), and the absorption of the sample is monitored after a certain time delay with a second white light source, usually a Xe lamp (probe). In fact, the energy absorbed from the pump causes transitions between different electronic states, leading to the generation of photo-carriers or excited states within the sample.

The transmittance of a sample is:

$$T = \frac{I_{trans}}{I_{inc}} \tag{3.1}$$

where I_{trans} is the transmitted intensity and I_{inc} is the incident intensity on the sample. The absorbance is defined as:

$$A = \log_{10} \frac{I_{inc}}{I_{trans}} = -\log_{10} T \quad (3.2)$$

and TAS measures how the absorbance of the sample changes between its ground and excited state (after the pump pulse), so we can express the change in absorbance as:

$$\Delta A \equiv A_{pump} - A_{no\ pump} = \log_{10} \frac{I_{no\ pump}}{I_{pump}} \quad (3.3)$$

Here, $I_{no\ pump}$ and I_{pump} are the transmitted intensity without and with pump excitation, and it is important to notice that we do not need to measure the intensity of the incident pulse.

3.1.1 Transient Absorption Spectroscopy Setup

The transient absorption spectroscopy setup comprises several key components that enable the accurate and precise measurement of transient species dynamics. The primary elements of this setup include a light source, an optical system, and a detector. The light source provides the pump and probe pulses, which are typically generated using ultrafast laser systems. These lasers produce short pulses of light with durations in the femtosecond to picosecond range, matching the timescales of electronic and vibrational transitions. The optical system directs and focuses the pump and probe pulses onto the sample, ensuring spatial and temporal overlap. The sample is usually in the form of a thin film or a solution, placed in a cuvette or on a solid support. Following sample excitation, the transmitted light is collected and directed towards a sensitive detector, such as a photodiode or a streak camera. The detector records the changes in the intensity of the probe pulse due to the sample's transient absorption.

Apart from the ultrafast pump-probe setups, there are alternative transient absorption spectroscopy configurations that allow the investigation of processes occurring on longer timescales, also called

laser flash-photolysis (LFP). By employing this alternative setup (Figure 3.1), researchers can explore dynamics with lifetimes from nanoseconds to milliseconds, providing insights into slower processes such as chemical reactions, protein conformational changes, and relaxation phenomena in complex systems. Moreover, these longer timescale transient absorption spectroscopy setups complement ultrafast techniques, offering a comprehensive understanding of the dynamics spanning a wide range of timescales in various research domains.

The schematic of the experimental setup for pump-probe LFP measurements is shown in Figure 3.1. Time-resolved infrared (TRIR) measurements on p-Si photocathodes were performed with a benchtop nanosecond transient mid-IR spectrometer (inspire, Magnitude Instruments) equipped with a pulsed 532 nm excitation laser and a germanium bandpass filter (1-5 μm). Fixed applied potentials were controlled by a CH Instruments electrochemical workstation model CHI 760E using a Pt mesh as the counter electrode and a leakless Ag/AgCl reference electrode. TAS measurements on WO_3/$BiVO_4$ photoanodes had a similar layout and employed a pulsed 355 nm excitation laser as pump. The white light of the probe source, a 450 W Xe lamp, was passed through a color filter before passing through the sample to probe the changes in absorption. The lamp was equipped with a multigrating detection monochromator outfitted with a photomultiplier tube (PMT). The detector was software selectable with the PMT for monitoring absorption kinetics at a single wavelength, covering the entire visible region. For these measurements, the spectral bandwidth was typically 10 nm with color notch filters placed after the sample but before the detection monochromator to eliminate laser scatter. Single-wavelength kinetic data were collected by averaging 100 sequences where one sequence refers to collection of probe-only ($I_{\text{no pump}}$) data followed by pump-probe (I_{pump}) data. The time resolution in these setups is achieved through electronic delay circuits and a shutter system. The electronic delay circuits enable precise control of the time delay between the pump and probe beams, while the shutter system controls the exposure of the sample to the probe light, ensuring accurate temporal resolution.

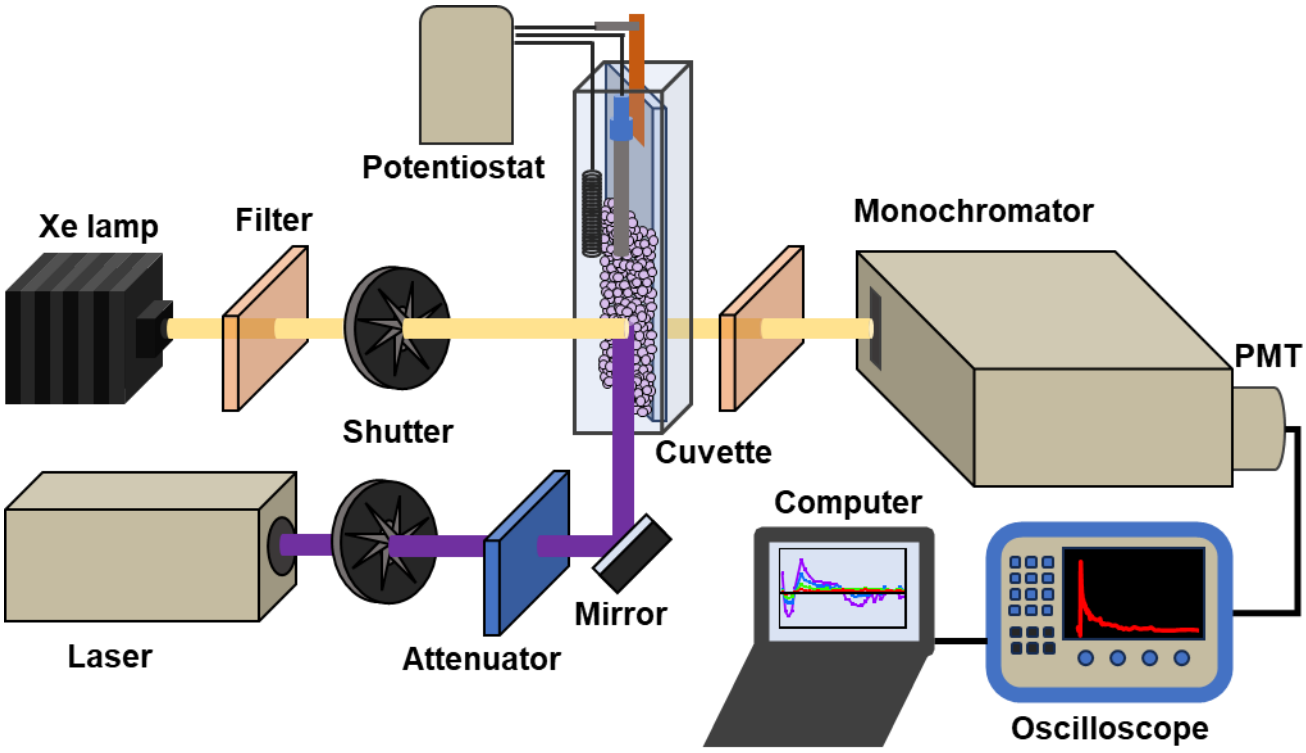

Figure 3.1: *schematic of a typical transient absorption spectroscopy setup*

After collecting the single-wavelength kinetic data a complete TA spectrum can be built by extracting $\Delta A(t^*)$ values at a fixed time delay t^* for all the probed wavelengths.

To understand the contributions to TAS spectra it is necessary to start from the energy level scheme of a semiconductor. After pump excitation, the electrons that occupy states close to the Fermi level are promoted to free states above the Fermi level. Usually, the energy of the pump pulse is greater than the energy gap so that electrons from the valence band can be promoted up to the conduction band. If this is the case, the concentration of absorbers (electrons) in the ground state (valence band) decreases and the transmittance of the probe light through the sample becomes higher. Therefore, $I_{\text{pump}} > I_{\text{no pump}}$, and $\Delta A < 0$ from Equation. The spectral feature coming from this negative contribution is called ground state bleaching and its signal is seen until all the excited electrons return to the valence band.

Another typical contribution commonly seen in semiconductors is called induced absorption. It comes from electrons excited by the pump pulse in transient energy states and can be excited again to higher energy states by the probe. For example, electrons excited from the valence to the conduction band minimum can be excited again in higher energy states above the conduction band. In this case, $I_{\text{pump}} < I_{\text{no pump}}$, and $\Delta A > 0$, as an additional absorption process is present. This contribution is usually related to free electrons in the conduction band or trapped electrons or holes in energy levels inside the energy gap, such as surface states or traps.

3.1.2 Transient decays in thin film photoelectrodes

Different equations can be used to fit the transient decay of the kinetic traces to obtain an analytical description of the relaxation to the ground state. The simplest equation is a first-order recombination kinetics that mathematically is described by a mono-exponential decay with equation:

$$\Delta A = A \exp\left(-\frac{t}{\tau}\right) \tag{3.4}$$

where τ is the time constant describing the decay, and A indicates the amplitude of the decay process and can be associated to the number of excited carriers that return to the ground state following this decay path.

When probing the transient decay over different orders of magnitude, more decay processes can be present at different times and in this case the TA signal can be fitted with a multi-exponential function, which is the sum of mono-exponential functions with different amplitudes and time constants. However, pure exponential relaxation is rarely found in nature, and it usually occurs over a wide time range, therefore an infinite sum of exponential with a distribution of characteristic times would be more helpful in more accurately describing the system. The Kohlrausch-Williams-Watts (KWW) function,[115,116] also commonly referred to as *stretched exponential* function, is a common alternative and a convenient tool when dealing with disordered systems:

$$\Delta A = A \exp\left(-\left(\frac{t}{\tau}\right)^{\beta}\right) \quad (3.5)$$

Where $0 < \beta < 1$ is the stretching exponent and for $\beta = 1$ the usual exponential function is recovered.

Another common function used to describe recombination in nanostructured systems is the power law decay:

$$\Delta A = Bt^{-\alpha} \quad (3.6)$$

Physically, the power law represents diffusion-limited recombination processes involving localized carriers,[117,118] which undergo relaxation within a broadened density of states.[119,120] The coefficient α describes how quickly the decay is and smaller values of α are associated with longer-lived signals (Figure 3.2)

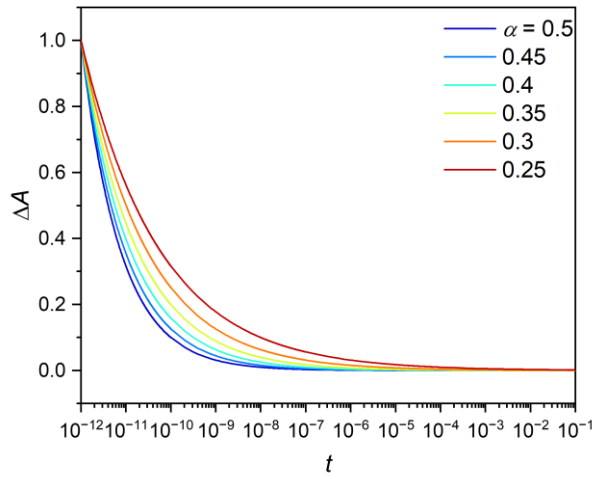

Figure 3.2: *Simulation of data following a power law $\Delta A = Bt^{-\alpha}$ normalized at t = 1 ps and with different values of the exponent α.*

The power law decay, contrarily to a single exponential function, occurs at all time scales and could be again described by an infinite sum of exponential functions with a distribution of characteristic times:

$$t^{-\alpha} = \frac{1}{\Gamma(\alpha)} \int_0^{\infty} s^{\alpha-1} e^{-st} ds \quad (3.7)$$

Figure 3.3 shows the different kinetics described by a mono-exponential, a KWW function and a power law. It is interesting to notice that in a log-log plot the power law shows a linear behavior and this feature could be helpful while choosing the appropriate fitting function of TA data.

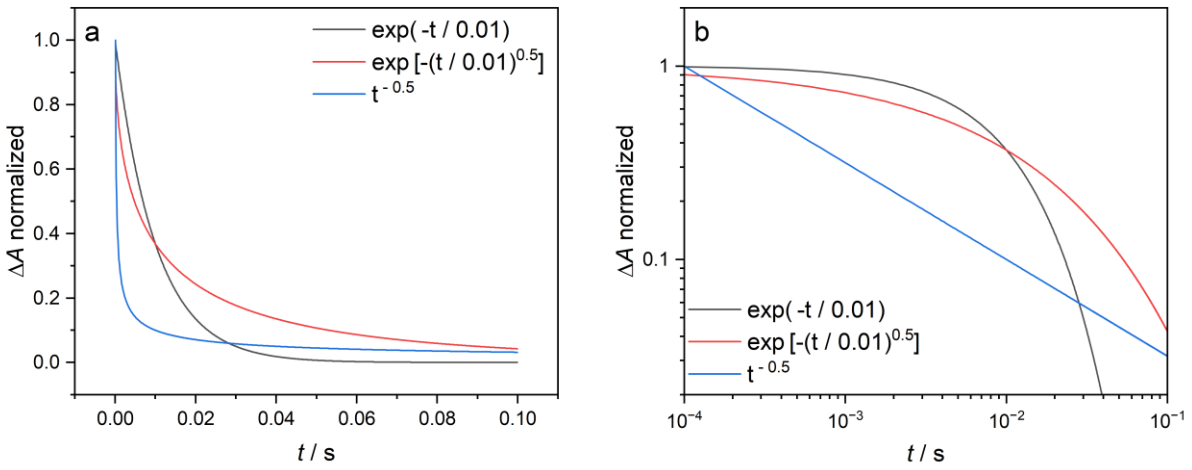

Figure 3.3: *examples of different kinetics that can be observed during a TAS experiment: single exponential, stretched exponential, and power law decay*

3.2 Intensity modulated photocurrent spectroscopy (IMPS)

The study of optoelectronic properties of materials is crucial for the development of efficient photoelectrodes, but also for other technological applications, such as solar cells, photodetectors, light-emitting diodes, and optoelectronic devices. Intensity Modulated Photocurrent Spectroscopy (IMPS) is a powerful and non-destructive technique used to investigate the charge carrier dynamics, transport, and recombination processes in semiconducting and optoelectronic materials. IMPS provides valuable insights into the performance and efficiency of these materials and aids in optimizing their design and functionality.

Before the advent of IMPS, traditional photocurrent and photovoltage measurements offered valuable information on the photogenerated charge carriers, but they were limited in their ability to provide dynamic and time-resolved data. IMPS involves the application of a small perturbation of light

intensity $\varphi_{inc}(\omega)$ and measuring the corresponding modulated current response $I_{ph}(\omega)$ over a wide range of frequencies ω. The response function $Y(\omega)$ as the form of an admittance and is calculated as:

$$Y(\omega) = \frac{I_{ph}(\omega)}{\phi_{inc}(\omega)} \tag{3.8}$$

A direct current (DC) light bias is used to keep the system close to real working conditions and the amplitude of the sinusoidal light perturbation is kept small (usually below 10% of the intensity of the DC light bias), in order to ensure a linear response of the photocurrent to the light stimulus.

3.2.1 IMPS setup

The typical IMPS setup is shown in Figure 3.4 and consists of a light-emitting diode (LED) as a light source that is modulated by an LED driver (Thorlabs DC2100) and a beam splitter that transmits a fraction of the light onto the sample (for the measurements shown in this thesis, it was placed inside a PEC cell with a PGSTAT204 electrochemical workstation, using a three-electrode configuration with a Pt counter electrode and Ag/AgCl as the reference) and direct a portion of the light onto a calibrated silicon photodiode (Hamamatsu). This allows simultaneous measurements of the light intensity and photocurrent, which is critical for normalizing the photocurrent data and obtain the transfer function of Equation 3.8.

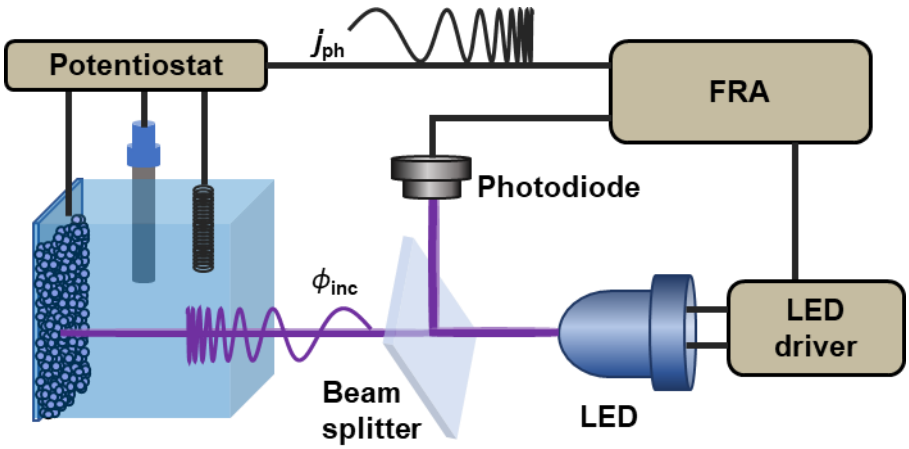

Figure 3.4: *schematic of a typical intensity modulated photocurrent spectroscopy setup*

The intensity of the incident light is modulated at a specific frequency, typically in the range of a few Hz to several MHz. This modulation can be achieved using a variety of techniques, such as choppers, mechanical shutters, or electro-optic modulators. In this setup we used a frequency response analyzer (FRA) module of the PGSTAT204 electrochemical workstation, that is able to generate alternating current (AC) signals with different frequencies. This is summed to a DC potential signal using an operational amplifier and is sent to the LED driver where it is converted to the current given to the monochromatic LED. For small variations, the light intensity emitted by the LED is directly proportional to the current passing through and also to the AC potential generated by the FRA. By modulating the light, the photocurrent generated in the material also oscillates at the same frequency.

The light intensity measured by the silicon photodiode is converted to a current based on its responsivity at the specific wavelength used in the experiment. This current is further amplified to obtain a voltage signal using a current amplifier. Similarly, the photocurrent generated at the photoelectrode is measured at the counter electrode and converted to a potential signal based on the current range used during the measurements.

Both the light intensity and photocurrent signals are fed back as voltage inputs to the FRA for data analysis. The FRA measures the amplitudes of the two sinusoidal AC signals, determines their phase shift, and calculates the quantity $Y(\omega)$ with Equation 3.8, for each frequency used during the experiment. $Y(\omega)$ is a complex number, and its real and imaginary components are used to construct a Nyquist plot, which is a common representation of IMPS spectra in literature. The Nyquist plot provides valuable insights into the charge carrier dynamics and recombination processes at the photoelectrode surface. By analyzing the Nyquist plot, crucial information about the charge carrier lifetime, mobility, and recombination mechanisms can be extracted.

3.2.2 The rate constant model in IMPS

The theoretical basis of IMPS was elaborated by Peter and co-workers between the 1980s and 1990s[121–125] by solving kinetic equations that were representing systems with single and multistep processes, but all their models needed some *a priori* information, such as the expression of the reaction mechanisms, that are not always known. As a result, the model of the system under investigation was always adapted to the most trivial case, that considers only two main kinetic processes, the hole transfer from the semiconductor surface to the electrolyte, and the recombination of these holes at the surface with bulk electrons.[76,126,127] This model is called rate constant model (RCM), as it associates two rate constants k^{trans} and k^{rec} to the two processes just described. The oversimplification of the carrier kinetics in this model hinders any insights into multistep or parallel processes happening at the surface, which would be expected in more complex nanostructured heterojunctions.

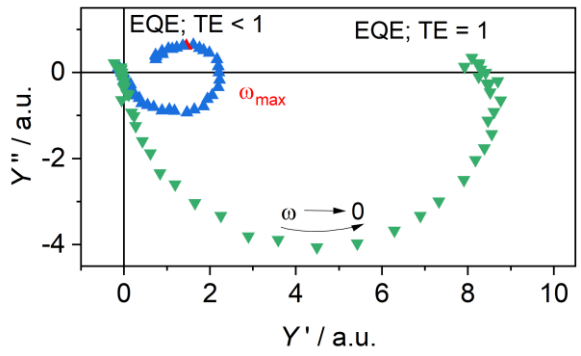

Figure 3.5: *Examples of IMPS spectra at different applied potentials. The blue plot shows the behavior at low applied potentials, where a loss of EQE is present due to a low TE. The green plot shows the behavior at high potentials where surface recombination becomes negligible, and the TE is assumed to be 1.*

By graphical inspection, IMPS spectra of a semiconductor/electrolyte interface show two semicircles in the Nyquist plot (Figure 3.5):[128] one in the fourth quadrant ah high frequencies and the other in the first quadrant at lower frequencies. The low frequency end of the spectrum contains fundamental information about the surface kinetics of the system: at the lowest frequency the photocurrent will be

in phase with the light modulation and the spectrum intercepts the real axis (Y' = 0). At higher frequencies, the photocurrent will start to be delayed with respect to the light modulation. This phase shift is given by the competition between charge transfer and recombination, and it results in the formation of a "recombination" semicircle in the Nyquist plot. The frequency ω_{max} that corresponds to the point where the imaginary component is maximum reports on the rate of transfer and recombination:

$$\omega_{\max} = k^{\text{trans}} + k^{\text{rec}} \tag{3.9}$$

Then, the spectrum crosses again the real axis and here the real component of Y is proportional to the number of charges available to be transferred in solution, and at even higher frequencies the spectrum is convoluted with the characteristic time constant of the PEC cell $\tau_{cell} = (2\pi\omega_{min})^{-1}$, where ω_{min} is the frequency where the imaginary component is maximum in module but with a negative sign. This characteristic time is related to the impedance of the cell through:

$$\tau_{\text{cell}} = R\frac{C_{\text{sc}}C_{\text{H}}}{C_{\text{sc}}+C_{\text{H}}} \tag{3.10}$$

where R is the total series resistance arising from the electrolyte, the semiconductor bulk and the ohmic contact, C_{sc} is the SCL capacitance, and C_H is the Helmholtz capacitance.[121] Then the spectrum loops back to the origin, as at very high frequency there is no measured photocurrent, forming the "generation" semicircle in the fourth quadrant of the Nyquist plot.

The size of the recombination semicircle describes the transfer efficiency (TE) of the system, that can be calculated by the ratio between the two real component of the intercepts with the real axis at low frequencies just described. The TE is also related to the transfer and recombination rate,[129] according to:

$$\text{TE} = \frac{k^{\text{trans}}}{k^{\text{trans}}+k^{\text{rec}}} \tag{3.11}$$

Consequently, from Equations 3.19 and 3.11 k^{trans} and k^{rec} can be estimated. This analysis relies on the presence of a maximum and intercept values of the IMPS spectrum, however, the extraction of these values is not always straightforward and also requires that the two features of the spectrum (the generation and recombination semicircles) have very well separated characteristic times (or frequencies), so $\tau_{cell} << 1/\omega_{max}$, and this is not always true for real systems.[121] A more effective method to deconvolve generation and recombination processes with similar characteristic times is described in the next section of this thesis.[21]

Following the work of Gutiérrez *et al*.,[130] the IMPS transfer function can be also normalized in the following way. The photocurrent can be divided by the electron charge *e*, and the intensity can be divided by hc/λ, where λ is the wavelength of the incident photon, so that they are expressed in electrons cm^{-2} s^{-1} and photons cm^{-2} s^{-1}, respectively:

$$Y(\omega) = \frac{j_{ph}(\omega)}{\phi_{inc}(\omega)} \cdot \frac{hc}{\lambda e} \tag{3.12}$$

With this normalization the quantity $Y(\omega)$ describes the number of charge carriers divided by the number of incident photons and contains information on the efficiency of the photoelectrode.

Now, the value of the intercept of *Y* with the real axis is LHE × CSE, where LHE is the light harvesting efficiency, defined as the fraction of light intensity absorbed by the material at each wavelength, and CSE is the charge separation efficiency and represents the percentage of photogenerated holes that are available for oxidation reactions and provides information on the transport properties of the material. The intercept with the real axis at the lowest frequency corresponds to the external quantum efficiency (EQE) of the system. Therefore, the overall efficiency of the photoelectrode is:

$$\mathrm{EQE} = \mathrm{LHE} \times \mathrm{CSE} \times \mathrm{TE} \tag{3.13}$$

The EQE is the ratio between the number of holes transferred to the electrolyte and the number of absorbed photons. Thus, from a single IMPS measurement, it is possible to extract information on bulk transport processes and surface recombination processes of the photoelectrode.

Going back to Figure 3.5, if the positive semicircle is present (blue triangles), surface recombination is much faster than hole scavenging; consequently, the photogenerated charges recombine and TE < 1. If the positive semicircle is absent (green triangles), it means that the charge transfer is much faster than surface recombination and the EQE is governed essentially by the rate of hole transfer to the solution. In this latter case, other features might be observed: when the cell time constant is close to the charge separation time constant, two superimposed semicircles possibly merging in one distorted semicircle appear in the complex plane; while if the charge separation is much faster, the spectrum results in one symmetrical semicircle.

3.3 Lasso-Distribution of Relaxation Times (L-DRT) algorithm for IMPS data fitting

The Distribution of Relaxation Times is a technique used in electrochemical impedance spectroscopy (EIS) or in IMPS to analyze and interpret complex impedance or admittance data obtained from electrochemical systems. It is especially valuable for studying systems such as electrode/electrolyte interfaces with various charge transfer and diffusion mechanisms, as it aims to deconvolute the frequency-resolved response of the system to reveal the characteristic timescales of each process.

Contrarily to the RCM described earlier, a DRT algorithm allows to have an assumptions-free understanding of the frequency domain response function, and it allows for a quantitative analysis of simple and complex systems. The main goal of DRT is to identify the distribution of typical characteristic times in the system, by fitting the admittance in Equation 3.8 with the integral equation:

$$\int_0^\infty \frac{g(t)}{1+i\omega t} dt = Y(\omega) \in \mathbb{C} \qquad (3.14)$$

where ω is the frequency at which the admittance $Y(\omega)$ is measured, $g(t)$ represents the unknown real-valued distribution over the times t that we want to find, and $i = \sqrt{-1}$ is the imaginary unit. From experimental measures we only know $Y(\omega)$ for a finite number of frequencies $\{\omega_1, \ldots, \omega_M\}$, such that the set $\left\{\tau_m = \frac{1}{2\pi\omega_m}\right\}_{m=1}^{M}$ is logarithmically evenly distributed in the range $[10^{-1}, 10^{4}]$. This problem is ill-posed in the sense of Hadamard,[131] as the solution is certainly not unique (i.e., different distributions $g(t)$ give the same integral); therefore, a choice must be done on which kind of solution is preferred. Ideally, the resulting distribution should fit nicely the data $\{Y(\omega_1), \ldots, Y(\omega_M)\}$ when plotted on the complex plane, without overfitting it.

From the physics of the system under investigation, it is reasonable to assume that the set of τ_m such that $g(\tau_m) \neq 0$ is discrete, i.e., there are very few characteristic times that fully describe the admittance of the system. The goal is to find this set of characteristic times with great precision. Once a characteristic time τ_m is found, the corresponding value $g(\tau_m)$ can be considered as its weight in describing the system. A positive (negative) weight means that the characteristic time increases (decreases) the photocurrent. Moreover, the weight can either be fully assigned to a single characteristic time using a Dirac distribution $g(\tau_m)\delta(\tau - \tau_m)$, or be distributed around τ_m using a Gaussian function with a physically reasonable standard deviation σ.

This problem will be tackled numerically with a discretization of the integral. The time range is subdivided in $N > M$ evenly logarithmically spaced intervals $[\tau_m, \tau_{m+1}]$, so that Equation 3.14 becomes:

$$Y(\omega_m) = \sum_{n=1}^{N} \frac{g(\tau_n)}{1 + i\omega_m\tau_n}, \qquad (3.15)$$

for $n = 1, \ldots, N$. Typically, $N = S \times M$ and a reasonable value is $S = 10$, meaning that the number of considered characteristic times is 10 times larger than the number the experimental frequencies. This results in a $(N \times M)$ complex linear system

$$Ag = b, \tag{3.16}$$

where $A \in \mathbb{C}^{M\times N}$ is the matrix $(A_{m,n}) = 1/(1 + i\omega_m\tau_n)$ and $b \in \mathbb{C}^M$ is the vector with the data ($Y(\omega_1)$, …, $Y(\omega_M)$). An additional requirement for the vector $g \in \mathbb{R}^N$ is to be sparse, i.e., with "many" zero-entries.

The linear system is first split it in real and imaginary part:

$$\begin{cases} A'g = b' \\ A''g = b'' \end{cases} \tag{3.17}$$

where the two matrices A' and A'' have entries

$$\left(A'_{m,n}\right) = \frac{1}{1+\omega_m^2\tau_n^2} \qquad \left(A''_{m,n}\right) = -\frac{\omega_m\tau_n}{1+\omega_m^2\tau_n^2} \tag{3.18}$$

and b' and b'' are, respectively, the real and imaginary parts of b.

Then it is necessary to solve the following minimization problem

$$g = \arg\min_{x\in\mathbb{R}^N} \left(\left|\left|A'x - b'\right|\right|_2^2 + \left|\left|A''x - b''\right|\right|_2^2 + \lambda \left|\left|x\right|\right|_1 \right), \tag{3.19}$$

where $\| - \|_p$ denotes, as usual, the p-norm. In addition to the least square problem, the regularization term $\lambda\left|\left|x\right|\right|_1$ helps avoiding overfitting. Different choices can be made: here, we decide to introduce a Lasso regularization, as it is often used to achieve sparse solutions, penalizing solutions with a high number of non-zero entries.[132]

The parameter $\lambda \in \mathbb{R}_{\geq 0}$ weights how much regularization is introduced in the minimization problem. Some validation tests have been developed[132] for identifying the best regularization parameter λ but these value may depend also on the quality of the measured data.[133] In general, if λ is too small,

the regularization term becomes negligible and the solution is overfitted; if it is too big ($\lambda > 1$), the regularization becomes prevalent, resulting in a solution which is identically zero.

In the following, we show hot the application of this algorithm can improve the analysis of two different systems: (i) a simulated discrete system, made of a specific number of characteristic times, and (ii)a generalized physical RCM described by kinetic equations. The algorithm will be also applied to IMPS measurements made on WO_3/$BiVO_4$ photoanodes and CIGS-based photocathodes that are shown later in in chapters 6 and 7.

3.3.1 Simulated discrete system

The first benchmark to validate the algorithm is a simulated dummy system made of *N* different time constants, that is equivalent to an electrical circuit constituted by a series of *N* Voigt elements (i.e., parallel RC's). Every Voigt element is characterized by a characteristic time $\tau_n = R_n C_n$ and a weight, given by the value R_n of the resistance. The impedance of such a circuit is

$$Z(\omega) = \sum_{n=1}^{N} \frac{R_n}{1+i\omega\tau_n}. \quad (3.20)$$

Equation 3.20 is equivalent to Equation 3.15, upon substituting R_n with $g(\tau_n)$. The main difference is that $g(\tau_n)$ can be also negative in the IMPS case. Therefore, IMPS data were generated using Equation 3.15 with $N = 4$. The values used for the calculation are reported in Table 3.1.

The IMPS spectrum generated using Equation 3.15 and shown in Figure 3.6 displays two semicircles, one in the negative and one in the positive imaginary admittance quadrant, suggesting a system defined by two characteristic times. However, the characteristic times used to simulate this spectrum are four, two negatives and two positives, clearly pointing out how a simple graphical evaluation of such IMPS spectra is not reliable for the identification of the number of elements characterizing the circuit.

Table 3.1: *Values of τ_n and $g(\tau_n)$ used for simulating the IMPS spectrum. In the last column is reported the height of the peak obtained using the L-DRT algorithm.*

n	$\tau_n\ (ms)$	$g(\tau_n)$	Peak height (Lasso)
1	3	0.75	0.73
2	10	1	1.01
3	80	-0.2	-0.19
4	500	-0.5	-0.49

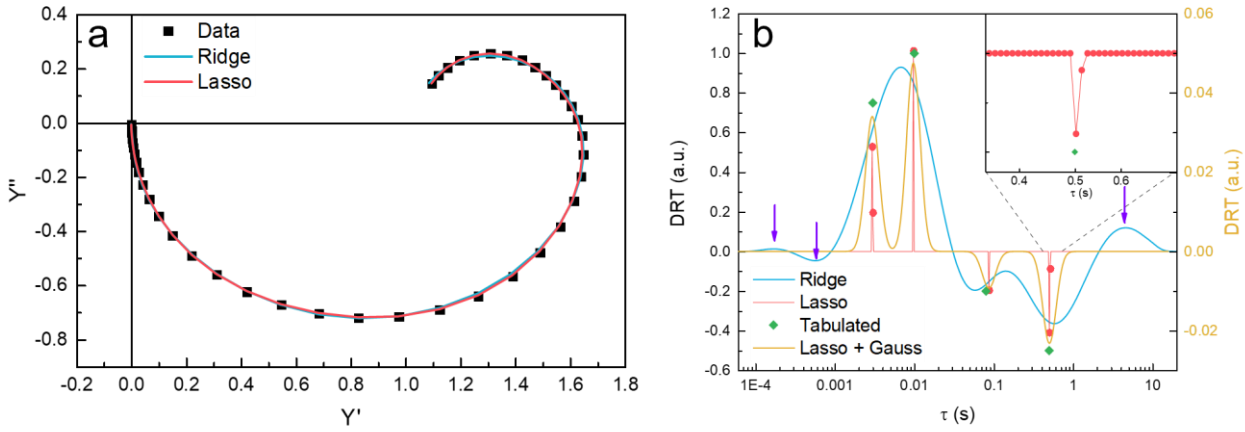

Figure 3.6: *a) IMPS spectrum generated using Equation 3.15 and values in Table 3.1, overlapped with fit curves obtained using Lasso and ridge regression, b) DRT curves calculated using Lasso and ridge regression, together with the Gaussian convolution of the L-DRT (GL-DRT curve); tabulated values $(\tau, g(\tau))$ used for generating the IMPS spectrum are reported as green points. Notice that the y-scale of the GL-DRT curve (yellow) differs from the one of the discrete L-DRT curve (red).*

By applying DRT analysis and fitting this spectrum with Lasso and ridge regression a good reconstruction of the data is obtained, as shown in Figure 3.6a. In fact, the blue and red line fully match every point of the IMPS spectrum.

By focusing on the DRT curves, a huge shape difference between the curves calculated with the two methods (Figure 3.6b) is clearly visible. On one hand, ridge regression is not able to deconvolve the first two positive peaks and, even if the two negative peaks are deconvolved, their positions are shifted

with respect to τ_3 and τ_4 due to the oscillations that give rise to other peaks. In addition, without prior information on the system, the oscillations introduced by ridge regression (see arrows in Figure 3.6b) may be misinterpreted as real elements of the analyzed circuit, introducing an artefact. On the other hand, Lasso regression can find correctly not only the four main peaks centered exactly at $\tau = \tau_n$, but also to return their precise height. In fact, as reported in Table 3.1, there is a good agreement between the tabulated values $g(\tau_n)$ and the height of the peak given by L-DRT. However, it must be noticed that the peak centered at τ_1 = 3 ms and τ_4 = 500 ms are split into two close points (see inset Figure 3.6b). For the sake of clarity, when a peak is split into two or more points, we report the sum of their height. In order to have a more reliable reconstruction of the data and avoiding the multiplication of peaks (i.e. overfitting), it is useful to build on each point τ of the L-DRT a Gaussian curve centered on τ and with full width at half maximum (FWHM) which is equal to the logarithmic spacing between two consecutive frequencies used for the measurement, namely $\mathrm{FWHM} = S \times (\log \tau_{n+1} - \log \tau_{n-1})$, where S is a parameter introduced earlier. The height of the Gaussian is then normalized so that its integral is equal to the value $g(\tau)$. Therefore, the resulting DRT curve will be the sum of several gaussian curves whose heights are close to zero for most of them, and appreciably different from zero only for the few of them centered at τ_n. In the following, we will refer to this curve as the Gaussian Lasso DRT curve (GL-DRT curve). This representation bestows a more reliable description of the simulated dummy system, pointing out the superior solidity of the Lasso approach with respect to conventional ridge regression.

3.3.2 Generalization of the Rate Constant Model

From the previous application we saw that DRT analysis based on Lasso regression is capable of deconvolving close characteristic times and returning the right intensity of the relative process. Now we apply L-DRT to a generalization of the RCM proposed by Peter[121], which describes the photocurrent response of a semiconductor/electrolyte interface to a periodic illumination of the photoelectrode. In the RCM, all the minority charge carriers generated after light excitation are

supposed to accumulate homogeneously along the surface of the semiconductor, then either undergo a charge transfer process to the electrolyte with a rate constant k^{trans} or recombine with majority carriers coming from the bulk with a rate constant k^{rec}. However, in a more realistic picture of the system, a semiconductor's surface is not homogeneous, causing a distribution of accumulation sites for minority carriers. Examples of such systems are very common since they are the results of nanostructured surfaces, decoration with catalysts or heterojunction with porous layers.[122,124,126] Each accumulation site *n* is therefore characterized by a fraction p_n of total hole flux I_{hole} towards the surface, so that $\sum_n p_n = 1$, and two rate constants k_n^{trans} and k_n^{rec}. No charge redistribution among different accumulation sites is considered during the experiment.

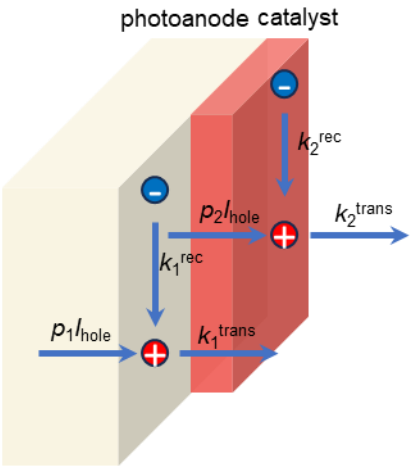

Figure 3.7: *Model of the dynamic processes of charge transfer and recombination when two hole accumulation sites are present. In this case holes are supposed to accumulate and transfer both directly from the surface of the photoelectrode (p_1) or from the catalyst which account for an additional hole transfer/recombination pathway (p_2).*

The general equation that describes the frequency dependent part of the total photocurrent is

$$I_{ph}(\omega) = I_{hole}\left(\sum_{n=1}^{N} p_n \frac{k_n^{trans}+i\omega}{k_n^{trans}+k_n^{rec}+i\omega}\right)\left(\frac{1}{1+i\omega\tau_{cell}}\right), \qquad (3.21)$$

where τ_{cell} is introduced in Equation 3.10. If $N = 1$, Equation. 3.21 returns the simple RCM, where a single state is responsible for the charge transfer/recombination processes.[121] If two accumulation sites are available, corresponding to $N = 2$, there are two possible transfer paths, as schematized in

Figure 3.7. Using Equation 3.21, we can thus simulate IMPS spectra, employing I_{hole} = 1, N = 2, k_1^{trans} = k_1^{rec} = 1, k_2^{trans} = k_2^{rec} = 10 and p_n ranging from 0 to 1. The resulting spectra together with the relative fit and DRT are reported in Figure 3.8.

From these calculations we can extract some important features in IMPS spectra and GL-DRT curves. As expected, IMPS spectra are characterized by one negative semicircle at high frequency and a distorted positive semicircle at lower frequencies. On the other hand, in GL-DRT curves there is only one positive peak at low characteristic times (high frequencies), while more than one negative peak appears at higher characteristic times (low frequencies), except for the boundary cases with p_n = 0 and p_n = 1, where only one negative peak is displayed. The positive peak is centered exactly at RC = τ_{cell} = 10^{-5} s, meanwhile the other negative peaks are centered at $\tau_1^{max} = (k_1^{trans} + k_1^{rec})^{-1}$ = 0.5 s and $\tau_2^{max} = (k_2^{trans} + k_2^{rec})^{-1}$ m= 0.05 s.

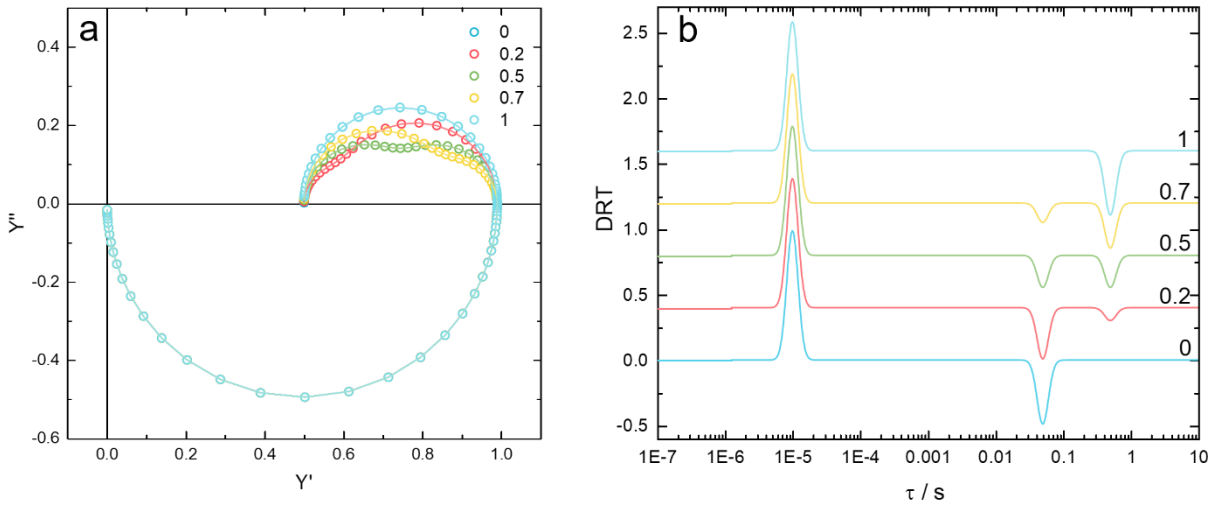

Figure 3.8: *a) IMPS spectra generated using* $\tau_{cell} = 10^{-5}s$, $p_1 = 0, 0.2, 0.5, 0.7, 1$ *and* $N = 2$ *with* $k_1^{trans} = k_1^{rec} = 1$ *and* $k_2^{trans} = k_2^{rec} = 10$, *together with their fit curves obtained using* $\lambda = 0.5$. *b) GL-DRT curves (in this case positive peaks are normalized to 1).*

As seen in the previous paragraph, the peculiar feature of the L-DRT algorithm is to return not only the right position of the peaks but also their height. In order to extract the height of the peaks that appears in the GL-DRT curves, it is necessary to rearrange Equation 3.21 in a form of an admittance similar to Equation 3.15, which allows the $g(\tau_n)$ factor for every addendum to be identified, as follows:

$$\frac{I_{ph}(\omega)}{\phi_{inc}} = \frac{I_{hole}}{\phi_{inc}}\left(\frac{1}{1+i\omega\tau_{cell}}\right)\sum_n p_n \frac{k_n^{trans}+i\omega}{k_n^{trans}+k_n^{rec}+i\omega} = \frac{I_{hole}}{\phi_{inc}}\left(\frac{1}{1+i\omega\tau_{cell}}\right)\sum_n p_n \frac{k_n^{trans}-k_n^{rec}+k_n^{rec}+i\omega}{k_n^{trans}+k_n^{rec}+i\omega} =$$

$$\frac{I_{hole}}{\phi_{inc}}\left(\frac{1}{1+i\omega\tau_{cell}} - \frac{1}{1+i\omega\tau_{cell}}\sum_n \frac{p_n\eta_n^{rec}}{1+i\omega\tau_n^{max}}\right), \quad (3.22)$$

where $\eta_n^{rec} = \frac{k_n^{rec}}{k_n^{trans}+k_n^{rec}}$ is the fraction of accumulated minority carriers that recombine with majority carriers coming from the bulk. Apart from the normalization factor I_{hole}/ϕ_{inc}, which is constant and does not depend on ω, Equation 3.22 differs from Equation 3.15 because of the factor $(1 + i\omega\tau_{cell})^{-1}$ in front of the summation; however, this factor becomes appreciably different from 1 only at high frequencies, say $\omega\tau_{cell} \gtrsim 0.1$. In this range, the summation vanishes because $\tau_n^{max} \gg \tau_{cell}$, leading to $\omega\tau_n^{max} \gg 1$ and $(1 + i\omega\tau_n^{max})^{-1} \approx 0$. This situation reflects the fact that the summation represents the low-frequency limit of the admittance, which is dictated by the long (compared to τ_{cell}) characteristic times τ_n^{max}. It is therefore legitimate to approximate the second, low-frequency term of Equation 3.22 by setting $(1 + i\omega\tau_{cell})^{-1} \approx 1$:

$$\frac{I_{ph}(\omega)}{\phi_{inc}} = \frac{I_{hole}}{\phi_{inc}}\left(\frac{1}{1+i\omega\tau_{cell}} - \sum_n \frac{p_n\eta_n^{rec}}{1+i\omega\tau_n^{max}}\right) \quad (3.23)$$

In Equation 3.23 it is useful to set $g(\tau_{cell}) = I_{hole}/\phi_{inc}$ and $g(\tau_n^{max}) = g(\tau_{cell})\, p_n\, \eta_n^{rec}$. If $k_n^{rec} \gg k_n^{trans}$ then $\eta_n^{rec} = 1$, meaning that all the minority carriers accumulated at the n-th sites recombines before going into the solution. On the other hand, if $k_n^{rec} \ll k_n^{trans}$ most of the minority carriers escape recombination and pass in the solution. At steady-state, i.e., $\omega = 0$, Equation 3.23 becomes:

$$\frac{I_{ph}(0)}{\phi_{inc}} = \frac{I_{hole}}{\phi_{inc}}(1 - \sum_n p_n\eta_n^{rec}) = \frac{I_{hole}}{\phi_{inc}}(1 - \sum_n p_n(1 - \eta_n^{trans})) = \frac{I_{hole}}{\phi_{inc}}\sum_n p_n\eta_n^{trans} = \frac{I_{hole}}{\phi_{inc}}\eta_{LD}^{trans} \quad (3.24)$$

where $\eta_{LD}^{tr} = \sum_n p_n\eta_n^{trans}$ is the L-DRT transfer efficiency.

As expected, Equation 3.24 suggests that the total steady-state photocurrent $I_{ph}(0)$ is given by the sum of the photocurrent that comes from every accumulation site. Equation 3.24 can be also written by

making explicit the efficiencies of the main optoelectronic processes involved in PEC systems, i.e. light harvesting efficiency (LHE), charge separation efficiency (CSE)[129], transfer efficiency $\eta_{\mathrm{LD}}^{\mathrm{trans}}$ and external quantum efficiency (EQE). This results in:

$$\frac{I_{\mathrm{hole}}}{\phi_{\mathrm{inc}}}\sum_n p_{\mathrm{n}}\eta_{\mathrm{n}}^{\mathrm{trans}} = \mathrm{LHE}\times\mathrm{CSE}\times\eta_{\mathrm{LD}}^{\mathrm{trans}} = \mathrm{EQE} \tag{3.25}$$

and therefore $\frac{I_{hole}}{\phi_{inc}} = g(\tau_{cell}) = \mathrm{LHE}\times\mathrm{CSE}$

The IMPS signal at steady state, i. e. when $\omega = 0$, can be expressed as:

$$\frac{I_{ph}(0)}{\phi_{inc}} = g(\tau_{cell}) - \sum_n g(\tau_n^{max}), \tag{3.26}$$

where

$$g(\tau_{\mathrm{cell}}) = I_{hole}/\phi_{inc} \tag{3.27a}$$

$$g(\tau_n^{max}) = g(\tau_{cell})p_n\eta_n^{rec} \tag{3.27b}$$

with $\eta_n^{rec} = \frac{k_n^{rec}}{k_n^{trans}+k_n^{rec}}$ representing the fraction of accumulated minority carriers that recombine with majority carriers at the surface of the semiconductor (recombination efficiency). Equation 3.27b suggests that the parameters $g(\tau)$ obtained with the L-DRT analysis have an important physical meaning when associated to the generalized RCM of a PEC system. In fact the value $g(\tau_{\mathrm{cell}})$ represents the fraction of holes accumulated at the surface of semiconductor/electrolyte interface with respect to the total amount of incident photons which is, by definition, the product LHE × CSE. In the RCM this quantity is the intercept with the real axis at medium frequencies. Instead, the value $g(\tau_{\mathrm{n}}^{\mathrm{max}})$ represents the fraction of accumulated minority carriers at surface (in the *n*-th site) that undergo recombination with majority carriers coming from the bulk with respect to the total amount of incident photons.

However, Equation 3.27b shows that it is not possible to determine both k_n^{trans} and k_n^{rec} for each accumulation site, since $g(\tau_n^{max})$ is proportional to the products $p_n\eta_n^{rec}$. The following equation is obtained by putting together all the parameters extracted from L-DRT analysis, i. e., $g(\tau_{cell})$, $g(\tau_n^{max})$, and τ_n^{max}, giving:

$$\frac{g(\tau_n^{max})}{g(\tau_{cell})\tau_n^{max}} = p_n k_n^{rec} \tag{3.28}$$

This relation highlights that the peak intensity of a DRT spectrum cannot be directly correlated only to the kinetic rate constant k_n^{rec} and k_n^{trans} without knowing the fraction of holes p_n that follow each path. If the various p_n can be estimated by complementary time-resolved spectroscopic techniques[134,135], then a full quantitative analysis of each peak in the DRT spectrum can be achieved. Nevertheless, even without knowing p_n, the L-DRT approach provides a more effective description of the charge dynamics at the semiconductor/electrolyte interface, compared to the RCM based on the shape of the IMPS curve in a Nyquist plot. Figure 3.9 summarizes the main parameters that are determined from the L-DRT analysis.

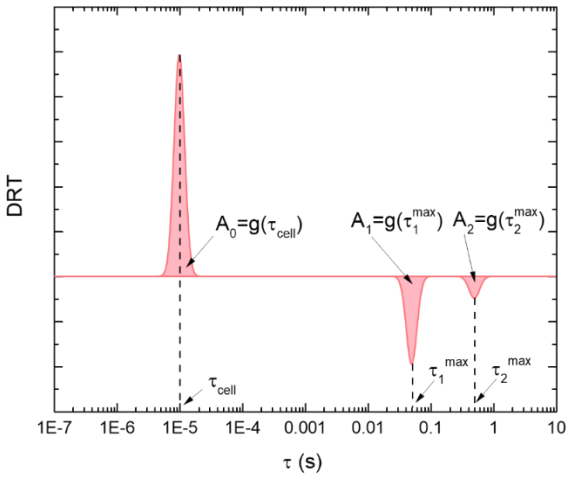

Figure 3.9: *GL-DRT curve reported together with the main parameters coming from the L-DRT analysis. A_0, A_1, A_2 are the integrals (area, highlighted in pink) of the respective gaussian centred at $\tau_{cell}, \tau_1^{max}$ and τ_2^{max}. Notice that the height of the Gaussian peak is normalized so that its integral is equal to the value $g(\tau_n)$.*

Indeed, $g(\tau_n)$ parameter obtained using L-DRT algorithm can be readily used for calculating other important physical quantity, such as the Gartner current $I_{Gartner}$[136] and the recombination current I_{rec}. In several works,[121,124,125,137] it was pointed out that the photocurrent measured in the external circuit is given by the difference between the flux of holes towards the surface $I_{Gartner}$ (given by the Gartner equation) minus the recombination current of electrons I_{rec} with holes trapped at the surface. These two currents have opposite sign since both electrons and holes flow toward the surface:

$$I_{ph} = I_{Gartner} - I_{rec} \tag{3.29}$$

Comparing Equation 3.29 with Equations 3.26 and 3.27b, it is possible to write that $I_{\mathrm{Gartner}} = \phi_{\mathrm{inc}} g(\tau_{\mathrm{cell}}) = I_{\mathrm{hole}}$ and $I_{\mathrm{rec}} = \phi_{\mathrm{inc}} \sum_n g(\tau_{\mathrm{n}}^{\mathrm{max}})$. L-DRT provides an easy separation of the Gartner current $I_{Gartner}$ from the recombination current I_{rec}.

Furthermore, L-DRT enables an easy calculation of the rate constants k_{LD}^{trans} and k_{LD}^{rec}, which are the rate constants that describe the overall dynamic behaviour at the semiconductor/electrolyte interface of the photoelectrochemical system. This can be achieved by approximating a system characterized by N negative peaks to a system with a single negative peak and transfer efficiency η_{LD}^{trans}. This peak will be characterized by a time constant τ_{LD}^{max}, given by the average of all the τ_n^{max} relative to negative peaks weighted by their intensity $g(\tau_n^{max})$:

$$\tau_{LD}^{max} = \frac{1}{k_{LD}^{trans} + k_{LD}^{rec}} = \frac{\sum_n g(\tau_n^{max}) \tau_n^{max}}{\sum_n g(\tau_n^{max})}. \tag{3.30}$$

We can thus write the following equation:

$$\eta_{LD}^{tr} = \sum_n p_n \eta_n^{tr} = \frac{k_{LD}^{tr}}{k_{LD}^{tr} + k_{LD}^{rec}} = k_{LD}^{tr} \tau_{LD}^{max}. \tag{3.31}$$

From Equations 3.30 and 3.31 it is now possible to calculate k_{LD}^{trans} and k_{LD}^{rec}. The calculation of such parameters is then independent from the shape of the IMPS curve in the Nyquist plot, providing a more reliable analysis with respect to the graphical analysis used in Peter's RCM.

4 Multi-electron transfer at H-terminated p-Si electrolyte interfaces: large photovoltages under inversion conditions

In this chapter, photovoltages for hydrogen-terminated p-Si(111) in an acetonitrile electrolyte were quantified with methyl viologen [1,1'-$(CH_3)_2$-4,4'-bipyridinium]$(PF_6)_2$, abbreviated MV^{2+}, and $[Ru(bpy)_3](PF_6)_2$, where bpy is 2,2'-bipyridine, that respectively undergo two and three one-electron transfer reductions. The reduction potentials values, $E°$, span a range greater than the 1.12 eV bandgap of Si, enabling a test of the assumption of fixed band edge positions for interfacial electron transfer. Time-resolved and steady-state infrared spectroscopies are introduced as new tools for the characterization of photoelectrochemical cells that provides compelling evidence for a transition from the depletion condition to an inversion layer as the Fermi level is raised above the conduction band edge toward the vacuum level. Kinetic evidence for an accumulation layer at more positive potentials indicates that the H-terminated p-Si acetonitrile electrolyte interface provides access to all four bias conditions known for semiconductors interfaces in the solid state, i.e., accumulation, flat band, depletion, and inversion. The bell-shaped dependence of the surface recombination rate on the surface potential, quantified herein by nanosecond time-resolved infrared spectroscopy, validates a statistical Schockley-Read-Hall (SRH) theory reported over 60 years ago. An important conclusion from this research[22] is that the most optimal photovoltage and surface electron concentration for multi-electron transfer catalysis occur when the acceptor $E°$ value lies above the conduction band edge and not within the bandgap, as is normally assumed.

4.1 Results

Cyclic voltammograms of an CH_3CN solution containing stoichiometric concentrations (1 mM) of methyl viologen (MV^{2+}) and ruthenium tris-bipyridyl $[Ru(bpy)_3]^{2+}$ with 100 mM $TBAPF_6$ electrolyte are shown in Figure 4.1a.

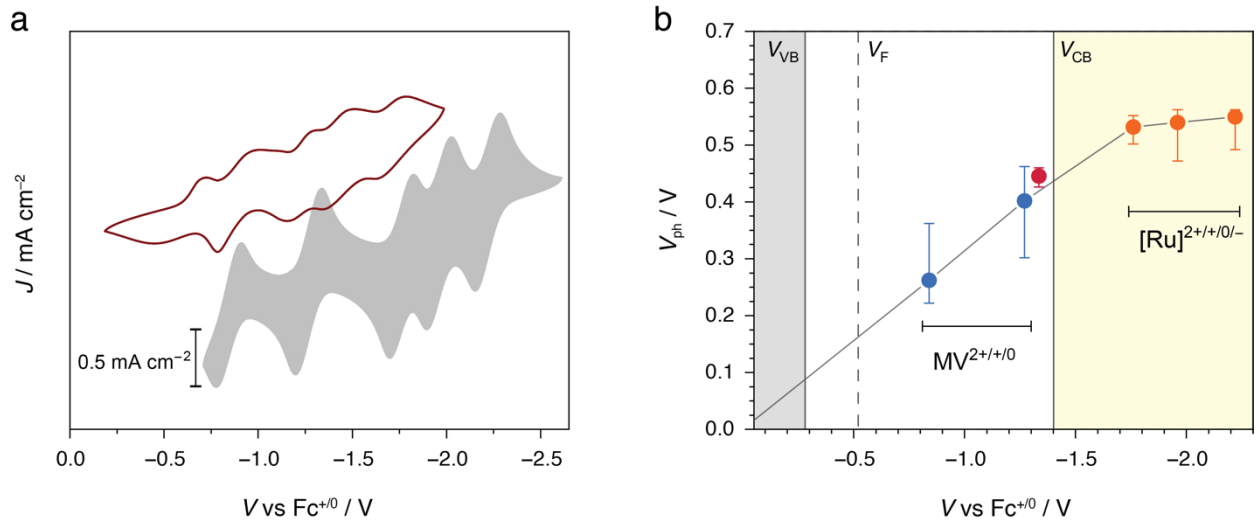

Figure 4.1: *a) Cyclic voltammograms of MV^{2+} and $[Ru(bpy)_3]^{2+}$ (at 1 mM each) measured at 100 mV s^{-1} with a degenerately doped n^+-Si (gray scale) and p-Si(111) (red) illuminated with 34 mW/cm² of 650 nm light. b) Plot of the median photovoltages measured with the p-Si electrode for the indicated redox process versus the reduction potentials, with the minimum and maximum values indicated by the error bars. The magenta datapoint refers to measurements conducted with $CoCp_2$. Superimposed areas in gray and light yellow are the energetic positions of the p-Si valence and conduction bands at the estimated flat band condition.*

Voltammograms were measured in the dark with a degenerately doped n^+-Si electrode as well as with a glassy carbon electrode (data not shown, but results were identical to those shown for n^+-Si), and with an illuminated (λ_{ex} = 650 nm, 34 mW cm^{-2}) p-Si photoelectrode; no waves were observed over this potential window in the absence of band gap illumination. The data show two sequential MV^{2+} waves and three sequential $[Ru(bpy)_3]^{2+}$ waves. The half-wave potentials, $E_{1/2}$, as an approximation for the reduction potentials, $E°$, were in good agreement with previous reports.[113] The voltammograms were stable and could be measured over periods of hours without significant change, consistent with a previous report.[93] The half-wave potentials, $E_{1/2}$, were much less negative at the illuminated p-Si electrode (E) than those measured with a glassy carbon (GC) electrode or a degenerately doped n^+-Si electrode ($E°$). This was also true for cobaltocene ($CoCp_2$) that was measured independently. The photovoltage, V_{ph}, defined as the difference in the measured reduction potentials for the illuminated p-Si relative to the dark n^+-Si, i.e., $V_{ph} = E_{1/2}$(p-Si) – $E_{1/2}$(n^+-Si), determined for at least eight separate measurements on eight different samples are given in Figure 4.1b and Table 4.1.

Table 4.1: *p-Si photovoltages and reduction potentials for the indicated redox couples.*[a]

Redox Couple	V_{ph} / mV (min, median, max)			$E°$ / V (n^+-Si)	E / V (p-Si, median)
$MV^{2+/+}$	220	260	360	−0.84	−0.58
$MV^{+/0}$	300	400	460	−1.27	−0.87
$[Co(Cp)_2]^{+/0}$	433	440	441	−1.33	−0.89
$[Ru(bpy)_3]^{2+/+}$	500	530	550	−1.76	−1.23
$[Ru(bpy)_3]^{+/0}$	470	540	560	−1.96	−1.42
$[Ru(bpy)_3]^{0/-}$	490	550	560	−2.22	−1.67

[a]Reduction potentials are referenced versus the $Fc^{+/0}$ redox couple. Values for illuminated p-Si are statistical reports across 8 independent measurements.

Capacitance data were analyzed with a Mott-Schottky plot, i.e., $1/C^2$ versus the applied potential, between –0.3 and –1.2 V vs $Fc^{+/0}$ with a step size of 10 mV. The capacitance, C, was extracted by modelling the impedance response of the photocathode with a single RC parallel circuit for frequencies greater than 300 Hz. Under these experimental conditions, the capacitance change was on the order of micro-Farads (expected for ideal space-charge layers in most semiconductors) and increased linearly with the applied voltage step between –0.4 and –0.7 V, with no evidence for significant Faradaic current.[138,139] The capacitance data were analyzed with Equation 4.1,

$$\frac{1}{C^2} = -\frac{2}{\varepsilon_0 \varepsilon_r e N_a A^2}\left(V - V_{fb} + \frac{kT}{q}\right) \quad (4.1)$$

where, ε_0 is the dielectric permittivity of vacuum, $\varepsilon_r = 11.7$ is the dielectric permittivity of silicon, q is the elementary unit of charge, A is the geometric area of the photoelectrode in contact with the solution, V is the applied potential, k is the Boltzmann constant, and T is the absolute temperature. Representative Mott-Schottky plots measured from 300 Hz to 100 kHz are given in Figure 4.2 in a 0.1 M $TBAPF_6/CH_3CN$ with 1 mM each of MV^{2+} and $[Ru(bpy)_3]^{2+}$.

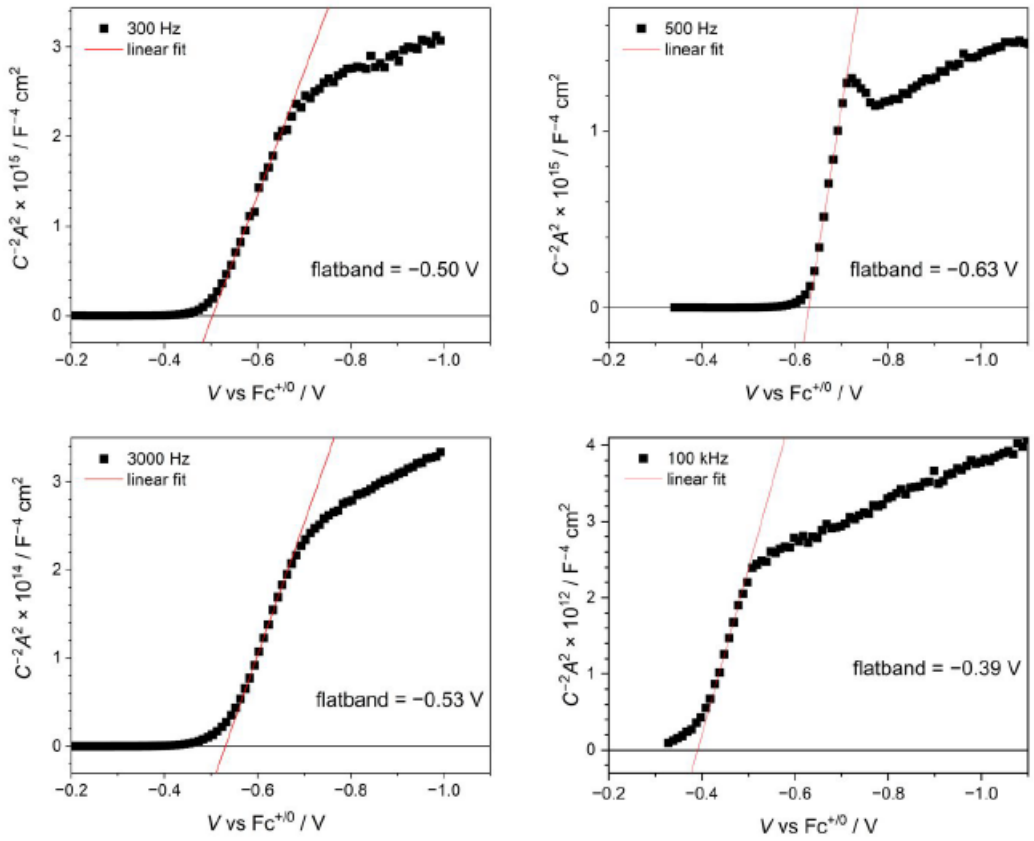

Figure 4.2: *Selected Mott-Schottky analyses of p-Si in electrolyte (0.1M $TBAPF_6/CH_3CN$) containing $[Ru(bpy)_3]^{2+}$ and MV^{2+} (1 mM). The measurements were taken in the dark at the indicated frequencies from 300 Hz to 100 kHz. The flatband potentials, determined by the intersect of the linear fit and the x-axis, are given in each plot.*

The intercept provided an estimate of the flat band potential ($V_{fb} = E_{fb}/e$) with an average value of –0.52 ±0.1 V vs $Fc^{+/0}$ that is in good agreement with previous literature reports for Si in acetonitrile electrolytes, for example V_{FB} = –0.43 V,[93] –0.61 V,[97] and –0.60 V,[140] all versus $Fc^{+/0}$. The slope obtained from the linear fit of the Mott-Schottky plot (Figure below) was used to calculate the acceptor density (N_a) according to Equation 4.2,

$$N_a = \frac{2}{qA^2\varepsilon_r\varepsilon_0 \times \text{slope}} \tag{4.2}$$

The energetic position of the Fermi level (V_F), relative to the intrinsic Fermi energy ($V_{F,i}$), was obtained according to Equation 4.3,

$$V - V_F = \ln\left(\frac{n_i}{N_a}\right) \times kT \tag{4.3}$$

where n_i is the intrinsic carrier density of silicon (1.5×10^{10} cm^{-3}), kT = 0.0259 eV at room temperature, $V_{F,i}$ is the intrinsic Fermi level, and the Fermi level V_F is equal to V_{fb}. The positions of the conduction (V_{CB}) and valence (V_{VB}) band edges were determined using the relations $V_{VB} = V_{F,i} + V_g/2$, and $V_{CB} = V_{F,i} - V_g/2$. V_g is equal to the voltage difference between the valence and conduction band edges (1.12 V), which is the bandgap energy E_g of silicon (1.12 eV). The average flatband potential of −0.52 (±0.1) V vs $Fc^{+/0}$ was determined by Mott-Schottky analysis on 12 different silicon electrodes in the dark at frequencies from 300 Hz to 100 kHz. The dopant concentration, N_a was in the range from 7.34×10^{14} cm^{-3} to 1.52×10^{16} cm^{-3}, which matches the supplier's information of (1 – 20 Ω cm → 1.49×10^{14} cm^{-3} to 6.64×10^{16} cm^{-3}). The average difference of $V_{fb} - V_{VB}$ was determined to be 0.24 (±0.04) eV.

Capacitance measurements made in acetonitrile electrolyte with 10 mM concentrations of MV^{2+} or $[Ru(bpy)_3]^{2+}$ resulted in the same flat band potentials as those measured in the neat electrolyte. The impact of including the reduced form(s) of the redox couples was not investigated herein.

Time-resolved infrared spectra measured at the indicated delay times after pulsed 532 nm excitation of p-Si are shown in Figure 4.3a. The spectra displayed as solid lines were measured in a dry N_2 ambient atmosphere, while the solid circles represent data measured at the open circuit condition in 0.1 M $TBAPF_6/CH_3CN$. Both the spectra and kinetics were largely insensitive to the two environments. Strong absorption by the acetonitrile solvent near 3000 cm^{-1} and below 1600 cm^{-1} precluded measurements in these regions. The absorption increased with the wavelength raised to the second power, behavior consistent with the presence of free carriers (electrons and holes).[140] Spectroelectrochemical data *without bandgap excitation*, Figure 4.3b, also revealed the presence of free carriers when the applied potentials were poised at values more negative than V_{CB}. Stepping the potential back to potentials more positive than V_{CB} revealed that the spectral changes were reversible.

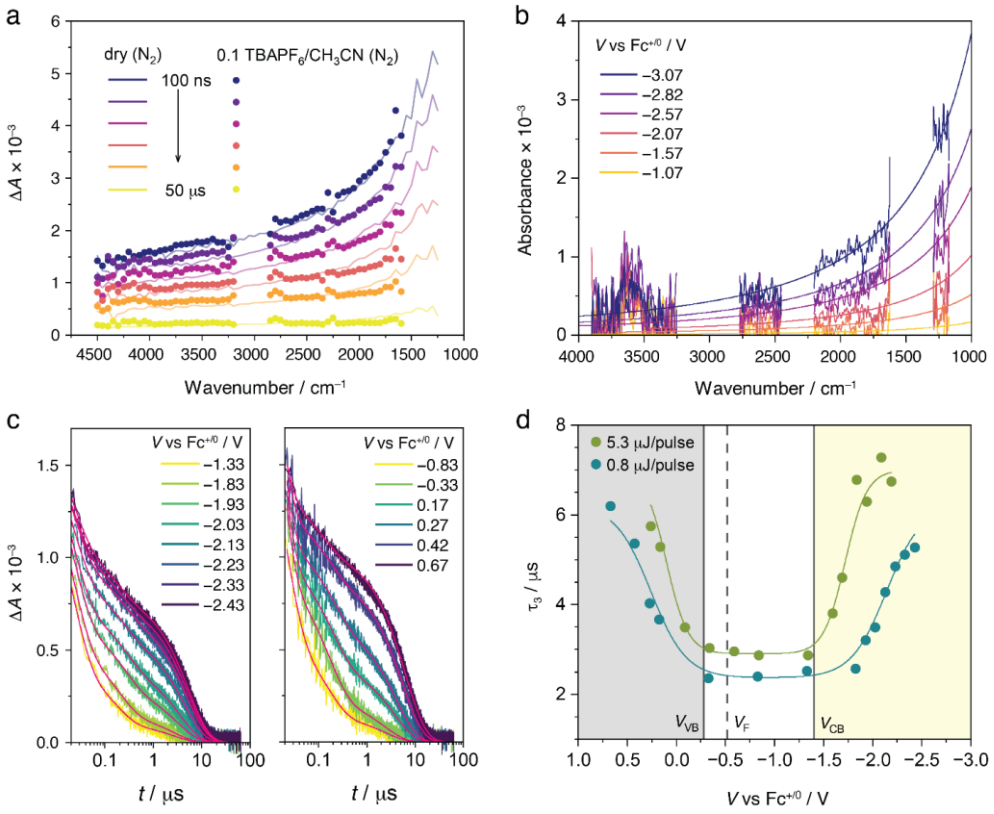

Figure 4.3: *a) TRIR spectra measured 100 ns to 50 µs after pulsed 532 nm laser excitation of p-Si under N_2 (solid lines) and p-Si in 0.1 M $TBAPF_6/CH_3CN$ (circles). b) Spectroelectrochemical IR measurements of p-Si under increasingly negative applied potentials in the dark showing the free carrier generation entering inversion. c) Kinetic data monitored at 2000 cm^{-1} as a function of the applied potential with overlaid kinetic fits. d) Plot of τ_3, assigned to surface recombination, as a function of the applied potential for two light intensity conditions. The band edge positions at the flat band configuration are shown with solid interpolating curves to guide the eye.*

The kinetic data were sensitive to the applied potential and light intensity yet were non-exponential under all conditions investigated. The data were fit to a sum of three exponentials. Kinetic data acquired as a function of the incident irradiance and the applied potential revealed that one of the three components ($\tau_3 = 1/k_3$) was highly sensitive to both parameters while the other two components were not, Tables 4.2 and 4.3.

The irradiance and applied potential-dependent recombination pathway was hence assigned to surface recombination. We note that the term surface recombination velocity (cm/s) is often used to specify recombination at a surface.[141,142] Interestingly, kinetic data measured at applied potentials more negative than −1.0 V vs $Fc^{+/0}$ were far more sensitive to the light intensity than those measured at

more positive applied potentials. Representative kinetic data measured at a fixed light intensity as a function of the applied potential are given in Figure 4.3c.

Table 4.2: *Free-carrier lifetimes in p-Si measured after pulsed 532 nm excitation at 0.8 μJ/pulse.*[a]

Potential V vs $Fc^{+/0}$	τ_1 **ns**	A_1 **%**	τ_2 **ns**	A_2 **%**	τ_3 **μs**	A_3 **%**
–1.33	18	76	151	18	2.49	6
–1.83	20	70	189	21	2.57	9
–1.93	24	62	263	21	3.23	17
–2.03	20	59	247	18	3.49	23
–2.13	18	55	211	16	4.28	29
–2.23	15	55	197	14	4.85	31
–2.33	12	60	170	12	5.10	28
–2.43	12	60	154	12	5.26	28

Table 4.3: *Free-carrier lifetimes in p-Si measured after pulsed 532 nm excitation at 5.3 μJ/pulse.*[a]

Potential V vs $Fc^{+/0}$	τ_1 **ns**	A_1 **%**	τ_2 **ns**	A_2 **%**	τ_3 **μs**	A_3 **%**
–1.34	19	79	208	16	2.94	5
–1.59	19	77	233	15	3.80	8
–1.69	21	74	251	16	4.60	10
–1.84	19	72	259	14	6.77	14
–1.94	21	70	267	16	6.29	14
–2.09	19	70	265	15	7.28	15
–2.19	20	71	260	15	6.75	14

[a]The electrolyte was 0.1M $TBAPF_6/CH_3CN$ and the lifetimes were extracted from a tri-exponential fit of kinetic data monitored at 2000 cm^{-1}. Errors of 1-10% to the extracted lifetimes represent uncertainties from the fit.

4.2 Discussion

This study of multi-electron transfer at H-terminated p-Si/acetonitrile electrolyte interface supports two important conclusions. First, the largest photovoltage values are realized when the molecular reduction potential coincides with the conduction band continuum of the semiconductor, not within the forbidden bandgap as is expected and predicted by Scheme 2.1. Second, all four electric field conditions known for a semiconductor junction in the solid state can also be accessed for semiconductor/electrolyte interfaces in photoelectrochemical cells. These findings are particularly

encouraging for applications that require multi-electron transfer and specifically for the realization of liquid "solar fuels" by CO_2 reduction with p-type hybrid semiconductor photoelectrodes.

These conclusions were garnered from electrochemical and spectroscopic measurements made as a function of the applied potential. Steady-state and time-resolved infrared spectroscopy were identified as particularly valuable experimental tools that distinguished inversion layer formation from Fermi-level pinning, a distinction that has historically been contentious in this field.[143,144] The bell-shaped dependence of the surface recombination rate with the applied potential predicted by a statistical model over 60 years ago was directly quantified through nanosecond transient infrared measurements. Next, we discuss the interfacial energetics measured in the dark, the impact of bandgap excitation, and the impact of these findings on multi-electron transfer catalysis within the context of the broader literature.

4.2.1 Interfacial Energetics.

The approximate band edge positions of p-Si at the flat band condition were extracted from capacitance data while the formal reduction potentials were measured by cyclic voltammetry in a common electrolyte in the absence of bandgap illumination. These data indicate that the two MV^{2+} reductions (blue spheres) fall within the forbidden bandgap while the three $[Ru(bpy)_3]^{2+}$ potentials (orange spheres) are within the continuum of conduction band states, Figure 4.4a.

A literature review reveals that two different semiconductor/electrolyte potential distributions have been invoked to account for photovoltage behavior with interfacial energetics like that for $[Ru(bpy)_3]^{2+}$: 1) Inversion Layer [107,145–148] formation; and 2) Fermi-level pinning (FLP).[113,143,144,149]

In an inversion layer, the surface recombination rate is decreased as predicted by the SRH model.[107,150,151] Under inversion conditions at high injection levels, the intrinsic Auger recombination rate may limit V_{ph},[152–154] but there is no evidence to support this in this study (*vide*

infra). In FLP, intra-bandgap surface states exchange carriers with the bands that may unpin the band edges,[113,143,149] thereby limiting the magnitude of V_{ph} without giving rise to saturation behavior. For example, the presence of a dielectric layer, like SiO_2 on Si, may support a significant potential drop that results in a smaller V_{ph} value than expected.[155] Likewise, semiconductor functionalization with a material that possesses a large density of states, such as redox active monolayers,[98,156,157] may yield a heterojunction with a smaller V_{ph} than that measured in the absence of the material. In the following discussion, focus is placed on inversion layer formation and FLP that give rise to the saturation photovoltage behavior reported herein.

Figure 4.4a provides a comparison of the potential distributions at a p-type semiconductor/electrolyte interface under ideal conditions with fixed band edge positions and in the presence of redox active surface states. As the Fermi level is raised from the flat band condition (reverse bias for a p-type semiconductor), a *depletion layer* is formed where the near surface region is depleted of majority carriers (holes for p-Si). When the Fermi level is raised further, to the point that it crosses the intrinsic Fermi level and is eventually poised above the conduction band edge at the interface, an inversion layer forms. The term *inversion* is used because, under these conditions, the type of majority carriers in the layer *inverts* to its opposite, e.g., electrons become dominant in a p-type semiconductor. Inversion layers are well known at solid-state interfaces such as in metal-oxide-semiconductor field-effect transistors (MOSFETs),[107] but their formation at semiconductor/electrolyte interfaces in photoelectrochemical cells remains less certain.[149] Although less relevant to this study, lowering the Fermi-level from the flat band condition results in an accumulation layer, where majority carriers accumulate in the space charge region.

The potential distribution provided in Figure 4.4a were determined by solving the Poisson equation under the bias conditions of accumulation, flat band, and depletion were determined using the depletion approximation,[107] (Equation 4.4) where $\rho(x)$ is the total charge density.

$$\frac{\mathrm{d}^2V(x)}{\mathrm{d}x^2} = -\frac{q}{\varepsilon_r\varepsilon_0}\rho(x) \tag{4.4}$$

Positive values of x represent the bulk, with the surface fixed at $x = 0$. The conduction band potential at the surface remains fixed to its flat band value, $V_{CB}(0) = V_{CB}$, and at values of $x > 0$, $V_{CB}(x)$ shifts with the applied potential by an amount equivalent to the change in potential relative to flat band, $\Delta V = V_{app} - V_{fb}$. A similar boundary condition was applied to the valence band. Equation 4.4, with the appropriate approximation (depletion vs inversion) and boundary conditions, were solved in Mathematica, resulting in the typical parabolic band bending in the depletion layer.[30] Analytical solutions that more rigorously describe an inversion layer may be provided with additional approximations that consider the effective density of states in the conduction and valence bands with utilization of the Fermi-Dirac distribution.[145,146]

The alternative case of semiconductor/electrolyte potential distribution occurs when a semiconductor has redox active surface states within the forbidden bandgap, Figure 4.4b. Under such conditions, raising the Fermi level from the flat band condition results in Faradaic electron transfer and partial reduction of the surface states. This redox chemistry pins the Fermi level and additional applied potential drops within the Helmholtz region of the electric double layer much like in a metal electrode. This condition is termed Fermi-level pinning (FLP), or sometimes band edge unpinning. Historically, the observation of photovoltages that were insensitive to the formal reduction potential of a redox couple has been taken as direct evidence for FLP;[113,143,144,149,158,159] however, the data reported herein show that the same insensitivity is observed for an inversion layer. Hence additional data are needed to distinguish FLP from an inversion layer.

A key distinguishing feature is the delocalized nature of conduction band electrons in an inversion layer, while a photoelectrode under FLP conditions has electrons present in localized surface states and a semiconductor under depletion conditions. For silicon, these surface states have historically been found at energies close to the intrinsic Fermi level.[107] The spectroelectrochemical IR data

reported here reveal the appearance of a long wavelength absorption as the Fermi level is raised to about –1.5 V vs $Fc^{+/0}$ that is lost when the potential is stepped back to more positive values. Free carrier absorption increases with wavelength raised to the second power, while trapped electrons in surface states are expected to show an absorption maximum.[140,160,161] Therefore, the IR spectral data are most consistent with the presence of conduction band electrons in an inversion layer. Additional evidence for an inversion layer, as well as the other electric field conditions, was extracted from kinetic measurements made after bandgap excitation as described below.

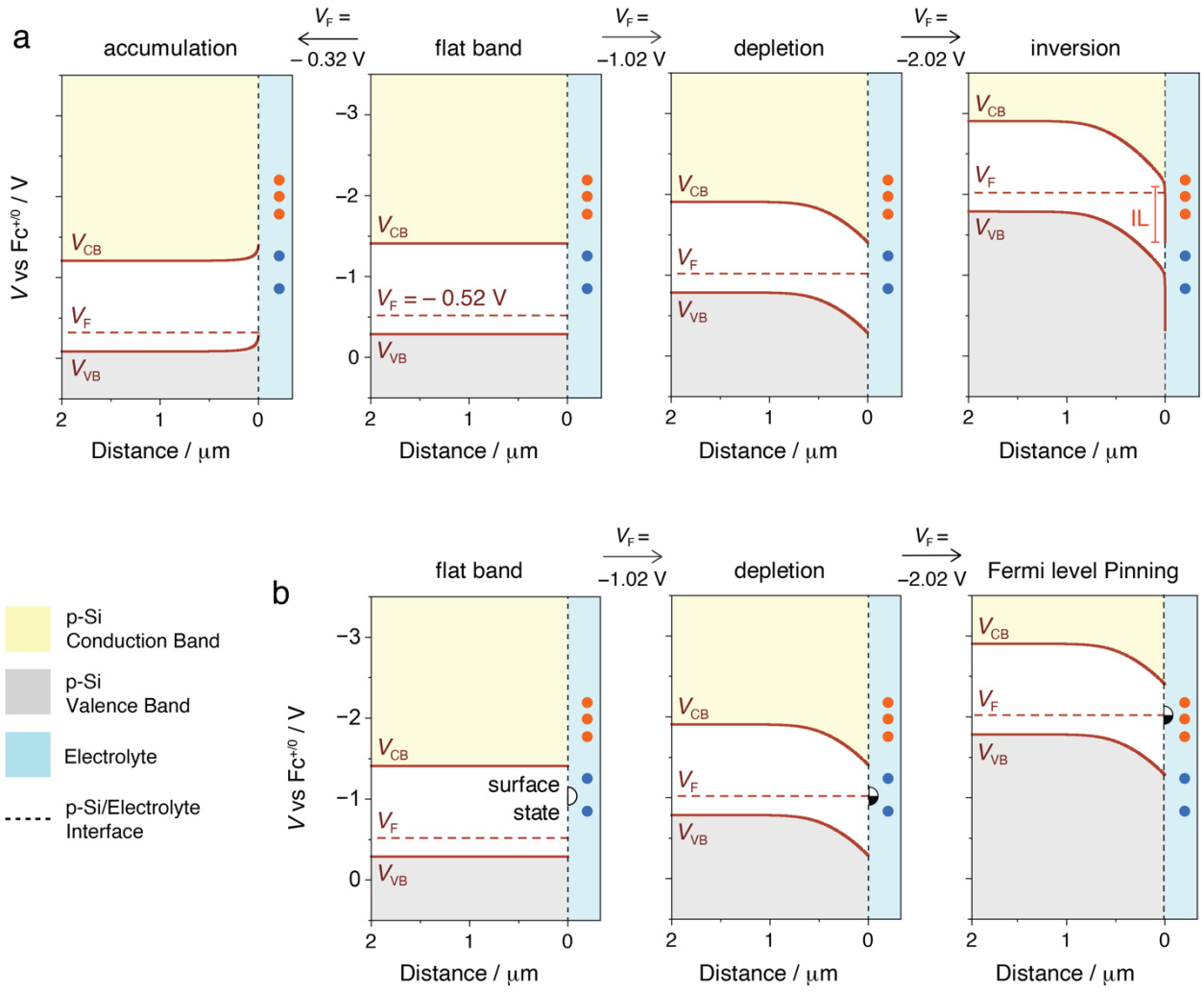

Figure 4.4. *a) Band diagrams for an ideal surface with valence band (V_{VB}), Fermi level (V_F) and conduction band (V_{CB}) calculated as a function of the distance inside the semiconductor from the surface and applied potential for a H-terminated p-Si in contact with electrolyte without bandgap excitation. b) Fermi level equilibration with an applied potential for an interface with silicon surface states (represented by partially filled black semicircles) leading to Fermi level pinning.*

Reduction potentials for MV^{2+} (blue circles) and $[Ru(bpy)_3]^{2+}$ (orange circles) are included for comparison with the band diagrams.

4.2.2 Bandgap Excitation

It is worthwhile to consider Figure 4.4a with the assumption of isoenergetic electron transfer from fixed band edge positions. The first and second reductions of MV^{2+} by illuminated p-Si are expected and indeed observed as the potential for both redox couples lie within the forbidden bandgap. In contrast and contrary to experiment, the $[Ru(bpy)_3]^{2+}$ reductions lie within the continuum of conduction band states where efficient interfacial electron transfer is not expected based on Scheme 2.1.

Under depletion conditions, the electric field serves to separate charge, sweeping conduction band electrons toward the interface and valence band holes toward the bulk. Ideal photoelectrochemical behavior is well established in the literature under depletion conditions for a variety of semiconductors with ideal behavior often judged by plots of V_{ph} vs $E°(A^{0/-})$.[30,31] The data reported here for the two viologen reductions are also fully consistent with depletion conditions and ideal behavior. The V_{ph} value for the second reduction, $MV^{+/0}$, is larger than the first, $MV^{2+/+}$, because the reduction potential is closer, but still below, the conduction band edge.[114] This energetic alignment leads to larger band bending in the dark, where it is hypothesized that larger electric fields reduce the concentration of holes at the surface, decreasing the effective rate of electron-hole pair recombination at the surface, therefore leading to a larger photovoltage.

Experimentally, the largest V_{ph} values were measured for $[Ru(bpy)_3]^{2+}$ that were, within experimental error, the same for all three redox couples. The consistent trend in the measured V_{ph} was: $MV^{2+/+}$ (260 mV) < $MV^{+/0}$ (400 mV) < $CoCp_2^{+/0}$ (450 mV) < $Ru^{2+/+}$ (530 mV) ~ $Ru^{+/0}$ (540 mV) ~ $Ru^{0/-}$ (550 mV). Historically, a constant photovoltage measured over a 440 mV range of $E°$ would be attributed to FLP. The larger photovoltage values would indicate surface states located energetically near V_{CB}. Indeed, by analogy to semiconductor-metal junctions that produce photovoltages insensitive to the

metal work function, photoelectrochemists assigned FLP to semiconductor-electrolyte interfaces where the photovoltage was insensitive to $E°(A^{0/-})$. This analogy was described in three back-to-back papers published in *J. Am. Chem. Soc*.[113,144,162] However, negligibly small shifts in V_{ph} may also result when the quasi-Fermi level is raised further into inversion – as an inversion layer is formed, the band bending, and consequently the electric field, in the depletion region of the space charge layer saturates, and the excess potential drops in the Helmholtz planes of the electric double layer. Hence both FLP and inversion layer conditions may lead to V_{ph} values that are independent of $E°(A^{0/-})$. Both Gerischer and Nozik have previously suggested that behavior attributed to Fermi-level pinning could instead be a result of an inversion layer.[147,163] A Faraday Discussion on this topic noted that distinguishing FLP from an inversion layer was particularly problematic when the surface state energy was close to a band edge.[163]

The long wavelength absorption identified in spectroelectrochemical data is reasonably assigned to conduction band electrons and provides compelling evidence for the formation of an inversion layer when the applied potential is more negative than V_{CB}. These spectral data support previous evidence for inversion layer formation at semiconductor-electrolyte interfaces garnered through photo-capacitance and conductance measurements.[147,148]

Time-resolved infrared (TRIR) experiments following pulsed bandgap excitation provided additional evidence for this assignment and allowed the electron-hole pair lifetimes to be quantified. Historically, the recombination of photogenerated carriers has been quantified by time-resolved microwave conductivity measurements.[159,164–166] An advantage of the TRIR approach is that it enables *in situ* measurements in a photoelectrochemical cell as a function of the applied potential. When plotted as a rate contant, $k_3 = 1/\tau_3$, and normalized to the maximum value, $k_3/k_{3,max}$ a *bell-shaped* dependence on the applied potential results, Figure 4.5a. Stevenson and Keyes first reported a bell-shaped dependency of the surface recombination velocity on surface Fermi level position when the semiconductor interface accesses accumulation, flat band, depletion and inversion conditions with

the applied potential consistent with what is now often called the Shockley-Read-Hall (SRH) recombination model.[107,150,151] Such *bell-shaped* behavior is well documented for solid-state junctions,[141,167,168] but to our knowledge has not been kinetically resolved in an operational photoelectrochemical cell.[142]

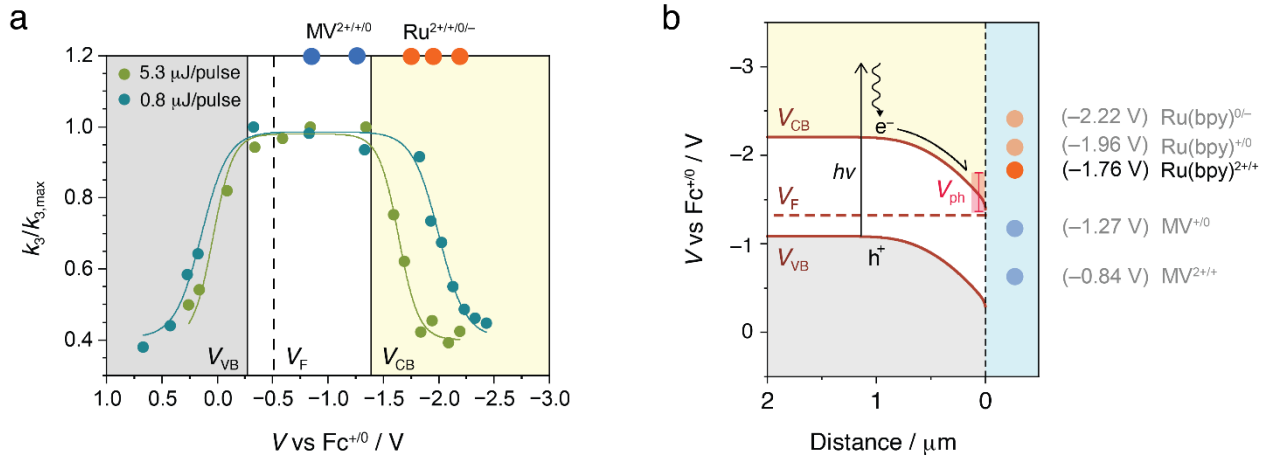

Figure 4.5: *a) Plot of $k_3/k_{3,max}$ versus applied potential extracted from TRIR measurements as a function of the light intensity at low (0.8 µJ/pulse) and high (5.3 µJ/pulse) intensity. The positions of the band edges at the flat band condition are shown in the white area and the curves overlaying the experimental points are a guide to the eye. Reduction potentials for MV^{2+} (blue circles) and $[Ru(bpy)_3]^{2+}$ (orange circles) are included. b) Interfacial energetics at the p-Si electrolyte interface under illumination, taking the first reduction of $[Ru(bpy)_3]^{2+}$ as an example. The indicated photovoltage, V_{ph} = 530 mV, corresponds to that measured by cyclic voltammetry in Figure 4.2a and Table 4.1.*

In the SRH model, recombination is a maximum when the surface potential and electric field are not sufficiently strong to separate electrons and holes; this occurs at the flat band potential which is near the center of the *bell-shaped* curve.[169,170] In contrast, electron-hole pair recombination is inhibited when an inversion layer is present as valence band holes are repelled from the surface and drift toward the bulk resulting in a depleted surface hole concentration. Indeed, the dramatically decreased recombination measured at positive and negative applied potentials are fully consistent with the presence of accumulation and inversion layers, respectively, and are not easily rationalized by other models.[150] If FLP were operative an increased lifetime would not be expected. Rather, the lifetime could decrease, due to carrier trapping by the surface states, or stay approximately the same as the

applied potential falls in the electric double layer, without increased band bending; behavior that is contrary to what was measured experimentally.

Under inversion conditions the kinetic data were far more sensitive to the light intensity than that measured at potentials corresponding to flat band, depletion, or accumulation, Figure 4.5a. This behavior also has precedence in the solid-state literature where photogeneration of large numbers of conduction band electrons favors inversion layer formation.[162,163] Indeed, the first reduction may be very near the conduction band edge in the dark, with bandgap excitation resulting in inversion layer formation, Figure 4.5b. A redox couple with an E^{o} that coincides exactly with the conduction band edge in the dark would likely result in the same photovoltage as that measured in the conduction band continuum and may enter inversion when illuminated.

A switch from depletion conditions in the dark to an inversion in the light is important for photocatalysis and solar fuel applications. The onset of inversion occurs when the surface electron concentration is equal to the hole concentration in the bulk creating an n-type layer on a p-type semiconductor for enhanced charge separation. Strong inversion leads to conduction band electron concentrations of ~10^{20} cm^{-3}.[145,146] At such concentrations the semiconductor exhibits metal-like behavior and the applied potential falls in the electric double layer rather than in the semiconductor itself. This is expected to have a tremendous impact on the structure and composition of the electric double layer. For example, catalysts with large dipole moments would be expected to align with the electric field when illuminated with bandgap light,[171] while electrolyte cations would be electrostatically attracted to the hydrophobic H-terminated Si surface.[172] In future work, such behavior will be specifically examined with surface-sensitive attenuated total reflection infrared techniques and exploited to optimize catalysis with hybrid photoelectrodes.

The impact of these findings on prior photoelectrochemical research deserves some discussion. The photoelectrochemical behavior for H-terminated p-Si reported by Bocarsly and Wrighton and attributed to FLP are likely instead due to inversion layer formation.[113,114,144] Likewise, the large

photovoltages and Faradaic yields reported in Kubiak's pioneering work on CO_2 photoreduction with Lehn's catalyst are also almost certainly due to the presence of an inversion layer.[93] The situation for III-V semiconductors and layered chalcogenide materials is less clear as a high density of surface states might be expected to underlie FLP behavior.[149,173,174] However, as was first pointed out by Dare-Edwards, Bard's description of p-GaAs behaving as if it were coated with a monolayer of metal is more in line with behavior expected for an inversion layer than for electron transfer mediated by poorly defined surface states.[149,151] The data described herein establish the direct spectroelectrochemical detection of conduction band electrons as a general tool for distinguishing inversion from FLP.[166] Alternatively, *in situ* quantification of the surface recombination kinetics, accomplished herein by TRIR, as a function of the applied potential will certainly provide new insights. A decrease in the recombination rate is expected for an inversion layer and it will be of particular interest to test the assertion made herein that the surface recombination rate will increase or stay constant as the Fermi energy of a photoelectrode under FLP conditions is raised toward the vacuum level.

In summary, multi-electron transfer at H-terminated p-Si acetonitrile electrolyte interfaces revealed that the largest photovoltages are realized when the molecular reduction potential has the same energy level as the continuum of conduction band electrons. Steady state and time-resolved infrared spectroscopic measurements indicated that this behavior is due to the presence of an inversion layer, a surface layer where the dopant type has changed from p- to n-type. The inversion layer provides a high $\sim 10^{20}$ cm^{-3} surface electron concentration that supports multi-electron transfer with reduction potentials that span a 440 mV range. Therefore, the conundrum raised at the beginning of this section and in Scheme 1 for optimizing multi-electron transfer, rather than a single transfer, is shown by experiment to be inconsequential. Indeed, the most ideal behavior was observed under inversion conditions with significantly smaller photovoltages generated when the reduction potential was within the forbidden bandgap. The photoelectrochemical behavior of the illuminated p-Si electrolyte

interface under inversion conditions suggests an Ohmic-like semiconductor-molecule interface with the advantages of solar light harvesting to 1100 nm and metal-like behavior. The bell-shaped recombination kinetic data indicates that all four of the semiconductor electric field conditions known for solid state semiconductor junctions can also be accessed in photoelectrochemical cells. These behaviors are particularly encouraging for the realization of “solar fuels” by multi-electron transfer catalysis with hybrid semiconductor photoelectrodes.

5 WO_3/$BiVO_4$ photoanodes studied by wavelength-dependent intensity modulated photocurrent spectroscopy

To gain a detailed and consistent picture of the processes occurring at the WO_3/$BiVO_4$ interface of the photoanode, its performance was compared to pristine colloidal WO_3. In this section we show a complete structural and functional characterization and apply an innovative approach to investigate the photoinduced carrier dynamics, based on the implementation of wavelength-dependent IMPS (WD-IMPS) analysis,[23] where the different layers of the heterojunction are selectively probed, identifying the charge transport properties in the bulk, at the interface between the two layers and at the surface.

5.1 Structure, Morphology, and Optical Properties

The morphological characterization of the photoanodes is reported in Figure 5.1. Colloidal WO_3 (Figure 5.1a) is characterized by a nanostructured morphology made of aggregated nanoparticles with an average diameter of 45 ± 12 nm, sintered together in a porous 3D network. After electrodeposition of $BiVO_4$ on WO_3 (Figure 5.1b), a homogeneous thin layer appears on the WO_3 nanoparticles, increasing the average size to 52 ± 8 nm. High-resolution transmission electron microscopy (HRTEM) micrographs display crystalline nanoparticles with *d*-spacing compatible with monoclinic WO_3 (Figure 5.1d). Interestingly, the surface of WO_3 colloids did not display a homogeneous compact layer of $BiVO_4$ nanoparticles (Figure 5.1e-f), but rather small (< 10 nm) $BiVO_4$ nanocrystals. While their crystal structure cannot be fully resolved due to beam sensitivity-related instability, the observed interplanar spacings are compatible with distorted scheelite $BiVO_4$. Figure 5.1c shows the X-Ray diffraction (XRD) profiles of the two photoanodes. In agreement with the above HRTEM analysis, WO_3 films exhibit a monoclinic structure, while $BiVO_4$ films show the typical monoclinic clinobisvanite structure (distorted scheelite structure), as previously reported. The WO_3 peak

intensities are the same in all the photoanodes, and the reflections associated to $BiVO_4$ are much lower in intensity than those corresponding to WO_3 due to the different thicknesses of the two layers.

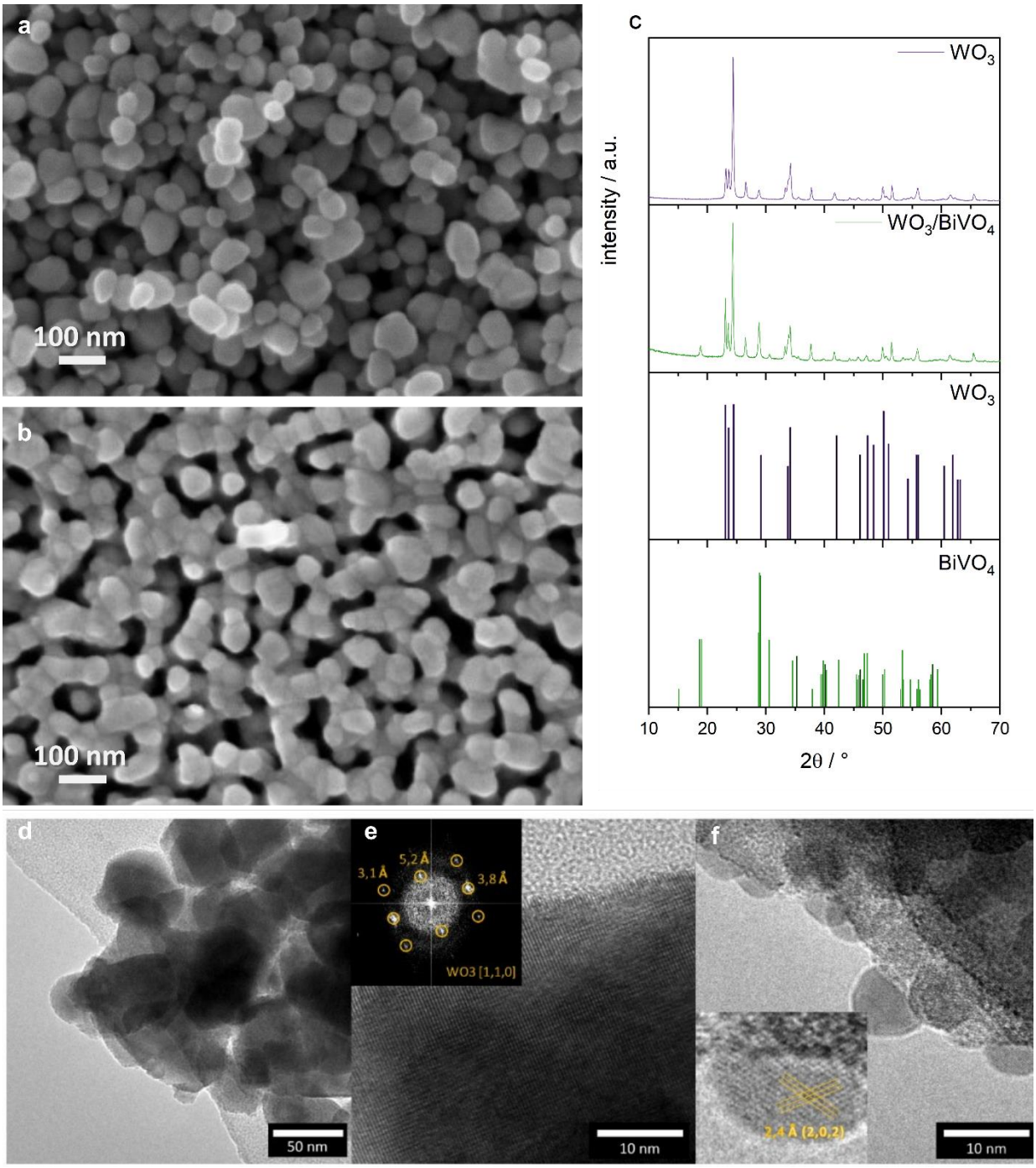

Figure 5.1: *FESEM micrographs of a) WO_3 and b) $WO_3/BiVO_4$. c) The XRD pattern of the prepared photoanodes and reference patterns for WO_3 and $BiVO_4$. d–f) HRTEM micrographs of the $WO_3/BiVO_4$ sample. In the inset: e) Fast Fourier transform displaying the crystal pattern of monoclinic WO_3, oriented on [1,1,0] zone axis. f) Higher-magnification detail of a $BiVO_4$ nanoparticle.*

Figure 5.2 displays the optical absorbance spectra of the WO_3 film and of the $WO_3/BiVO_4$ heterojunction. The spectra are in good agreement with the nominal bandgap energies for WO_3 and $BiVO_4$, that are about 2.7 eV (440 nm) and 2.4 eV (510 nm), respectively.

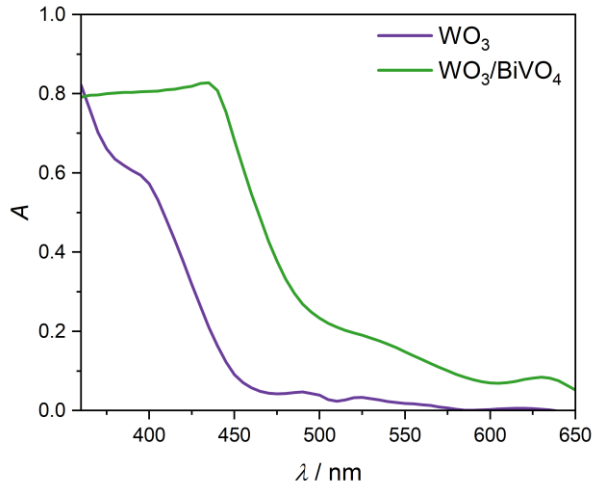

Figure 5.2: *Absorbance spectra of the two studied photoanodes.*

As later discussed in the IMPS result analysis, two different monochromatic LEDs were used to analyze the carrier dynamics of the photoanodes, to excite the $BiVO_4$ layer selectively, or both layers. The LEDs have nominal peak wavelengths of 470 nm and 370 nm and are referred in the text as blue and UV LED, respectively. From the absorbance A, the light harvesting efficiency (LHE) was calculated as:

$$\mathrm{LHE} = 1 - 10^{-A(\lambda)} \tag{5.1}$$

defined as the fraction of light intensity absorbed by the material at each wavelength.

5.2 PEC characterization

The electrochemically active surface area (ECSA) of the WO_3 film gives an estimation of the real surface area involved in the PEC processes and was estimated from the ratio between the double layer capacitance C_{dl} of the solid/electrolyte interface and the specific capacitance C_S of an ideal flat film. A flat tungsten foil was polished and thermally oxidized in order to have a compact WO_3 sheet that could be compared to the colloidal WO_3 photoanode. Their specific capacitances were measured by

EIS in dark at open circuit potential (OCP). Figure 5.3 shows the two EIS measurements and the equivalent circuit used to fit the data.

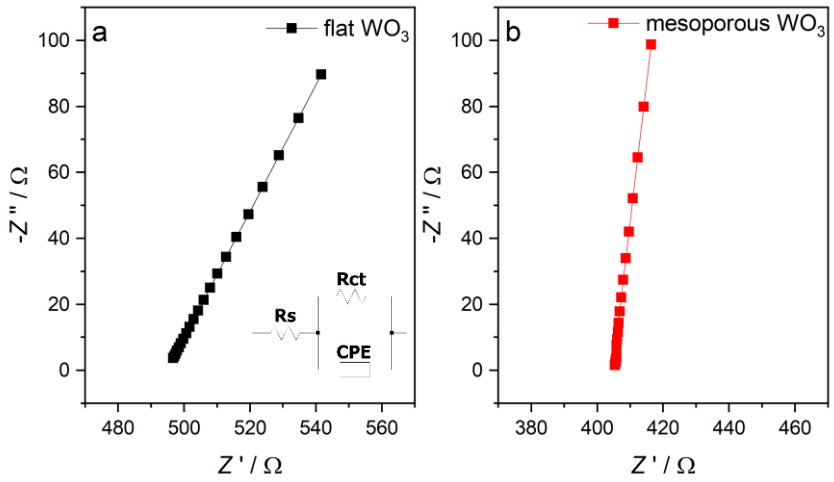

Figure 5.3: *Electrochemical impedance spectroscopy performed in dark at OCP on the a) compact and b) colloidal WO_3 electrodes. Inset: equivalent circuit used to fit the data.*

The impedance of the constant phase element (CPE) is:

$$Z_{CPE} = \frac{1}{Q_0(i\omega)^{1-\alpha}} \tag{5.2}$$

where ω is the frequency of the sinusoidal applied potential, $i = (-1)^{1/2}$, Q_0 is a constant with units of F $s^{\alpha-1}$, and $1 \geq \alpha \geq 0$ is related to the phase angle of the frequency response. For the circuit model used here, C_{dl} is related to the impedance of the circuit elements according to the following Equation:

$$C_{dl} = \left[Q_0 \left(\frac{1}{R_s} + \frac{1}{R_{ct}}\right)^{\alpha-1}\right]^{\frac{1}{\alpha}} \tag{5.3}$$

The compact WO_3 has a C_{dl} of 33.5 µF cm^{-2}, in good agreement with typical values for flat metal oxides found in literature that range from 20 µF cm^{-2} to 80 µF cm^{-2}. On the other hand, the colloidal WO_3 has a C_{dl} of 800 µF cm^{-2}, meaning that the film has an ECSA 24 times higher than that of a compact electrode, and therefore can be considered mesoporous. As the addition of $BiVO_4$ does not significantly modify the morphology of the photoanode, as suggested by field emission scanning

electron microscopy (FESEM) and HRTEM analysis, the whole structure can be considered mesoporous as well.

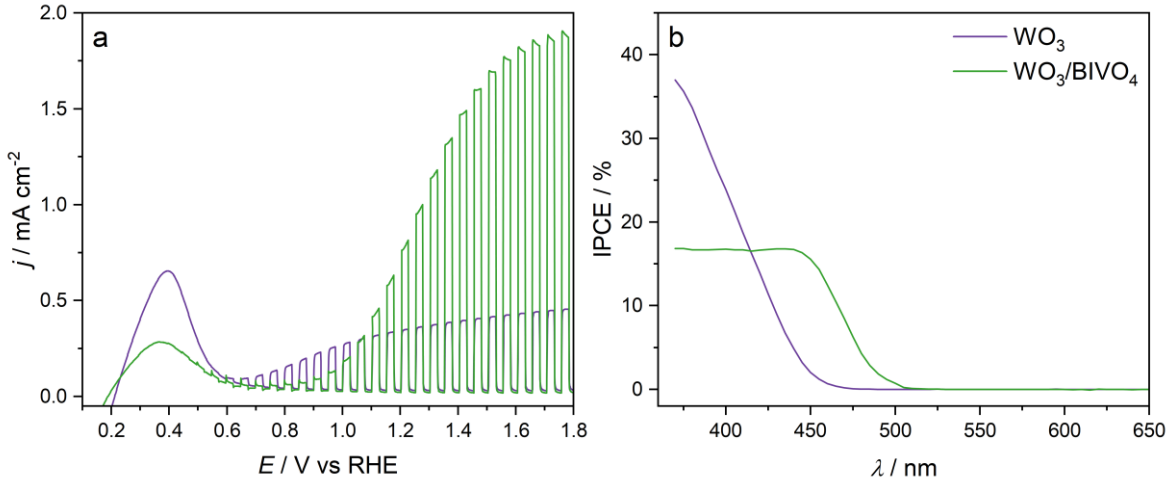

Figure 5.4: *a) Chopped LSV under 1-sun equivalent illumination in acetate buffer solution (pH 5) and b) IPCE spectra at 1.7 V_{RHE} for WO_3 and $WO_3/BiVO_4$ samples.*

Figure 5.4a shows the linear sweep voltammetry (LSV) curves measured in acetate solution under chopped white LED illumination, with an incident of 1 sun. Important contributions of the $BiVO_4$ layer can be noticed with respect to the bare WO_3. In fact, the maximum photocurrent increases more than four times (1.85 mA cm^{-2} at 1.7 V_{RHE}) and shifts the onset towards more positive potentials, requiring a stronger anodic polarization to reach the saturation photocurrent. The current peak observed at 0.4 V_{RHE} is related to the reoxidation of W(V) to W(VI): W(V) is generated during the *j*/*V* experiment upon scanning the electrode at $V < 0.7$ V_{RHE} and requires charge compensation, here in the form of Na^+, by the electrolyte. When $BiVO_4$ is present this effect is reduced, but it does not disappear completely; this might be an indication that the WO_3 layer is not completely covered, consistently with the morphological results, and some of the W(VI) ions may still undergo electrochemical reduction at the relevant voltage.

Figure 5.4b shows the incident photon-to current conversion efficiency (IPCE) spectra of the three electrodes under an applied potential of 1.7 V_{RHE}. WO_3 has a high IPCE (up to 35%) in the UV region of the spectrum, whereas the IPCE is almost zero for $\lambda > 450$ nm, as expected as the bandgap is 2.7

eV. When the $BiVO_4$ layer is added, the IPCE is extended toward the visible range, up to ≈ 525 nm. However, the IPCE of pristine WO_3 exceeds the one of $WO_3/BiVO_4$ in the UV region (< 390 nm). The conversion efficiency given by the IPCE is extracted only from the steady-state photocurrent, and to gather information on the carrier dynamics out of equilibrium we turn to WD-IMPS.

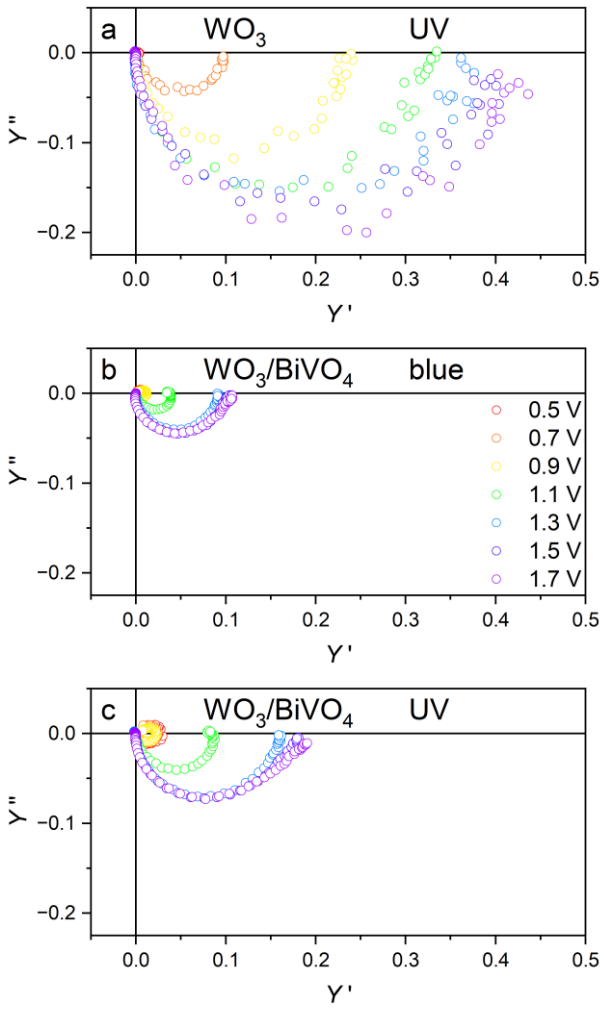

Figure 5.5: *IMPS response of the photoanodes under UV/blue illumination (producing steady-state photocurrent = 35 μA cm^{-2}) in 0.2M acetate buffer solution (pH 5).*

Figure 5.5 shows the IMPS spectra of the two samples under UV and blue monochromatic illumination and at different applied potentials, after normalization according to Equation 3.12. For WO_3 only the measurement with the UV LED is present, as it does not absorb light at 470 nm. For $WO_3/BiVO_4$, using both blue and UV LEDs allows for selective excitation of the different layers of the photoanode, thus identifying the role of each material with respect to the heterojunction PEC

activity. The first row of Figure 5.5 shows the IMPS spectra of the WO_3 photoanode. Upon UV excitation, only the negative semicircle is present, meaning that surface recombination is much slower than charge transfer from the electrode to the solution. On the other hand, the IMPS spectra of $WO_3/BiVO_4$ photoanodes show positive semicircles, indicating surface recombination up to 1.1 V_{RHE}, that disappears at more anodic potentials for both light sources, in agreement with another work on $BiVO_4$. The only difference between UV and blue illumination is given by the value of real-axis intercepts, which is related to the CSE and EQE efficiency of the electrode.

From the IMPS data we can extrapolate the relative efficiency of each optoelectronic process taking place in the PEC cell. The CSE versus applied potential is reported in Figure 5.6a. Upon blue excitation, the CSE of $WO_3/BiVO_4$ displays a sigmoidal shape with onset at about 0.9 V_{RHE} and the maximum CSE value in the high polarization regime (1.5 V_{RHE}) is around 17%. Under UV light, the WO_3 photoanode shows the highest CSE, as it reaches values around 50%. Therefore, it appears that the presence of the $BiVO_4$ layer partly reduces the collection of charges photogenerated within WO_3. Moving to the analysis of the TE (Figure 5.6b), while pristine colloidal WO_3 exhibits unitary TE in the whole considered potential window upon UV illumination, the addition of $BiVO_4$ layer introduces superficial recombination at potentials lower than 1 V_{RHE}, with all excitation sources. Thus, $BiVO_4$ in the low-potential regime is less efficient than WO_3 in transferring charges to the solution, meaning that the number of holes that effectively oxidize water decreases because of competing recombination. This is consistent with the shifted photoanodic onset if the $WO_3/BiVO_4$ junction with respect to bare WO_3. Indeed, only when reaching a sufficiently strong anodic polarization, electrons are drawn away from $BiVO_4$ and the electron/hole recombination process at the surface become negligible.

The EQE versus the applied potential is shown in the right column of Figure 5.6c. With blue LED, we observe a 10.6% value for $WO_3/BiVO_4$, while upon UV illumination, the EQE reaches a value of 19%. UV-excited bare WO_3 displays a higher EQE in the whole potential range with respect to the heterojunction. The IPCE measured at 1.7 V_{RHE} is in good agreement with the EQE extracted by the

IMPS spectra at the equivalent potential with the corresponding excitation wavelength, validating the theoretical model used to extract these efficiencies from the IMPS measurements. Compared to IPCE, IMPS allows to discern the contribution of each process to the steady-state EQE by resolving the carrier dynamics, revealing whether the EQE is limited by the charge separation in the bulk or by the charge transfer at the interface.

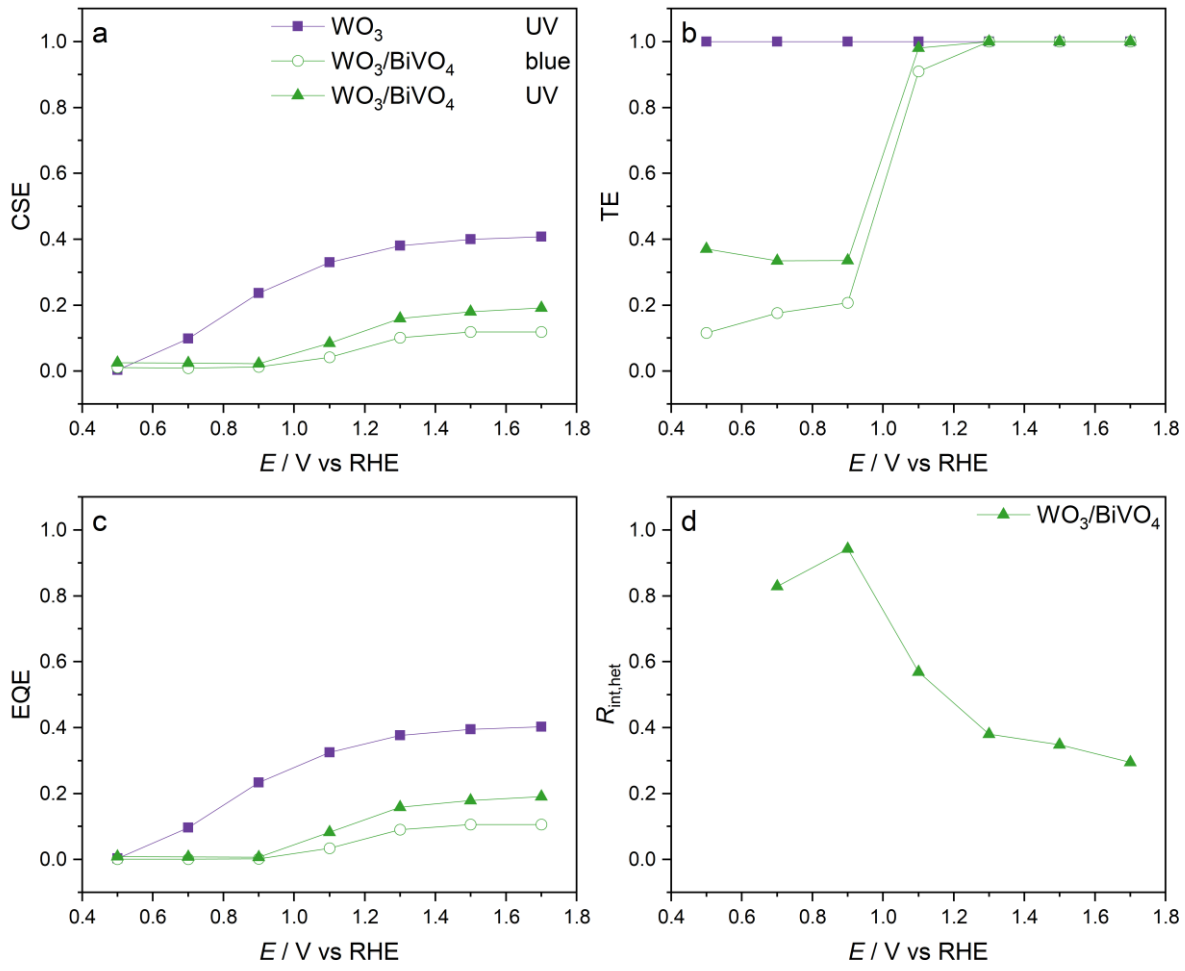

Figure 5.7: *a) CSE, b) TE, and c) EQE of $WO_3/BiVO_4$ when illuminated with blue and UV LEDs; d) $R_{int,het}$ in $WO_3/BiVO_4$*

5.3 Loss at the heterojunction

The main critical point highlighted by this analysis is the improvement of the EQE in the visible region when the heterojunction is formed compared to the pristine WO_3 that shows negligible absorption, but in the UV region the opposite is observed. This drop in EQE might result from either the inner filter effect of the $BiVO_4$ layer, that shadows the incident light on the underlying WO_3, or

the rise of recombination processes related to the heterojunction, or both. A reasonable assumption is that the overall EQE of the heterojunction, at a specific potential, results from the sum of the contributions of each layer, depending on the relative LHE, CSE, and TE:

$$\mathrm{EQE_{het}} = \mathrm{TE_{WO_3}} \times \mathrm{CSE_{WO_3(het)}} \times I_{\mathrm{abs,WO_3}} + \mathrm{TE_{BiVO_4}} \times \mathrm{CSE_{BiVO_4(het)}} \times I_{\mathrm{abs,BiVO_4}} \qquad (5.4)$$

The absorbance of $BiVO_4$ at 370 nm (A_{BiVO4}) is calculated by subtracting the absorbance of WO_3 (A_{WO3}) from the absorbance of the heterojunction (A_{het}). From this calculation, $BiVO_4$ absorbs $I_{abs,BiVO4} = 1\text{-}10^{-A,BiVO4} \approx 19.7$ % of the incident UV light while WO_3 absorbs $I_{abs,WO3} = LHE_{WO3} \times (1 - I_{abs,BiVO4}) \approx 64.4\%$ of it.

We can now reasonably assume $CSE_{BiVO4(het)}$ in the UV region is equivalent to $CSE_{BiVO4(het)}$ under selective $BiVO_4$ illumination in the blue region, as the CSE value at energies above bandgap may be considered independent on the incident photons energy. In addition, CSE_{BiVO4} already includes possible losses of photogenerated carriers that are generated in the $BiVO_4$ layer and recombine at the $BiVO_4/WO_3$ interface. Since the only remaining unknown value in Equation 5.4 is the $CSE_{WO3(het)}$, we can calculate it for every working potential. The resulting value differs from the one observed in pristine WO_3 and is consistently lower. This suggests that additional loss processes are undertaken by the e-h pairs generated in the WO_3 layer within the heterojunction and can be included in $CSE_{WO3(het)}$ as an interface recombination term ($R_{int,het}$) defined as:

$$\mathrm{CSE_{WO_3(het)}} = \mathrm{CSE_{WO_3}} \times \left(1 - R_{\mathrm{int,het}}\right) \qquad (5.5)$$

where CSE_{WO3} is the CSE in pristine WO_3. The EQE_{het} now becomes:

$$\mathrm{EQE_{het}} = \mathrm{TE_{WO_3}} \times \mathrm{CSE_{WO_3}} \times \left(1 - R_{\mathrm{int,het}}\right) \times I_{\mathrm{abs,WO_3}} + \mathrm{TE_{BiVO_4}} \times \mathrm{CSE_{BiVO_4(het)}} \times I_{\mathrm{abs,BiVO_4}} \qquad (5.6)$$

The resulting $R_{int,het}$ as a function of the applied potential in $WO_3/BiVO_4$ is shown in Figure 5.6d, and displays a sigmoidal shape with onset at about 0.9 V_{RHE}. In the $WO_3/BIVO_4$ electrode, as part of the

electroactive WO_3 surface could be directly contacted by the electrolyte, we would expect the occurrence of direct hole-scavenging pathways from WO_3 to the liquid phase, but the high $R_{int,het}$ of the heterojunction for potentials lower than 0.9 V_{RHE} suggests that the large majority of holes generated inside WO_3 are instead lost due to interfacial recombination with $BiVO_4$. For higher applied potentials, $R_{int,het}$ rapidly decreases, probably due to the stronger depletion field built at the $WO_3/BiVO_4$ junction that facilitates the separation of the charge carriers, the transport of the photogenerated holes to the VB of $BiVO_4$, and the injection in the electrolyte. It is however interesting to observe that even when the $R_{int,het}$ plateau is reached in the high polarization regime (1.7 V_{RHE}), its minimum value is 53%, corresponding to the fraction of photogenerated holes recombining at the $WO_3/BiVO_4$ interface, before being effectively transferred across the heterojunction.

Charge recombination at the interface and poor transfer kinetics of holes in solution are the main limitations highlighted from this WD-IMPS analysis. Co-Fe mixed overlayers have shown remarkable improvements in the overall charge carrier kinetics of the $WO_3/BiVO_4$/heterojunction. The effect of this surface modification was studied by TAS and IMPS and the results are shown in the next chapter.

6 Analysis of the effect of Co-Fe overlayers on the kinetics of $WO_3/BiVO_4$ heterojunctions

Surface modification has been widely studied to further enhance the performance of $WO_3/BiVO_4$ photoanodes for photoelectrochemical water splitting, as it can increase the photocurrent and shift the onset potential. In particular, the integration of cobalt iron oxide (CoFeOx)[78,175] or cobalt iron Prussian blue (CoFe-PB)[23,176] overlayers onto $WO_3/BiVO_4$ heterojunctions displays significant enhancement in charge separation leading to decreased recombination at the surface and improved overall efficiency.

The intricate processes describing this enhancement can be unraveled by means of time-resolved techniques. In this Chapter a transient absorption spectroscopy analysis (TAS) on $WO_3/BiVO_4$ photoanodes coated with cobalt iron oxide and cobalt iron Prussian blue overlayers, that investigate the charge carrier kinetics from the picosecond to second timescale is presented. After understanding the kinetics at the ultrafast time scale, an intensity modulated photocurrent spectroscopy (IMPS) study is presented to compare the surface kinetics of modified heterojunctions with the pristine photoanode.

6.1 PEC Characterization

The deposition of mixed CoFe co-catalysts is resulting in a dramatic enhancement of the photoelectrochemical performance of oxide semiconductors. Figure 6.1a reports the linear sweep voltammetries under chopped AM 1.5G illumination of a nanostructured $WO_3/BiVO_4$ semiconductor photoanode in slightly basic environment (green line), superimposed to the ones registered from the same material upon the deposition of a thin layer of mixed cobalt/iron oxide (CoFeOx), and of a Co-Fe hexacyanoferrate, a Prussian Blue analogue (CoFe-PB). The PEC performance improvement is remarkably similar for either CoFe-PB and CoFeOx, both resulting in a deep improvement of the photocurrent onset potential, while the saturation current is only slightly enhanced by the

photoanode's surface modification. For both oxide co-catalysts no oxidation wave is observed in the expected potential region for Co^{2+}/Co^{3+} oxidation. We observe that the presence of the catalytic overlayer does not substantially improve the limiting photocurrent of $WO_3/BiVO_4$, but mostly affects the activation region of the *j*/*V* characteristic causing the cathodic shift mentioned before.

IPCE spectra (Figure 6.1b) are in agreement with this observation: at low anodic bias, i.e., 0.8 V_{RHE}, the electrodes modified with the overlayers mentioned above nearly double the photon to electron conversion with respect to the unmodified junction, while showing nearly identical photoconversion efficiencies in all electrodes once a sufficient anodic bias is provided to them.

These data thus suggest that, at low/intermediate bias a larger hole population is able to escape recombination and reach the interface with the electrolyte when an overlayer is present, giving rise to enhanced photon to electron conversion. When the bias is strong enough, the performance of the various electrodes is levelled and a saturation region, evident from both the IPCE spectra and the *j*/*V* curves, is achieved in all cases. This condition is ostensibly determined by the achievement of the widest possible depletion region inside the semiconductor, likely limited by the size and doping density of the smaller $BiVO_4$ nanoparticles decorating the larger WO_3 structures.

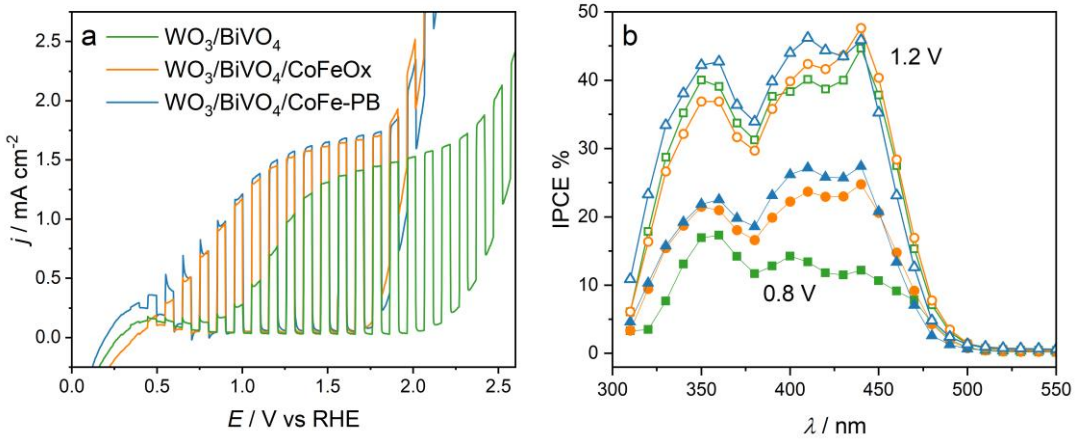

Figure 6.1: *a) Chopped linear sweep voltammetry (Scan rate 50 mV/s, AM 1.5G illumination in borate buffer 0.5M) and b) incident photon-to-current conversion efficiency measurements at different applied potentials on indicated samples.*

6.2 Transient Absorption spectroscopy

Operando transient absorption spectroscopy (TAS) is used here to elucidate the intricate charge carrier dynamics and interfacial processes that govern the performance of this PEC system. The processes that limit the performance of the unmodified $WO_3/BiVO_4$ heterojunction and the beneficial effect of the two overlayers have been investigated on very different timescales and usually focus only on ultrafast kinetics[41,42,120,177] or on slow kinetics, when the water oxidation reaction already takes place.[176,178–180] In this section, the first TAS analysis of $WO_3/BiVO_4$ heterojunctions whose surface was modified by addition of CoFeOx and CoFe-PB is reported. Moreover, it is the first study that spans several orders of magnitude, from picoseconds to seconds, offering a unique perspective on the dynamic processes occurring within the photoanode system, and providing valuable insights into charge carrier dynamics and interfacial reactions.

Ultrafast TAS experiments were carried out in the 10^{-12} s to 10^{-9} s range using excitation by a 100 fs laser pulse with wavelength of 430 nm and energy of 5 μJ/pulse on a 1 mm^2 area. Figure 6.2 compares the TA spectra measured in phosphate buffer 0.1M (pH 7) for the $WO_3/BiVO_4$ photoanodes with and without CoFe-based overlayers. All TA spectra display three main regions in the UV-Vis-NIR, in agreement with previous studies on $BiVO_4$ and $WO_3/BiVO_4$ photoanodes: i) a well-defined band centered at about 470 nm can be assigned to trapped holes in $BiVO_4$[181] and corresponds to transitions from the VB into IBG states emptied by ultrafast (≈ 1 ps) trapping of photoexcited holes;[41,120,179] ii) a broad band between 550 nm and 700 nm (partly convoluted with oscillations due to thin-film interference) is assigned to intraband transitions of free holes in the valence band;[41,120,179] iii) a broad TA in the NIR arises from intraband transitions of free electrons in the CB.[182,183]

Since the IBG states responsible for hole trapping are mainly located in proximity of the $BiVO_4$ surface and are known to represent a crucial step for water oxidation,[176,179] we focus the analysis on the main band at 470 nm by following its decay as a function of time, as summarized in Figure

6.3. The best-fit parameters obtained in various time domains are summarized in Figure 6.4. The charge recombination and transfer processes inferred from the analysis are depicted graphically in Scheme 6.1 to provide a comprehensive view of the overall kinetics and to support the discussion.

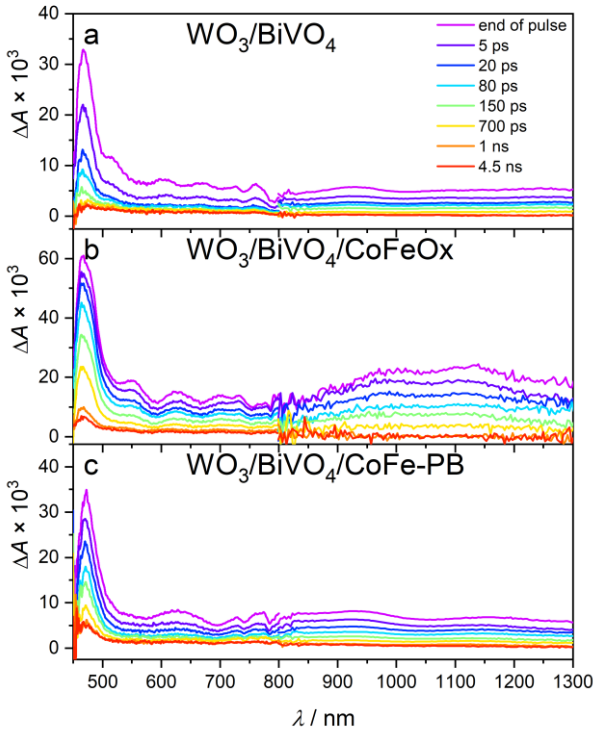

Figure 6.2: *Transient absorption difference spectra measured after pulsed 430 nm (100 fs, 5 μJ/pulse) excitation of a) $WO_3/BiVO_4$, b) $WO_3/BiVO_4$/CoFeOx, and c) $WO_3/BiVO_4$/CoFe-PB at open circuit in phosphate buffer 0.1M (pH 7) after the indicated time delay.*

Figure 6.3a-d-g shows the ultrafast time traces $\Delta A(t)$ monitored at 470 nm and different applied potentials for the three samples. We notice that ΔA(1 ns) is always higher than 1 mOD, meaning that a high number of trapped holes survive recombination in the ultrafast timescale. Therefore, we monitored the decay kinetics on a widely extended range (up to 1 s) using two more instruments that work in the 10 ns – 0.1 ms range (Figure 6.3b-e-h) and in the 1 ms – 1 s range (Figure 6.3c-f-i). In both, we used 6 ns laser pulses with wavelength of 355 nm and energy of 5 mJ on a 1 cm^2 area. The very good matching of the TA amplitudes in the extended time ranges allows them to be directly merged without any normalization. Differently, ultrafast ΔA values are smaller due to weaker excitation conditions, as shown by the discontinuity between the first and second column in Figure

6.3. Nevertheless, the comparison remains fully meaningful because the laser excites both the WO_3 and the $BiVO_4$ layers in all cases. Since the most significant enhancement of the photocurrent induced by the overlayers is observed between 0.6 V_{RHE} and 1.0 V_{RHE} (Figure 6.1a), in the discussion we will pay particular attention to the effect of CoFeOx and CoFe-PB in this potential range.

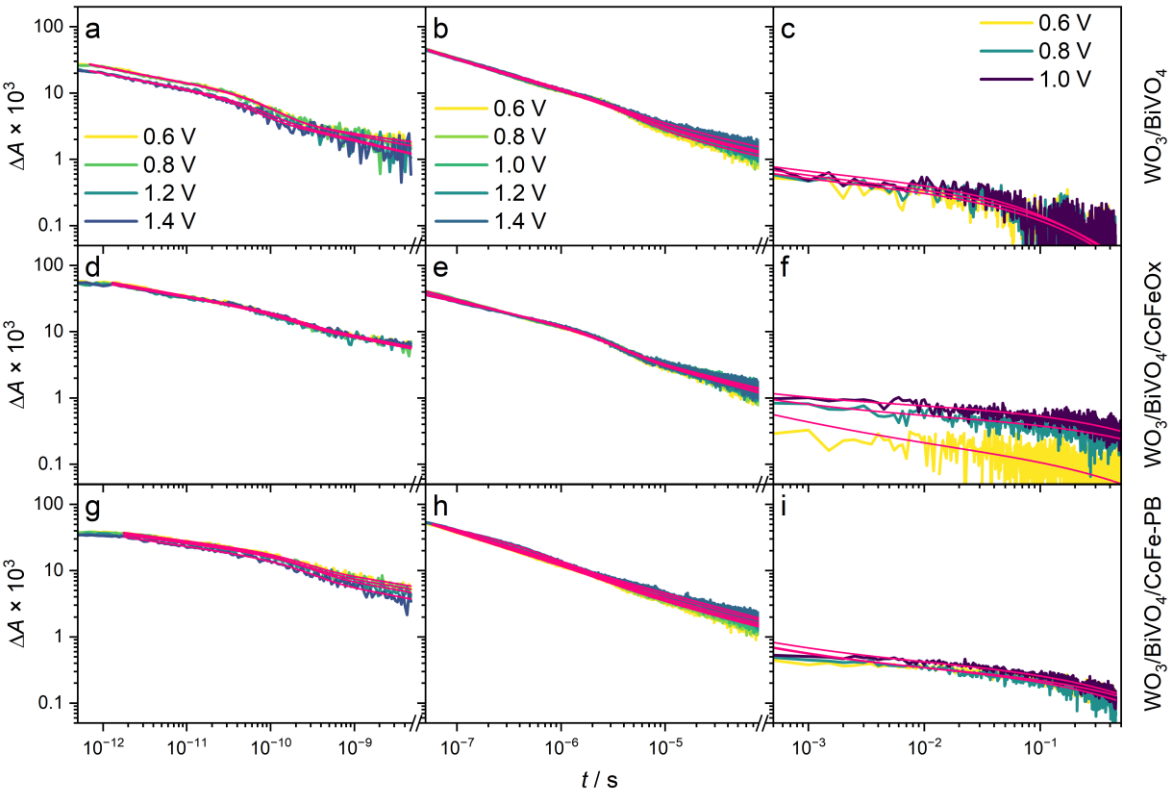

Figure 6.3: *Absorption changes monitored at 470 nm after pulsed (a, d, g) 430 nm (100 fs, 5 µJ/pulse) and (b, c, e, f, h, i) 355 nm (6 ns, 5 mJ/pulse) excitation of (a, b, c) $WO_3/BiVO_4$, (d, e, f) $WO_3/BiVO_4$/CoFeOx, and (g, h, i) $WO_3/BiVO_4$/CoFe-PB at different applied potentials vs RHE in phosphate buffer 0.1 M (pH 7); overlaid are fits to Equation 1 (a,d,g), 2 (b,e,h), and 3 (c,f,i).*

The linear trend visible at ultra-short times in the log-log plot suggests that the initial decay follows a power law, with an additional component present at longer times; therefore, the picosecond kinetic data were fit according to Equation 6.1:

$$\Delta A = B_1 t^{-\alpha_1} + A_1 \exp\left(-\frac{t}{\tau_1}\right) \quad (6.1)$$

Physically, the power law represents diffusion-limited recombination processes involving localized carriers,[117,118] which undergo relaxation within a broadened density of states.[119,120] Therefore,

it is legitimate to assign the power law decay to the recombination of holes trapped at IBG states with free or shallowly trapped electrons undergoing random-like walk within the mesoporous $WO_3/BiVO_4$ structure. This process, which occurs at all time scales and corresponds to the sum of exponential functions with a distribution of characteristic times,[184] is depicted by the blue arrows in Scheme 1. The exponent α_1 is significantly reduced by overlayer addition, from 0.37 – 0.30 in the bare photoanode down to 0.26 – 0.21, whereas the applied field has a small and non-monotonous effect on it (Figure 6.4). Since smaller α_1 values are associated with longer-lived transient signals (Figure 3.2), we infer that the overlayers significantly reduce the diffusion-limited recombination of trapped holes. Typical values of the power law exponent in the literature are in the range 0.2 – 0.5, in good agreement with our results in the ps and in the extended (ns to s) time domain (*vide infra*).[118,120,179]

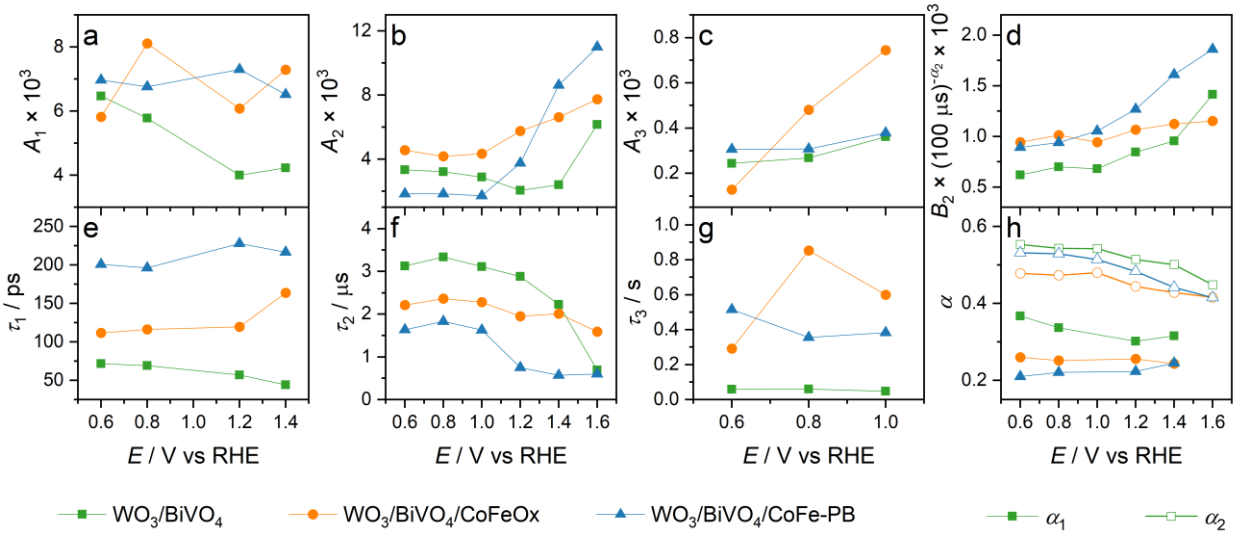

Figure 6.4: *best fit parameters to Equations 1, 2, and 3 for the indicated samples as a function of the applied potential. Exponential amplitudes and time constant at the a,e) picosecond, b,f) nanosecond, and c,g) millisecond timescale; d) power law amplitude after a 100 µs delay; h) power-law exponents α_1 and α_2.*

The exponential decay with a characteristic time τ_1 describes a first-order kinetics that has been assigned in the literature to recombination with free electrons in the CB,[41,42,120] as illustrated by the red arrows in Scheme 6.1. In support of this interpretation, a similar exponential decay with amplitude $A_1^{el} \approx 0.8$ mOD and time $\tau_1^{el} \approx 70$ ps is observed in the time trace of the bare photoanode

at 1000 nm, which is representative of free electrons (See Figure 6.5a). The linear trend visible in the log-log plot suggests that the decay follows a power law, with an additional exponential component present at longer times only for $WO_3/BiVO_4$; therefore, the picosecond kinetic data were fit according to Equations 6.2 and 6.3 for the unmodified and modified heterojunctions, respectively:

$$\Delta A = B_1^{el} t^{-\alpha_1^{el}} + A_1^{el} \exp\left(-\frac{t}{\tau_1^{el}}\right) \tag{6.2}$$

$$\Delta A = B_1^{el} t^{-\alpha_1^{el}} \tag{6.3}$$

Notably, an increasing anodic potential provokes a decrease of both A_1 and A_1^{el}, confirming the link between these recombinative processes.

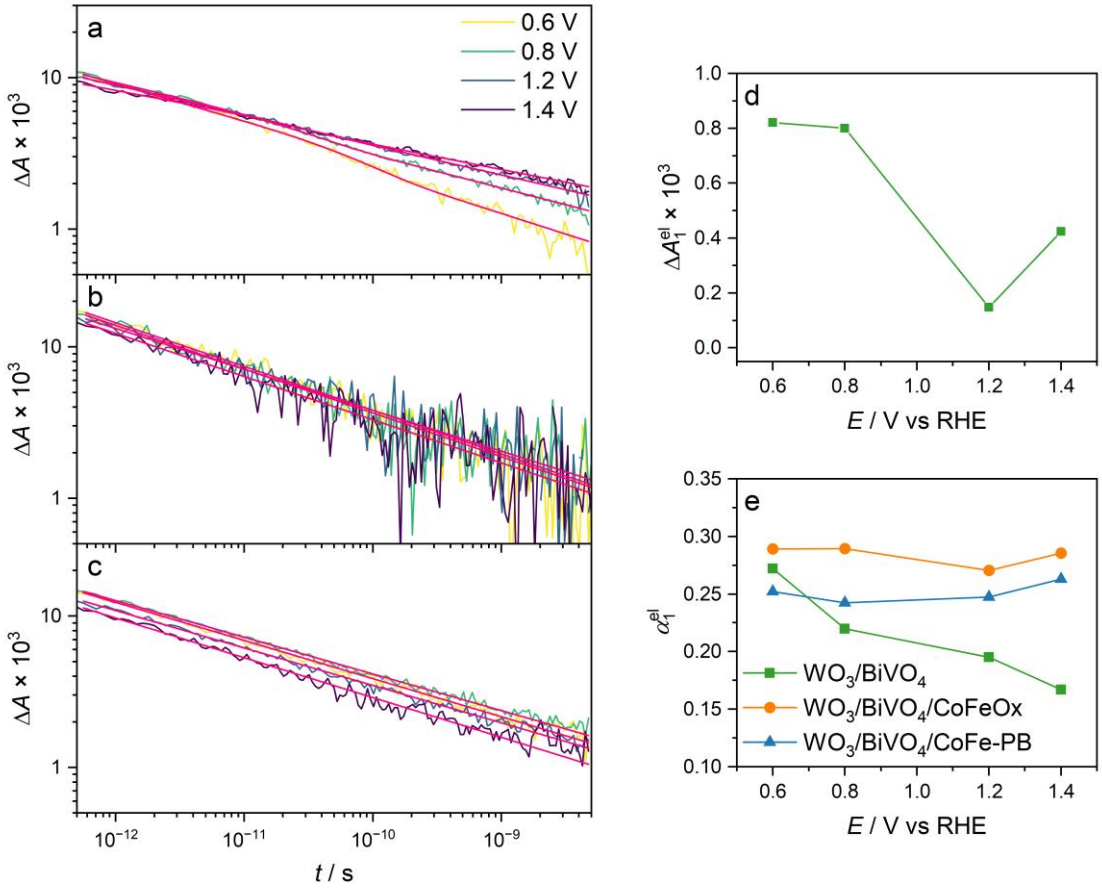

Figure 6.5: *Absorption changes monitored at 1000 nm after pulsed 430 nm (100 fs, 5 μJ/pulse) excitation of a) $WO_3/BiVO_4$, b) $WO_3/BiVO_4$/CoFeOx, and c) $WO_3/BiVO_4$/CoFe-PB at different applied potentials vs RHE in phosphate buffer 0.1 M (pH 7); overlaid are fits to Equation 6.2 for $WO_3/BiVO_4$ and to Equation 6.3 for $WO_3/BiVO_4$/CoFeOx and $WO_3/BiVO_4$/CoFe-PB; d) amplitude*

A_1^{el} measured on $WO_3/BiVO_4$ and e) power law exponent α_1^{el} for indicated samples as a function of the applied potential.

The lifetime τ_1 (Figure 6.4a-e) increases with overlayer addition, rising from 50 – 70 ps in the bare sample to 100 – 150 ps with CoFeOx and 200 – 250 ps with CoFe-PB. Therefore, first-order recombination of trapped holes with CB electrons gets slower after addition of CoFeOx and CoFe-PB overlayers.

In summary, both CoFeOx and CoFe-PB significantly reduce the recombination rate of trapped holes in the ps range, with beneficial effect on the charge separation efficiency. This points to a passivation of recombination centers, possibly associated with dangling bonds, that may also result in an increased band bending at the semiconductor/electrolyte interface due to unpinning of the Fermi level or and the $WO_3/BiVO_4$ heterojunction.

The subsequent dynamics of the charge carriers was investigated by analyzing the 10 ns – 0.1 ms TAS experiments reported in Figure 3b-e-h. Here, the linear trend in the log-log plot of suggests again the presence of an underlying power law decay; in addition, with increasing applied potential, an exponential decay with characteristic time of 1-3 μs becomes more relevant. Accordingly, the time traces were fitted to the sum of a power law and an exponential decay:

$$\Delta A = B_2 t^{-\alpha_2} + A_2 \exp\left(-\frac{t}{\tau_2}\right) \quad (6.4)$$

The power-law decay can again be associated with diffusion-limited recombination of trapped holes. However, by this time most CB electrons have either recombined with holes (lifetime τ_1) or are trapped in states below the CB minimum. Indeed, Ravensbergen *et al*. have identified a characteristic time of 2.5 ns for electronic transition into shallow traps of $BiVO_4$.[120] Therefore, the motion of both diffusing species becomes detrapping-limited (purple arrows in Scheme 1) leading to a change of α_2 with respect to α_1. Another reason for the change of the power law exponent is that recombination is heavily affected by the incident intensity of the laser.[179] The α_2 values reported in Figure 6.4h are close to 0.5, in excellent agreement with the value of −0.49 reported by

Ravensbergen *et al*. in a similar time window.[120] We notice that α_2 decreases slightly with increasing applied potential and by the addition of the overlayers (especially CoFeOx); this translates into a higher density of trapped holes that have survived recombination at a given time t^*, as shown in Figure 6.4d by the value $B_2 \cdot (t^*)^{-\alpha 2}$ (proportional to the trapped hole density) for t^* = 100 µs. Therefore, it appears that the overlayers produce a similar effect as the applied potential in promoting the separation of free or shallowly trapped electrons from the trapped holes. This observation corroborates the suggestion according to which the overlayers enhance the electric field that drive charge separation at the relevant interfaces (*vide supra*).

An important difference between the ps and ns regimes emerges when examining the behavior of the exponential component (Figure 6.4f): in fact, its characteristic time τ_2 drops significantly from ≈ 3 µs of the bare photoanode down to 2 – 15 µs with overlayer deposition at 0.6 V_{RHE} (rather than increasing as τ_1) and further decreases by applying more anodic potentials. Furthermore, its amplitude A_2 rises significantly with increasing potential above 1 V_{RHE}. Therefore, this component describes a depopulation of trapped holes, which is enhanced by both the overlayers and the potential, thus showing the same trend as the photocurrent displayed in Figure 6.1a. This similarity clearly indicates that this process is not representative of charge losses due to recombination, but rather of the transfer of trapped holes towards intermediate charge transfer (CT) states, from which injection into the electrolyte leading to water oxidation and Faradaic photocurrent occurs. In support of this interpretation, Moss et al have shown that the transfer of holes from IBG traps of $BiVO_4$ to the CoFe-PB overlayer is an efficient process that is largely complete by about 10 ms (a time similar to τ_2).[176] Microscopically, this corresponds to the oxidation of Fe and Co cations in the overlayers, e.g. from Co^{3+} to Co^{4+}. Clearly, this characteristic time cannot be associated with direct injection into the electrolyte since this is known to occur on a much longer timescale (*vide infra*). In the case of the bare photoanode, the intermediate CT state can be associated with oxidized species adsorbed in proximity of surface oxygen vacancies in $BiVO_4$[185–187] (e.g., hydroxyl radicals) as well as with

oxidized cations in the overlayer.[176] The intermediate charge transfer state is depicted just outside the $BiVO_4$ layer in Scheme 6.1 and the transfer of trapped holes active at 470 nm is represented by the yellow arrows that become thicker with applied potential and overlayer addition. We remark that such intermediate transfer on a few μs scale, beneficial to the photoelectrochemical performance, was not directly identified in previous studies, apparently because TA experiments were focused on either ultrafast or slow measurements.

Finally, we analyze the kinetic traces collected from 1 ms to 1 s using the sum of a power law and a single stretched exponential (Kohlrausch–Williams–Watts function) with β = 0.5 as a fit function, according to:

$$\Delta A = B_2 t^{-\alpha_2} + A_3 \exp[-(t/\tau_3)^{\beta}] \quad (6.5)$$

where the parameters of the power-law decay have been fixed to those obtained in the previous case (for every sample and potential value); this approach implicitly assumes that the electron-hole recombination described by the power law is the same in the two different time windows, which is reasonable since the intensity and excitation wavelength are the same and the involved charge carriers are trapped in similar states. The KWW decay describes hole injection into the electrolyte leading to water oxidation, with the typical characteristic time of 10s – 100s ms (Figure 6.4g and green arrow in Scheme 6.1).[188,189] This assignment is corroborated by the increase of its amplitude A_3 with the applied potential (Figure 6.4c), i.e in the same range where the photocurrent rises significantly (Figure 6.1), with a particularly strong slope in the case of the CoFeOx overlayer.

We remark that TAS is not able to distinguish between hole transfer directly from the IBG states and via intermediate CT states. In fact, CT states do not contribute to 470 nm TA, but the transfer of a hole from a CT state to the electrolyte (on a several ms scale) can be rapidly followed by hole transfer from IBG states into CT states on a ms time scale (yellow arrow in Scheme 6.1), which is eventually detected as a decay of the 470 nm TA signal. In other words, the kinetics of hole injection via intermediate CT states contributes to the the decay of the trapped holes through fast transfer between

IBG and CT states. Overall, the KWW components describes a combination of different hole injection pathways, i.e., direct and via CT states, which explains the need for a stretched rather than a simple exponential.

Interestingly, we notice that the overlayers extend the characteristic time τ_3 from 47 ms for $WO_3/BiVO_4$ to 380 ms with CoFe-PB and 600 ms with CoFeOx at 1 V_{RHE}. Since the overlayers have a positive impact on the photocurrent, especially in the 0.6-1.0 V_{RHE} range, the increased lifetime cannot reflect a slower injection into the electrolyte that would reduce the water oxidation flow. In order to understand this result, we remind that $\tau_3 = (k^{trans} + k^{rec})^{-1}$, where k^{trans} and k^{rec} are the rate constants for transfer and recombination.[176,179] Therefore, the increased lifetime can be ascribed to a decrease of k^{rec}. A similar explanation in terms of reduced recombination was also proposed by Ma *et al*. to interpret the lifetime increase with increasing V_{RHE} in photoanodes where k^{trans} is potential-independent.[179] Furthermore, this view is fully supported by a intensity modulated photocurrent spectroscopy investigation that is shown in the next section,[23] which revealed that the CoFe-PB overlayer reduces k^{rec} compared to the bare photoanode, while k^{trans} remains unchanged.

In conclusion, the TA kinetics spanning twelve orders of magnitude in time were fitted by simple models invoking a small number of processes and few fitting parameters with a physically sound interpretation. In conjunction with the ample knowledge provided by previous pump-probe studies, precious insights into the effects of CoFe-based overlayers on $WO_3/BiVO_4$ photoanodes were gained, as summarized below:

- Reduction of the power-law recombination rate at all timescales as well as of the exponential recombination in the 10's of ps range, resulting in an improved charge separation efficiency;
- Enhanced transfer of holes on the ≈ 1 ms timescale from intra bandgap traps at the $BiVO_4$ surface to intermediate states associated with oxidized cations in the overlayer, from which charge transfer into the electrolyte can take place at longer times;

- Increased lifetime of the KWW decay associated with water oxidation in the 10's to 100's of ms timescale, indicating that the overlayers boost the photoelectrochemical performance by suppressing surface recombination rather than by accelerating water oxidation kinetics.

These points can be resumed stating that the overlayers act as efficient hole collectors, which enhance charge separation preserving holes from various recombination processes at several timescales, without deteriorating water oxidation kinetics.

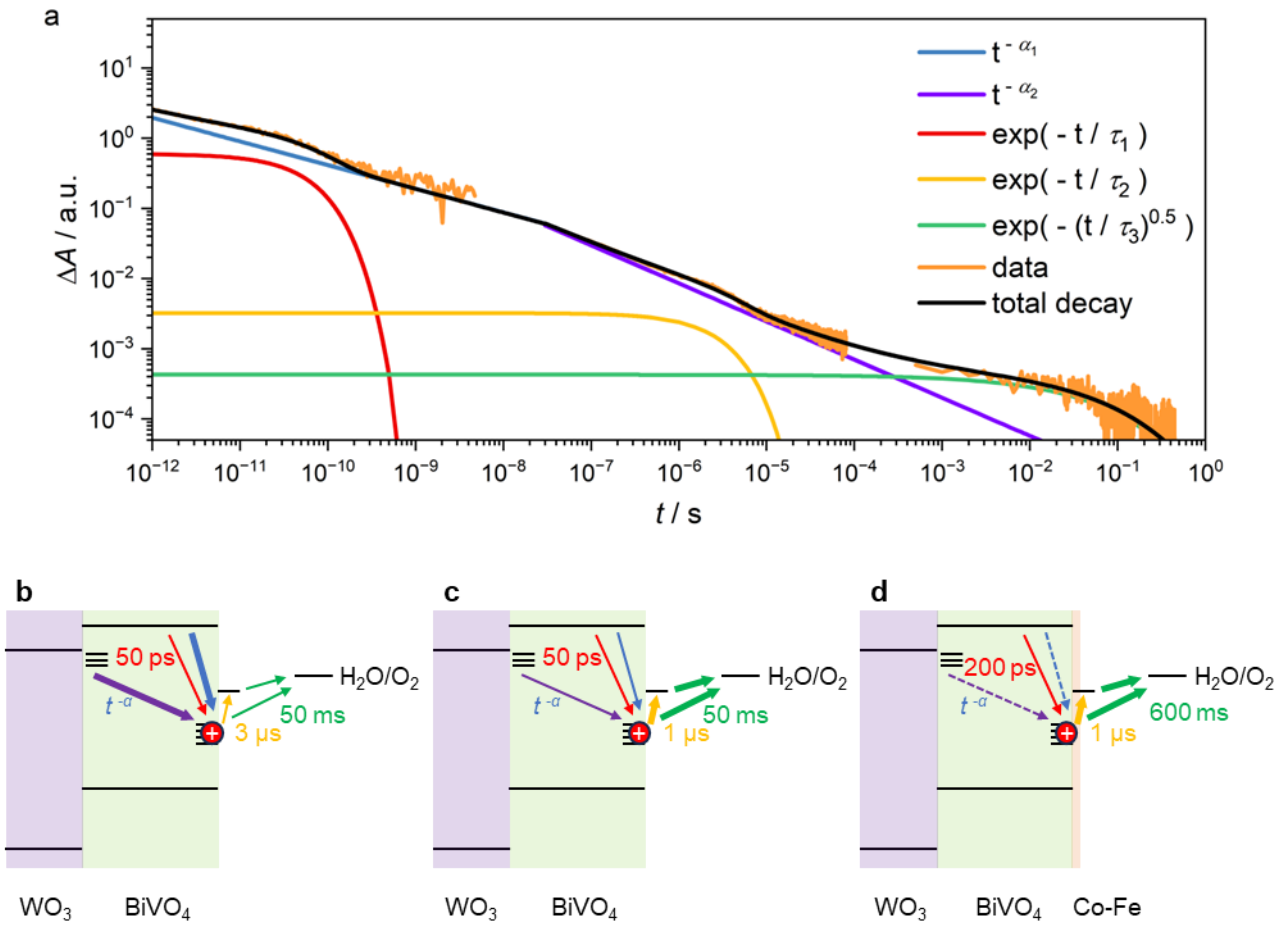

Scheme 6.1: *a) Example of overlayed kinetics from 10 ns to 1 s and relative fit and band diagram showing the relevant detrapping processes at different timescales for b) $WO_3/BiVO_4$, c) $WO_3/BiVO_4$ at higher potential, and d) $WO_3/BiVO_4$ with Co-Fe overlayer. Dashed arrows and thicker arrows represent a decrease and an increase in amplitude, respectively. In a), ultrafast ΔA data have been scaled to provide continuity with those in the ns range. See text for detailed explanation.*

6.3 GL-DRT analysis

In order to gain a deeper insight into the charge carriers dynamics in presence of the two catalysts, IMPS spectroscopy was performed on a bare $WO_3/BiVO_4$ photoanode and on the same photoanode modified with CoFeOx and CoFePB, using a UV LED with a 385 nm peak wavelength.

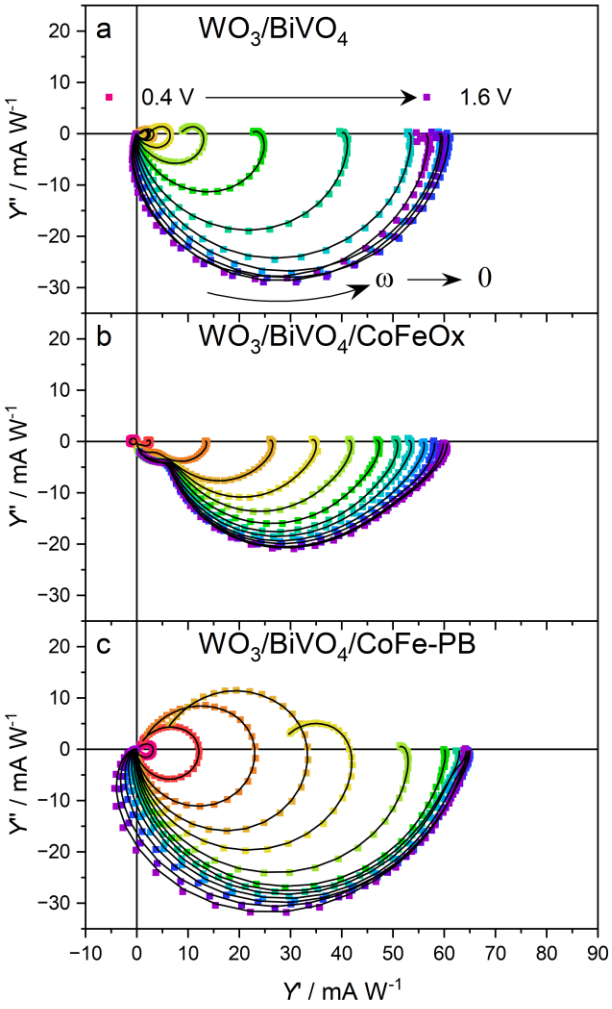

Figure 6.6: *IMPS spectra of a) $WO_3/BiVO_4$, b) $WO_3/BiVO_4$/CoFeOx and c) $WO_3/BiVO_4$/CoFe-PB in borate buffer 0.5M (pH=9) under 385 nm illumination.*

Figure 6.6a show the IMPS spectra measured on $WO_3/BiVO_4$ while applying potentials from 0.4 to 1.6 V_{RHE}. The addition of the catalyst overlayer does not affect the EQE value at high applied potentials, as previously discussed, but largely affects the IMPS spectra in the low-potential region. Indeed, the CSE is largely enhanced by the addition of both CoFeOx and CoFe-PB in the 0.4 – 0.9 V

region, where the maximum photocurrent enhancement is observed due to the onset cathodic shift. This is further highlighted by the CSE versus applied potential plot in Figure 6.7.

However, within this potential region, striking differences in the recombination pathway are observed between the two co-catalysts. CoFeOx deposition is suppressing recombination in the whole considered potential range, including the aforementioned region. On the other hand, the CoFe-PB modified photoanode displays much larger recombination processes described by the semicircle in the 1st quadrant, compared to the other two studied samples. However, as the CSE is also larger, the resulting EQE is almost matching the one of the CoFeOx modified photoanode. These measurements show that both catalysts can enhance the PEC efficiency of the photoanode, but they rely on two different kinetics of the photogenerated charges, especially at low modulation frequencies.

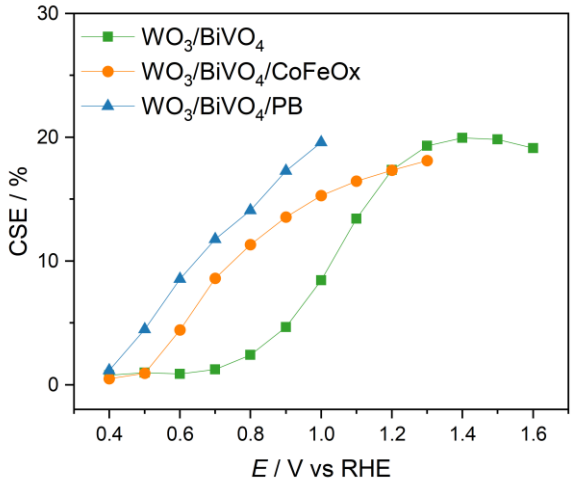

Figure 6.7: *CSE for indicated photoanodes extracted from the measurements in Figure 6.6*

The performance at the plateau of the CoFeOx modified photoanode (Figure 6.6b) is comparable, but there is almost no recombination in all the considered potential range, especially at more negative applied potentials. Two semicircles appear in the 4th quadrant, which could be linked to different parallel paths of photocurrent generation at the semiconductor and at the catalyst.

The different processes that build up the IMPS spectrum can be deconvoluted with Lasso-DRT algorithm described in Section 3.3.[31] The black lines superimposed to the spectra in Figure 6.6 are the fits obtained, and they describe well all the measured data points for the three samples. The results

of this Gaussian Lasso DRT (GL-DRT) fit are more easily visualized through color maps, shown in Figure 6.8, where one can see the characteristic time constants of the processes at different applied potentials and the color scale reports on the intensity of the process. The red color is associated to a process where a current of positive sign (holes that go from the electrode to the solution) is generated, while a blue line is a current of opposite sign, so it can be interpreted as a recombination current or holes going in the opposite direction.

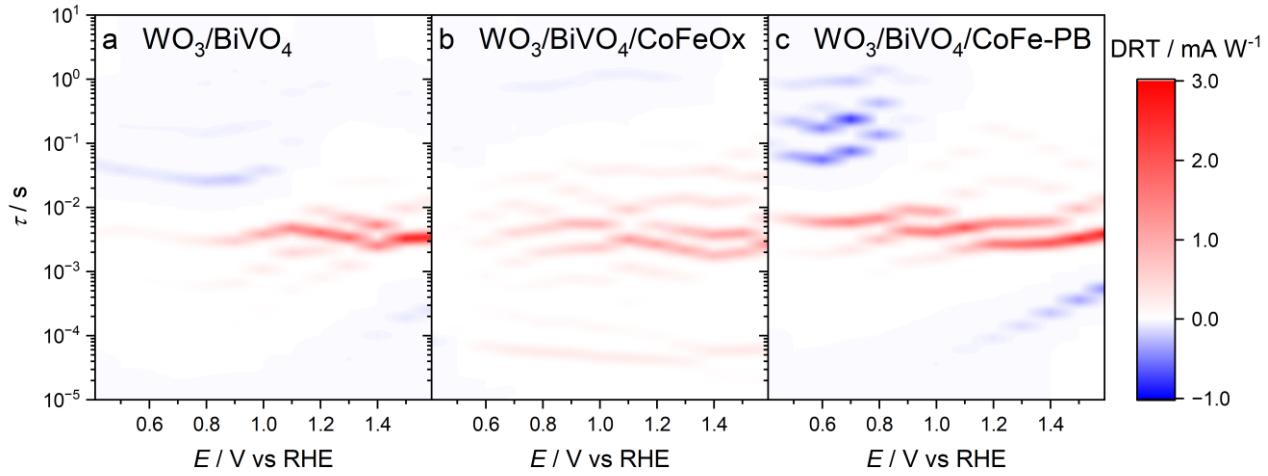

Figure 6.8: *GL-DRT color maps of a) $WO_3/BiVO_4$, b) $WO_3/BiVO_4$/CoFeOx and c) $WO_3/BiVO_4$/CoFe-PB extracted from Figure 6.6.*

The color map in Figure 6.8a describes the kinetics of the bare photoanode: the hole photocurrent is generated in the ms timescale and gets more intense for potentials more positive than 1 V_{RHE}. The recombination processes happen on a longer time scale, with $\tau = (k^{trans} + k^{rec})^{-1} \approx 50$ ms (Figure 6.8a and 6.9a) and gradually decrease in intensity with the applied potential. Such lifetime is consistent with the KWW lifetime extracted from TAS analysis (Figure 6.4g), further confirming the latter to be related to surface-accumulated photoholes.

Larger characteristic times $(k^{trans} + k^{rec})^{-1}$ are seen in both the CoFeOx and the CoFe-PB modified photoanode, shown in Figure 6.8b-c and 6.9a, and are on average ≈ 1 s and ≈ 0.2 s, respectively, again consistent to the corresponding TAS lifetimes. However, the CoFe-PB modified photoanode displays a distribution of characteristic times, suggesting multiple transfer pathways and pointing out that CoFe-PB addition may result in partial passivation of the recombination centers, explaining both the

intermediate photoholes lifetime and the persistence of a recombination pathway in presence of limited band banding (at low applied bias).

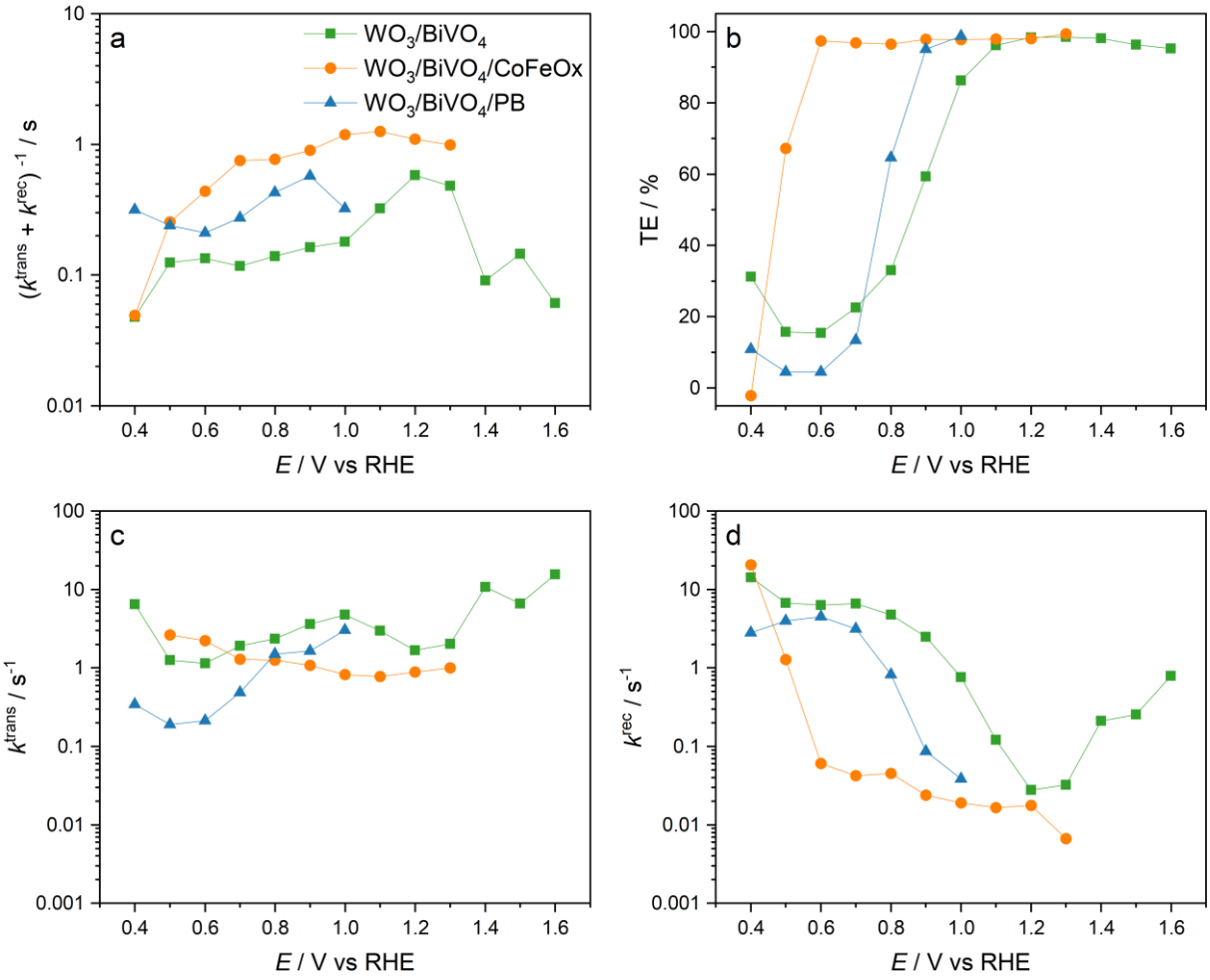

Figure 6.9: *a) characteristic time τ, b) TE, c) k^{trans}, and d) k^{rec} extracted from GL-DRT analysis for the indicated samples.*

Surface recombination and transfer rates (k^{rec} and k^{trans}, respectively), as well as the resulting transfer efficiency (TE), defined as $\frac{k^{trans}}{k^{trans}+k^{rec}}$, can also be extracted from the GL-DRT fit and they are shown as a function of the applied potentials for the three photoanodes in Figure 6.9. We can define two potential regions, namely a low (< 0.8 V_{RHE}) and a high (> 0.8 V_{RHE}), where the two catalysts act on the charge carrier dynamics. At high polarization regimes, the transfer rate is substantially stable with the applied potential for all samples, while only a small drop is observed in the low polarization regime for the $WO_3/BiVO_4$/CoFe-PB sample. On the other hand, the recombination rates are largely

modified by the addition of the catalysts. The CoFeOx overlayer is producing a drop of two orders of magnitude in the low polarization regime, resulting in a large enhancement of the transfer efficiency, while for the Prussian Blue analogue, the enhancement can be appreciated only at potentials larger than 0.8 V. Thus, the onset of the transfer efficiency enhancement is only shifted to more cathodic potentials of about 100 mV, compared to the 400 mV shift produced by CoFeOx.

To sum up, at high polarization regimes, the addition of both Co-Fe mixed co-catalysts reduces the recombination rate, enhancing both charge separation efficiency and photoholes lifetime, suggesting efficient passivation of recombination centers. The same behavior is observed in the low polarization regime, in presence of the CoFeOx overlayer, pointing out full passivation also in absence of large bending of the semiconductor bands. As the transfer rate is essentially consistent between this sample and pristine $WO_3/BiVO_4$, the rate limiting step for water oxidation is then expected to be either the direct transfer of photoholes from $BiVO_4$ valence band, or the transfer to the co-catalyst layer, followed by an extremely fast hole transfer to the electrolyte. On the other hand, the CoFe-PB overlayer is producing both enhanced photoholes lifetime and CSE in the low potential regime, as well as a transfer rate similar to CoFeOx, suggesting efficient charge generation and extraction. However, in absence of large band bending in the semiconductor layer, the photogenerated holes are more prone to recombine at the surface, suggesting only partial passivation of the recombination centers.

7 Dynamics of photoexcited charge carriers in CIGS-based photocathodes compared to solar cells: insights from intensity modulated photocurrent spectroscopy

In this Chapter, we investigate the performance and the charge carrier dynamics of different solar energy conversion pathways that employ a $Cu(In,Ga)Se_2$ (CIGS) thin film as the light absorber. Specifically, we compare a) CIGS solar cell (CIGS PV), b) photoelectrochemical cell for water splitting using a CIGS photocathode (CIGS PEC), c) same as b) with the addition of a NiMo catalyst layer on the CIGS photocathode (CIGS-NiMo PEC), and d) dark electrolysis with a NiMo cathode sputtered on FTO assisted by a CIGS solar cell (CIGS PV-NiMo EC). Linear sweep voltammetry (LSV) and intensity modulated photocurrent spectroscopy (IMPS) techniques are employed to investigate the photocurrent response and charge carrier dynamics of each configuration. The characteristic timescales of the investigated dynamics are determined by means of the Lasso regression analysis of the distribution of relaxation times (DRT).[21]

7.1 Characterization of a CIGS photovoltaic cell

In Figure 7.1, the current-voltage (*j*-*V*) characteristics of the CIGS solar cell under 1 sun illumination is presented. The *j*-*V* curve provides valuable insights into the device's performance and allows for the calculation of important parameters such as the point of maximum power (P_{max}), fill factor (FF), and efficiency.

The voltage range used for the sweep covered the entire operating range of the device, allowing for the determination of the open-circuit voltage (V_{oc} = 0.705 V) and of the short-circuit current (j_{sc} = 32.2 mA cm^{-2}).

From the *j-V* curve, the point of maximum power is determined at 0.524 V, which corresponds to the maximum power output of the solar cell (P_{max} = 14.8 mW cm^{-2}). The FF is thus calculated to be 65.4%. The efficiency of the solar cell, calculated as the ratio of the maximum power output to the incident power from the solar simulator is 14.8%, comparable to the one of commercial CIGS solar cells.[190–192]

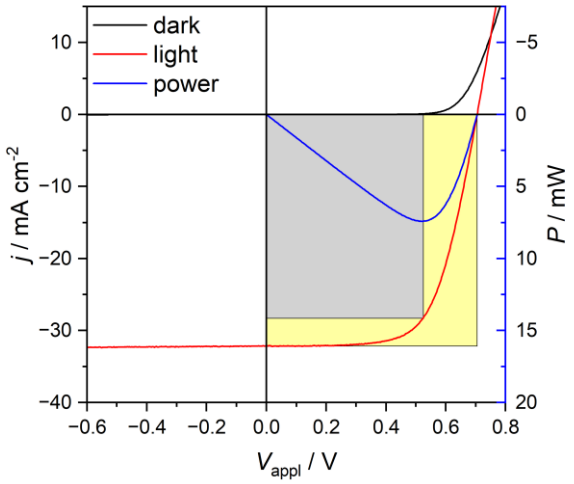

Figure 7.1 *Current-voltage characteristics of a CIGS solar cell in dark and under AM1.5G illumination, and output power.*

7.2 PEC characterization of CIGS-based photocathodes

In Figure 7.2, we present a comparison of the chopped linear sweep voltammetry (LSV) curves measured in borate buffer (0.1 M) with Na_2SO_4 (0.5 M) at pH 9 for the CIGS-only photocathodes and the CIGS-NiMo photocathodes. LSV curves are commonly characterized by spikes in photocurrent during potential sweeping when the light is turned on, followed by a subsequent decrease in current due to charge recombination, typically occurring at the surface of the material.

The CIGS-NiMo photocathode exhibits similar spike heights in photocurrent compared to the CIGS photocathode. However, a significantly reduced recombination is observed in the CIGS-NiMo photocathode, resulting in a sustained photocurrent of 5 mA cm^{-2} at 0 V_{RHE}. This enhanced photocurrent indicates either improved charge transfer to the solution or reduced charge recombination within the CIGS-NiMo photocathode, which contributes to its better performance.

Another significant effect observed in the LSV curves is the anodic shift in the onset potential of the dark current, which can be attributed to the incorporation of NiMo. In the case of the CIGS-only photocathode, the dark current remains at zero across the entire potential range. In contrast, the introduction of NiMo in the CIGS-NiMo photocathode results in the appearance of dark current around 0 V_{RHE}, reaching up to 2 mA cm^{-2} at −0.3 V_{RHE}. Notably, at this potential, the photocurrent reaches an impressive value of almost 10 mA cm^{-2}, further highlighting the exceptional performance of the CIGS-NiMo photocathode even when compared to existing literature benchmarks, based on Pt-modified CIGS photocathodes.[193,194]

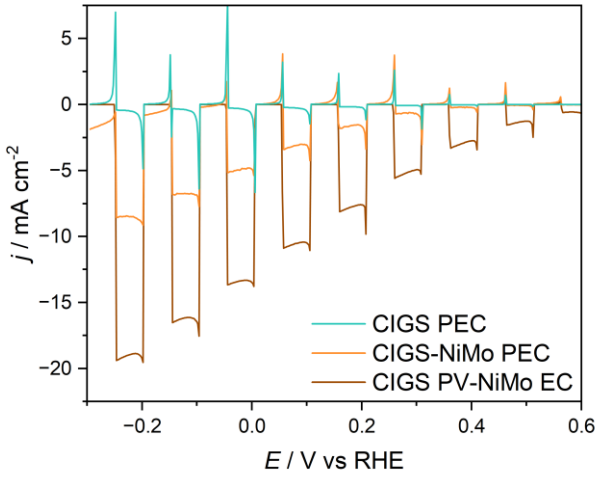

Figure 7.2 *Linear sweep voltammetry under chopped AM 1.5G illumination (100 mW cm^{-2}) of the different CIGS-based devices architectures used for water splitting in a PEC cell in a three-electrode configuration (Pt as counter electrode, Ag/AgCl as reference electrode) in borate buffer 0.1M + Na_2SO_4 0.5M (pH = 9)*

When comparing the photocurrent generated by the CIGS solar cell (Figure 7.1) and the LSV measurements on the CIGS and CIGS-NiMo photocathodes, a significant drop in efficiency is observed when the CIGS material is incorporated into a PEC cell for hydrogen evolution. The short-circuit current of the PV cell (32.2 mA cm^{-2}) far exceeds the photocurrent generated by the CIGS-NiMo photocathode (10 mA cm^{-2}). A potential hypothesis for this efficiency loss is the presence of additional layers, such as TiO2 and NiMo, in the photocathode configuration, which may introduce defects at the interfaces and either increase recombination or limit charge transfer between layers until the electrons reach the electrolyte.

To investigate this hypothesis, an assisted PEC device was constructed, where NiMo was sputtered onto a fluorine-doped tin oxide (FTO) substrate and used as dark cathode inside the PEC cell. This electrode was connected in series with the metallic pad of the CIGS solar cell. The solar cell, operating in air, had its back contact connected to the working electrode of the electrochemical workstation.

This experimental setup allowed for a comparison of the conversion efficiency of the CIGS material when used as a photocathode behind the NiMo layer to its efficiency as a standalone solar cell in air. By effectively removing the potential recombination centers introduced by the TiO2 layer, this configuration aimed to provide insights into the performance differences observed.

The LSV measurements, as shown in Figure 7.2, demonstrate an increase in photocurrent density in all the investigated potential range. Although the current density still falls short of the short-circuit current of the standalone solar cell, 20 mA cm^{-2} of photocurrent are generated at −0.3 V_{RHE}.

These experiments confirm that using assisted devices with the absorber material in air instead of in solution yields significantly improved performance compared to using photocathodes. Additionally, NiMo proves to be a valuable alternative to more expensive and rare catalysts based on Pt, Ir or Ru.

Through IMPS measurements, generation and separation of charges inside the CIGS material and the charge transfer and recombination processes at the electrode/electrolyte interface were investigated, in order to gain deeper insights into the carrier dynamics within the PV and PEC architectures described in the previous measurements.

Figure 3a shows the intensity modulated photocurrent spectroscopy (IMPS) spectra for the CIGS solar cell as a function of the applied potential, ranging from 0.7 V (close to open circuit) to 0 V (short circuit). Interestingly, no recombination is observed for any of the applied potentials. The generation semicircle in the second quadrant steadily increases in size until it reaches a plateau value of 150 mA W^{-1} at potentials close to 0 V. This indicates efficient charge generation and separation processes within the CIGS absorber layer, with minimal losses due to recombination.

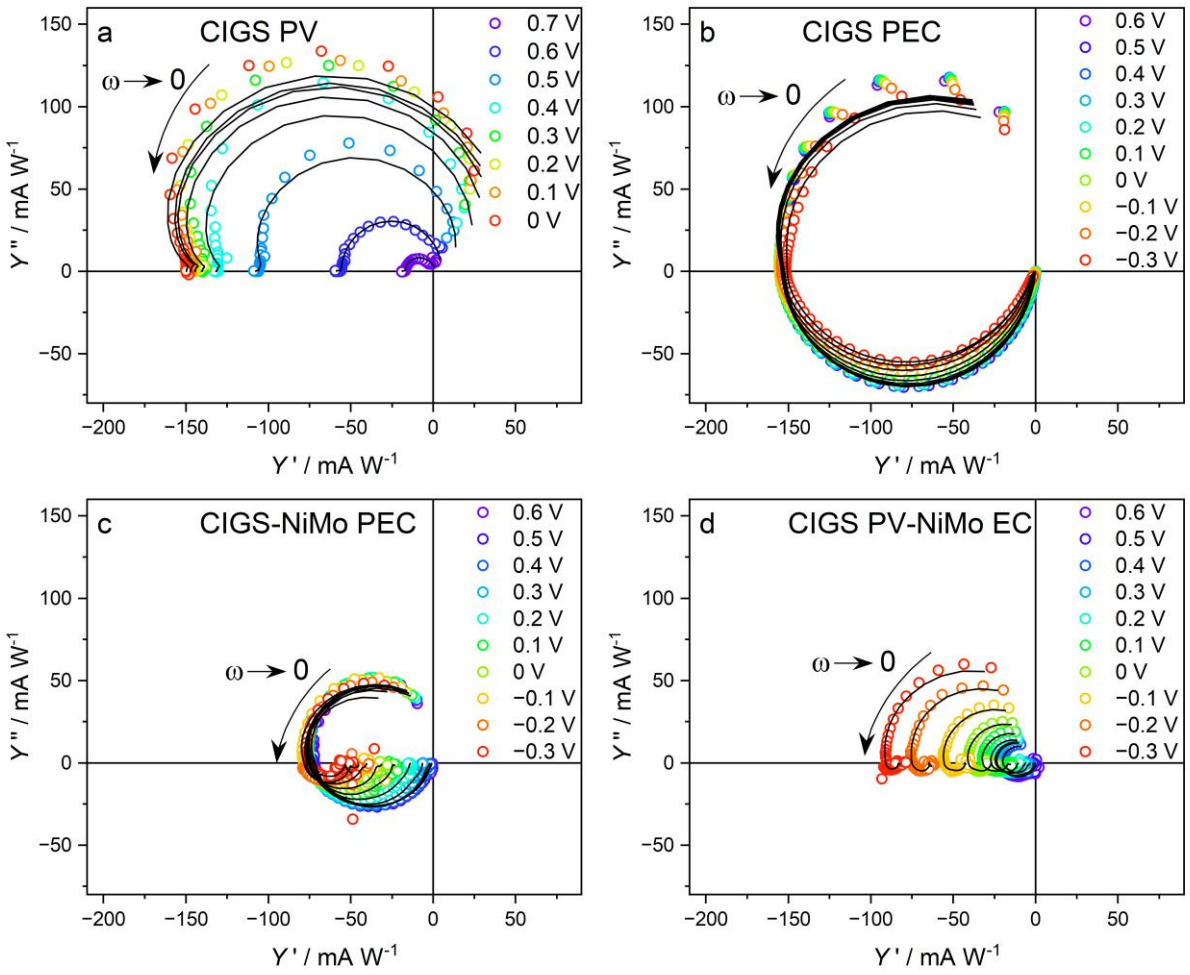

Figure 7.3: *IMPS measurements collected with 100 mW cm^{-2} white light bias and 8 mW cm^{-2} red light bias (660 nm) with 10% of light modulation at the indicated applied potentials performed on a) CIGS PV, b) CIGS PEC, c) CIGS-NiMo PEC, and d) CIGS PV-NiMo EC. Measurements on a) were performed in air in a two-electrode configuration, while on b), c), and d) were performed in a PEC cell in a standard three-electrode configuration where a solution of borate buffer 0.1M + Na_2SO_4 0.5 M (pH = 9) was fluxed continuously during data collection, with Pt as counter electrode and Ag/AgCl as reference electrode*

At high frequencies, an additional feature appears in the IMPS spectra, crossing the imaginary axis and resulting in negative admittance. This phenomenon may arise when the absorption length in the material is much shorter than the cell thickness, and the diffusion length of carriers is longer than the absorption length. When strongly absorbed light illuminates the semiconductor from the electrolyte side, a characteristic "time of flight" delay in the photocurrent response is observed. In the IMPS plot, this delay manifests as a spiral approach to the origin at high frequencies. The phase shift continuously

increases with increasing frequency and arises from the constant time delay between charge generation and collection, determined by the diffusional transit time.[195,196]

In Figure 7.3b, representing the IMPS spectra of the CIGS photocathode, we do not observe changes in the generation semicircle as a function of the applied potential, unlike the CIGS solar cell. Also, the photocathode exhibits recombination processes, as indicated by the presence of an additional semicircle in the third quadrant, that loops back to the axes origin, indicating a zero EQE. This suggests that the introduction of the TiO_2 layer and the formation of the semiconductor/electrolyte interface impacts the carrier dynamics, leading to increased recombination losses.

Figure 7.3c displays the IMPS spectra of the CIGS-NiMo photocathode. We observe a slight decrease in the size of the generation semicircle at high frequency compared to the CIGS-only photocathode, but the additional semicircle in the third quadrant is less pronounced, indicating that the incorporation of NiMo as a catalyst enhances the charge carrier dynamics within the CIGS-NiMo photocathode.

Finally, Figure 7.3d shows the IMPS spectra for the NiMo dark cathode assisted by the CIGS solar cell. Remarkably, this configuration exhibits enhanced carrier dynamics, leading to a generation semicircle whose size is potential dependent and comparable to the CIGS solar cell and the CIGS photocathode, but has significantly reduced recombination as seen in the CIGS-NiMo architecture of Figure 7.3c. This confirms that the direct connection of the solar cell to NiMo in an assisted PEC configuration improves charge transfer efficiency and minimizes recombination losses, yielding higher photocurrents.

7.3 GL-DRT anlaysis

The color maps shown in Figure 4 are the result of the GL-DRT analysis, that are used to emphasize the dependency of relaxation times on the potential applied to the PEC cell. All the different architectures display a characteristic feature around 3 to 8 microseconds, related to the rapid charge generation and separation processes occurring within the CIGS absorber layer.

The negative sign of this feature in the color maps is consistent with the direction of the electron flow, which goes from the CIGS absorber layer to the surface, then to the solution and is collected at the counter electrode. This negative photocurrent response indicates the efficient extraction of photogenerated electrons from the CIGS absorber layer and their subsequent transport through the various layers (CdS, ZnO, AZO, TiO_2, NiMo, etc.) to reach the electrode/electrolyte interface.

As this negative feature appears across all architectures and configurations, it becomes evident that the initial charge generation and separation within the CIGS absorber layer itself occur with similar characteristic timescales, regardless of the specific architecture or catalyst used. This common feature highlights the robustness of the CIGS absorber layer as a photocathode material and its capability to efficiently generate and separate charge carriers in response to incident light.

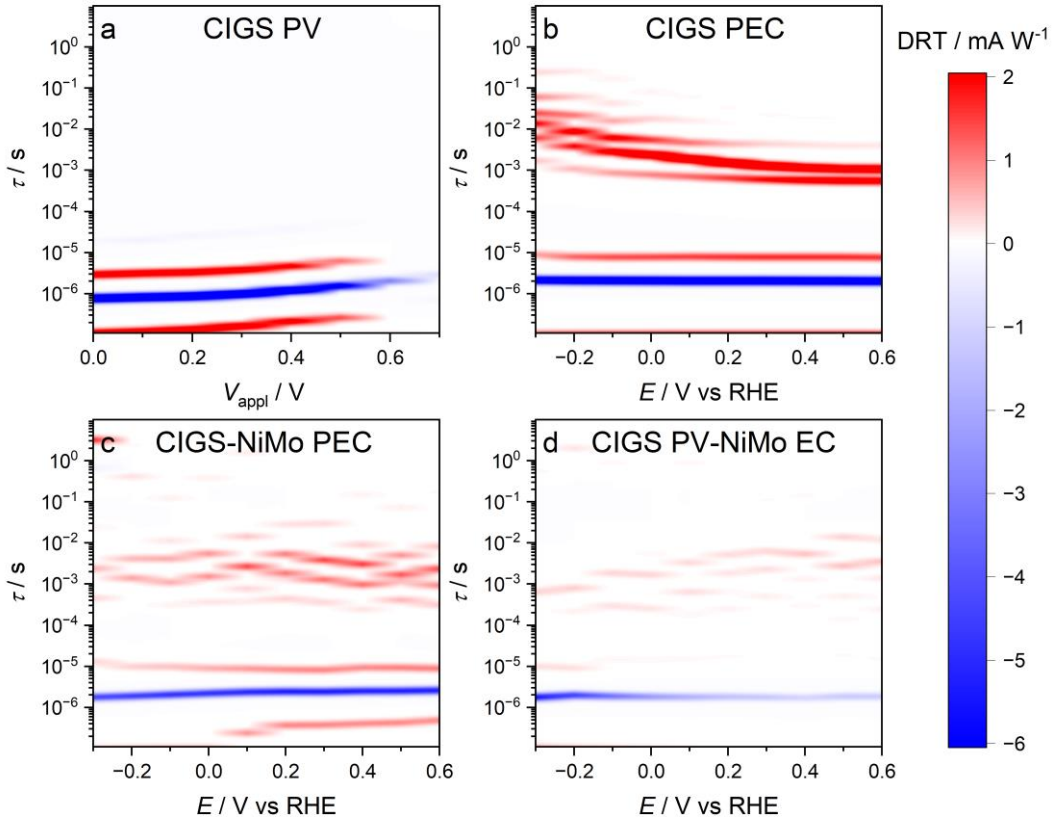

Figure 7.4: *GL-DRT color maps on a) CIGS PV, b) CIGS PEC, c) CIGS-NiMo PEC, and d) CIGS PV-NiMo EC extracted from measurements in Figure 7.3*

Starting with the CIGS solar cell in Figure 7.4a, two additional red traces are observed. The first one, occurring on faster timescales, is related to the high-frequency feature in the IMPS spectra that was

commented earlier. The second red trace, around 10-20 microseconds, indicates a fast recombination phenomenon, likely occurring at the CIGS/CdS or CdS/AZO interfaces. The GL-DRT algorithm successfully identifies and separates these recombination features, even though their characteristic times are all very close. Moving to Figure 7.4b, which depicts the color map of the CIGS photocathode, similar positive (red) features are observed below microseconds and around 10 microseconds, suggesting that the CIGS/CdS/ZnO/AZO architecture operates similarly. We can exclude that the second recombination feature is due to surface recombination, as it is expected to occur at longer times and it was observed also for the CIGS solar cell operating in air. Interestingly, all the charge carriers generated at the p-n junction and rapidly extracted from the AZO layer recombine on a longer timescale, in the range of milliseconds. This indicates poor carrier dynamics at either the TiO_2/AZO interface or at the semiconductor/electrolyte interface. Upon the addition of NiMo to the CIGS photocathode in Figure 7.4c, the recombination feature at ≈ 10 μs disappears, indicating very rapid electron extraction from the CdS layer. NiMo also reduces surface recombination on the longer timescale, in particular it removes all the processes happening at times longer than 10 ms. In Figure 7.4d, representing the CIGS solar cell connected to the NiMo dark cathode, the two fast recombination features are again present, similar to the CIGS solar cell. However, the second feature is significantly lower and nearly disappears at the most negative applied potentials. Moreover, long-time recombination is greatly reduced, nearly reaching zero at −0.3 V_{RHE}. This configuration demonstrates the best possible kinetics at the CIGS/CdS p-n junction and excellent surface kinetics at the NiMo/electrolyte interface.

Figure 7.5 shows CSE, TE, k^{trans}, and k^{rec} as a function of the applied potential for the architectures CIGS PEC, CIGS-NiMo PEC, and CIGS PV-NiMo EC. From this analysis one can appreciate the beneficial effect of the NiMo catalyst on the CIGS photocathode or of the CIGS PV module assisting the NiMo dark cathode in solution. In fact, even though the CIGS photocathode exhibits the highest CSE that reaches values of almost 30% in all the considered potential range, its PEC performance is

severely limited by the TE of electrons in solution which is never higher than 0.5%. The NiMo-modified photocathode has a lower CSE, which is potential independent and oscillates around 13-14%, but the TE has the typical sigmoidal shape, reaching a value of 70% at – 0.3 V_{RHE}. Even higher TE values, up to ≈ 91%, are reached by the NiMo dark cathode assisted by the CIGS PV module. In this case, the performance is limited more by the CSE, as it stays around 5% until 0 V_{RHE} and only at more cathodic applied potential it arrives at ≈ 15%.

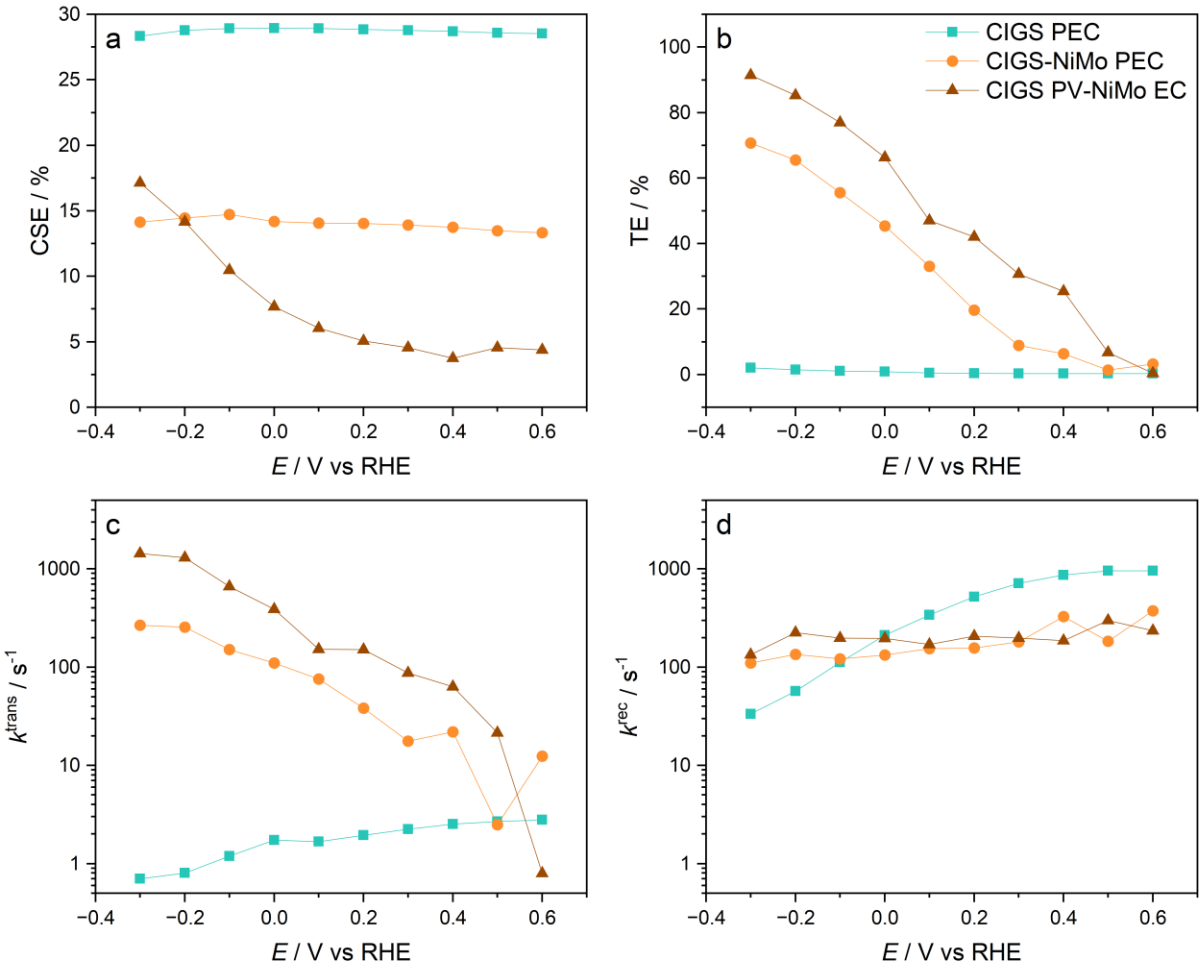

Figure 7.5: *a) CSE, b) TE, c) k^{trans}, and d) k^{rec} extracted from the GL-DRT analysis shown in Figure 7.4 for the indicated samples.*

The transfer and recombination rates of the three architectures are shown in Figure 7.5c-d. In all the considered potential range k^{trans} of the CIGS photocathode is always significantly lower than k^{rec}. When NiMo is deposited on the surface, k^{trans} increases for all potentials, and at the most cathodic potential the enhancement is more than two orders of magnitude. The same effect is seen with the

assisted NiMo dark cathode, where k^{trans} increases of one more order of magnitude. The other effect of using NiMo on the photocathode or as a dark cathode is a slight drop in k^{rec} compared to the unmodified CIGS photocathode, especially when the device operates at more anodic potentials. In these two architectures k^{trans} becomes greater than k^{rec} at 0 V_{RHE} and 0.2 V_{RHE}, respectively.

The results obtained from this GL-DRT analysis show a substantial difference between NiMo used on photocathodes for HER and Co-Fe mixed overlayers used on photoanodes for OER. In fact, here not only the recombination is suppressed, but the transfer of charges in solution is increased, meaning that NiMo can be considered as a catalyst for hydrogen evolution in the strict sense.

There is a very limited understanding of CIGS coupled with a NiMo catalyst used as a photocathode and the focus of the few works present in literature is on how to increase the stability depending on the pH of the solution and the applied potential.[54] The novel GL-DRT analysis on different PEC and PV-E architectures allowed a more deep and thorough understanding of the severe limitations that the CIGS absorber encounters when used as photocathode. In fact, while the kinetics of the absorber layer is the same in all configurations, extractions of electrons from the TiO_2 protective layer to the solution is the limiting step for the HER. The results presented in this chapter are encouraging for using NiMo as a HER catalyst alternatively to platinum to improve the efficiency of CIGS photocathodes: in fact, the active sites of NiMo enhance the transfer rate in solution and decrease the recombination at low cathodic potentials, reaching almost 10 mA cm^{-2} at – 0.3 V_{RHE}. The performance of this system still falls short of the assisted water splitting configuration, which presents impressive transfer efficiency and transfer rate of electrons in solution, but opens the possibility of further studies on modified photocathodes for PEC water splitting.

Conclusions

In this thesis, the fundamental processes that affect the kinetics of charge carriers in photoelectrodes used for PEC water splitting were explored by means of time- and frequency-resolved techniques. In the first part, multi-electron transfer at H-terminated p-Si acetonitrile electrolyte interfaces revealed that the largest photovoltages are realized when the reduction potential of the species in solution has the same energy level as the continuum of conduction band electron. This behavior is due to the formation an inversion layer at the surface that supports multi-electron transfer, as highlighted by steady-state and time-resolved infrared spectroscopic techniques. The bell-shaped recombination kinetic data also indicated that all four of the semiconductor electric field conditions known for solid-state semiconductor junctions (accumulation, flatband, depletion, and inversion) can also be accessed in photoelectrochemical cells.

In the second part, wavelength-dependent IMPS was used to investigate the optoelectronic properties of a mesoporous $WO_3/BiVO_4$ photoanode in an *operando* PEC cell. The selective excitation of the different layers of the heterojunction allowed for a deep understanding of the loss mechanisms affecting charge extraction and it highlighted the occurrence of recombination processes at the heterostructure interface.

The third part showed a combined transient absorption spectroscopy and IMPS study spanning twelve orders of magnitude in time on the effect of Co-Fe overlayers on the kinetics of a $WO_3/BiVO_4$ heterojunction. A suppression of the recombination of holes trapped at the surface was observed at all time scales, resulting in a larger accumulation of holes available for water oxidation. In the µs timescale a hole transfer from intra bandgap traps at the surface to oxidized cations in the overlayer was observed. Increased transfer efficiency was observed in the ms – s range, resulting from decreased surface recombination rate, rather than increased hole transfer to the solution.

Finally, a beneficial effect of a NiMo layer on the surface of a CIGS photocathode to drive the HER was observed, establishing this binary alloy as a valid alternative to rare-metal-based electrocatalysts. Different PV, PV-E and PEC architectures based on a CIGS absorber layer were characterized by means of IMPS in air or in electrochemical environment, allowing a robust comparison of the fundamental charge carrier kinetics in the bulk and at the surface, where charges are extracted to drive the HER.

Bibliography

1. Ghoniem, A.F. (2011) Needs, resources and climate change: Clean and efficient conversion technologies. *Prog. Energy Combust. Sci.*, **37** (1), 15–51.

2. Lewis, N.S., and Nocera, D.G. (2006) Powering the planet: Chemical challenges in solar energy utilization. *Proc. Natl. Acad. Sci. U. S. A.*, **103** (43), 15729–15735.

3. Polman, A., and Atwater, H.A. (2012) Photonic design principles for ultrahigh-efficiency photovoltaics. *Nat. Mater.*, **11** (3).

4. Chau, K., Djire, A., and Khan, F. (2022) Review and analysis of the hydrogen production technologies from a safety perspective. *Int. J. Hydrogen Energy*, **47** (29), 13990–14007.

5. Fujishima, A., and Honda, K. (1972) Electrochemical Photolysis of Water at a Semiconductor Electrode. *Nat. 1972 2385358*, **238** (5358), 37–38.

6. Goto, Y., Hisatomi, T., Wang, Q., Higashi, T., Ishikiriyama, K., Maeda, T., Sakata, Y., Okunaka, S., Tokudome, H., Katayama, M., Akiyama, S., Nishiyama, H., Inoue, Y., Takewaki, T., Setoyama, T., Minegishi, T., Takata, T., Yamada, T., and Domen, K. (2018) A Particulate Photocatalyst Water-Splitting Panel for Large-Scale Solar Hydrogen Generation. *Joule*, **2** (3), 509–520.

7. Guan, X., Alam Chowdhury, F., Pant, N., Guo, L., Vayssieres, L., and Mi, Z. (2018) Efficient Unassisted Overall Photocatalytic Seawater Splitting on GaN-Based Nanowire Arrays. *J. Phys. Chem. C*, **122** (25), 13797–13802.

8. Hisatomi, T., and Domen, K. (2019) Reaction systems for solar hydrogen production via water splitting with particulate semiconductor photocatalysts. *Nat. Catal. 2019 25*, **2** (5), 387–399.

9. Jia, J., Seitz, L.C., Benck, J.D., Huo, Y., Chen, Y., Ng, J.W.D., Bilir, T., Harris, J.S., and Jaramillo, T.F. (2016) Solar water splitting by photovoltaic-electrolysis with a solar-to-hydrogen efficiency over 30%. *Nat. Commun.*, **7**, 13237.

10. Hu, S., Xiang, C., Haussener, S., Berger, A.D., and Lewis, N.S. (2013) An analysis of the optimal band gaps of light absorbers in integrated tandem photoelectrochemical water-splitting systems. *Energy Environ. Sci.*, **6** (10), 2984–2993.

11. Zhang, S., Shen, L., Ye, T., Kong, K., Ye, H., Ding, H., Hu, Y., and Hua, J. (2020) Noble-Metal-Free Perovskite-BiVO4 Tandem Device with Simple Preparation Method for Unassisted Solar Water Splitting. *Energy and Fuels*, **34** (4), 5016–5023.

12. Döscher, H., Geisz, J.F., Deutsch, T.G., and Turner, J.A. (2014) Sunlight absorption in water-efficiency and design implications for photoelectrochemical devices. *Energy Environ. Sci.*, **7** (9), 2951–2956.

13. Hu, C., Zhang, L., and Gong, J. (2019) Recent progress made in the mechanism comprehension and design of electrocatalysts for alkaline water splitting. *Energy Environ. Sci.*, **12** (9), 2620–2645.

14. Li, W., Tian, H., Ma, L., Wang, Y., Liu, X., and Gao, X. (2022) Low-temperature water electrolysis: fundamentals, progress, and new strategies. *Mater. Adv.*, **3** (14), 5598–5644.

15. Koper, M.T.M. (2011) Thermodynamic theory of multi-electron transfer reactions:

Implications for electrocatalysis. *J. Electroanal. Chem.*, **660** (2), 254–260.

16. Montoya, J.H., Seitz, L.C., Chakthranont, P., Vojvodic, A., Jaramillo, T.F., and Nørskov, J.K. (2016) Materials for solar fuels and chemicals. *Nat. Mater.*, **16**, 70–81.

17. Shockley, W., and Queisser, H.J. (1961) Detailed Balance Limit of Efficiency of p-n Junction Solar Cells. *J. Appl. Phys.*, **32** (3), 510–519.

18. De Vos, A. (1980) Detailed balance limit of the efficiency of tandem solar cells. *J. Phys. D. Appl. Phys.*, **13**, 839–846.

19. Fountaine, K.T., Lewerenz, H.J., and Atwater, H.A. (2016) Efficiency limits for photoelectrochemical water-splitting. *Nat. Commun.*, **7**, 13706.

20. Eperon, G.E., Leijtens, T., Bush, K.A., Prasanna, R., Green, T., Wang, J.T.W., McMeekin, D.P., Volonakis, G., Milot, R.L., May, R., Palmstrom, A., Slotcavage, D.J., Belisle, R.A., Patel, J.B., Parrott, E.S., Sutton, R.J., Ma, W., Moghadam, F., Conings, B., Babayigit, A., Boyen, H.G., Bent, S., Giustino, F., Herz, L.M., Johnston, M.B., McGehee, M.D., and Snaith, H.J. (2016) Perovskite-perovskite tandem photovoltaics with optimized band gaps. *Science (80-.).*, **354** (6314), 861–865.

21. Piccioni, A., Vecchi, P., Vecchi, L., Grandi, S., Caramori, S., Mazzaro, R., and Pasquini, L. (2023) Distribution of Relaxation Times Based on Lasso Regression: A Tool for High-Resolution Analysis of IMPS Data in Photoelectrochemical Systems. *J. Phys. Chem. C*, **127** (17), 7957–7964.

22. Keller, N.D., Vecchi, P., Grills, D.C., Polyansky, D.E., Bein, G.P., Dempsey, J.L., Cahoon, J.F., Parsons, G.N., Sampaio, R.N., and Meyer, G.J. (2023) Multi-Electron Transfer at H-Terminated p-Si Electrolyte Interfaces: Large Photovoltages under Inversion Conditions. *J. Am. Chem. Soc.*, **145** (20), 11282–11292.

23. Vecchi, P., Piccioni, A., Mazzaro, R., Mazzanti, M., Cristino, V., Caramori, S., and Pasquini, L. (2022) Charge Separation Efficiency in WO_3 /$BiVO_4$ Photoanodes with CoFe Prussian Blue Catalyst Studied by Wavelength-Dependent Intensity-Modulated Photocurrent Spectroscopy. *Sol. RRL*, 2200108.

24. Lee, D.K., Lee, D., Lumley, M.A., and Choi, K.S. (2019) Progress on ternary oxide-based photoanodes for use in photoelectrochemical cells for solar water splitting. *Chem. Soc. Rev.*, **48** (7), 2126–2157.

25. Jang, Y.J., and Lee, J.S. (2019) Photoelectrochemical Water Splitting with p-Type Metal Oxide Semiconductor Photocathodes. *ChemSusChem*, **12** (9), 1835–1845.

26. Dhar, S., Seitz, O., Halls, M.D., Choi, S., Chabal, Y.J., and Feldman, L.C. (2009) Chemical properties of oxidized silicon carbide surfaces upon etching in hydrofluoric acid. *J. Am. Chem. Soc.*, **131** (46), 16808–16813.

27. Yablonovitch, E., Allara, D.L., Chang, C.C., Gmitter, T., and Bright, T.B. (1986) Unusually Low Surface-Recombination Velocity on Silicon and Germanium Surfaces. *Phys. Rev. Lett.*, **57** (2), 249–252.

28. Higashi, G.S., Chabal, Y.J., Trucks, G.W., and Raghavachari, K. (1990) Ideal hydrogen termination of the Si (111) surface. *Appl. Phys. Lett.*, **56** (7), 656–658.

29. Dumas, P., Chabal, Y.J., and Jakob, P. (1992) Morphology of hydrogen-terminated Si(111) and Si(100) surfaces upon etching in HF and buffered-HF solutions. *Surf. Sci.*, **269–270** (C), 867–878.

30. Gibbons, J.F., Cogan, G.W., Gronet, C.M., and Lewis, N.S. (1984) A 14% efficient nonaqueous semiconductor/liquid junction solar cell. *Appl. Phys. Lett.*, **45** (10), 1095–1097.

31. Lieber, C.M., Gronet, C.M., and Lewis, N.S. (1984) Evidence against surface state limitations on efficiency of p-Si/CH3CN junctions. *Nature*, **307**, 533–534.

32. Di Valentin, C., and Pacchioni, G. (2014) Spectroscopic properties of doped and defective semiconducting oxides from hybrid density functional calculations. *Acc. Chem. Res.*, **47** (11), 3233–3241.

33. Mi, Q., Zhanaidarova, A., Brunschwig, B.S., Gray, H.B., and Lewis, N.S. (2012) A quantitative assessment of the competition between water and anion oxidation at WO 3 photoanodes in acidic aqueous electrolytes. *Energy Environ. Sci.*, **5** (2), 5694–5700.

34. Huang, Z.F., Song, J., Pan, L., Zhang, X., Wang, L., and Zou, J.J. (2015) Tungsten oxides for photocatalysis, electrochemistry, and phototherapy. *Adv. Mater.*, **27** (36), 5309–5327.

35. Kudo, A., Omori, K., and Kato, H. (1999) A Novel Aqueous Process for Preparation of Crystal Form-Controlled and Highly Crystalline BiVO4 Powder from Layered Vanadates at Room Temperature and Its Photocatalytic and Photophysical Properties. *J. Am. Chem. Soc.*, **121** (49), 11459–11467.

36. Chatchai, P., Murakami, Y., Kishioka, S.-Y., Nosaka, A.Y., and Nosaka, Y. (2009) Efficient photocatalytic activity of water oxidation over WO 3 /BiVO 4 composite under visible light irradiation. *Electrochim. Acta*, **54**, 1147–1152.

37. Grau, S., Berardi, S., Moya, A., Matheu, R., Cristino, V., Vilatela, J.J., Bignozzi, C.A., Caramori, S., Gimbert-Suriñach, C., and Llobet, A. (2018) A hybrid molecular photoanode for efficient light-induced water oxidation. *Sustain. Energy Fuels*, **2** (9), 1979–1985.

38. Shi, X., Herraiz-Cardona, I., Bertoluzzi, L., Lopez-Varo, P., Bisquert, J., Park, J.H., and Gimenez, S. (2016) Understanding the synergistic effect of WO3–BiVO4 heterostructures by impedance spectroscopy. *Phys. Chem. Chem. Phys.*, **18** (13), 9255–9261.

39. Rao, P.M., Cai, L., Liu, C., Cho, I.S., Lee, C.H., Weisse, J.M., Yang, P., and Zheng, X. (2014) Simultaneously efficient light absorption and charge separation in WO3/BiVO4 core/shell nanowire photoanode for photoelectrochemical water oxidation. *Nano Lett.*, **14** (2), 1099–1105.

40. Grigioni, I., Stamplecoskie, K.G., Selli, E., and Kamat, P. V. (2015) Dynamics of Photogenerated Charge Carriers in WO3/BiVO4 Heterojunction Photoanodes. *J. Phys. Chem. C*, **119** (36), 20792–20800.

41. Grigioni, I., Ganzer, L., V. A. Camargo, F., Bozzini, B., Cerullo, G., and Selli, E. (2019) In Operando Photoelectrochemical Femtosecond Transient Absorption Spectroscopy of WO3/BiVO4 Heterojunctions. *ACS Energy Lett.*, **4** (9), 2213–2219.

42. Grigioni, I., G. Stamplecoskie, K., H. Jara, D., Vittoria Dozzi, M., Oriana, A., Cerullo, G., V. Kamat, P., and Selli, E. (2017) Wavelength-Dependent Ultrafast Charge Carrier Separation in the WO3/BiVO4 Coupled System. *ACS Energy Lett.*, **2** (6), 1362–1367.

43. Shi, X., Choi, I.Y., Zhang, K., Kwon, J., Kim, D.Y., Lee, J.K., Oh, S.H., Kim, J.K., and Park, J.H. (2014) Efficient photoelectrochemical hydrogen production from bismuth vanadate-decorated tungsten trioxide helix nanostructures. *Nat. Commun.*, **5**, 4775.

44. Su, J., Guo, L., Bao, N., and Grimes, C.A. (2011) Nanostructured WO3/BiVO4 heterojunction films for efficient photoelectrochemical water splitting. *Nano Lett.*, **11** (5),

1928–1933.

45. Fujimoto, I., Wang, N., Saito, R., Miseki, Y., Gunji, T., and Sayama, K. (2014) WO3/BiVO4 composite photoelectrode prepared by improved auto-combustion method for highly efficient water splitting. *Int. J. Hydrogen Energy*, **39** (6), 2454–2461.

46. Kalanur, S.S., Yoo, I.H., Park, J., and Seo, H. (2017) Insights into the electronic bands of WO3/BiVO4/TiO2, revealing high solar water splitting efficiency. *J. Mater. Chem. A*, **5** (4), 1455–1461.

47. García-Tecedor, M., Cardenas-Morcoso, D., Fernández-Climent, R., and Giménez, S. (2019) The Role of Underlayers and Overlayers in Thin Film BiVO4 Photoanodes for Solar Water Splitting. *Adv. Mater. Interfaces*, **6** (15).

48. Rudmann, D., Brémaud, D., Da Cunha, A.F., Bilger, G., Strohm, A., Kaelin, M., Zogg, H., and Tiwari, A.N. (2005) Sodium incorporation strategies for CIGS growth at different temperatures. *Thin Solid Films*, **480**–**481**, 55–60.

49. Mardare, D., Tasca, M., Delibas, M., and Rusu, G.I. (2000) On the structural properties and optical transmittance of TiO2 r.f. sputtered thin films. *Appl. Surf. Sci.*, **156**, 200–206.

50. Wada, T., Kohara, N., Nishiwaki, S., and Negami, T. (2001) Characterization of the Cu(In,Ga)Se2/Mo interface in CIGS solar cells. *Thin Solid Films*, **387** (1–2), 118–122.

51. Mudryi, A. V., Gremenok, V.F., Karotki, A. V., Zalesski, V.B., Yakushev, M. V., Luckert, F., and Martin, R. (2010) Structural and optical properties of thin films of Cu(In,Ga)Se2 semiconductor compounds. *J. Appl. Spectrosc.*, **77** (3).

52. Contreras, M.A., Romero, M.J., To, B., Hasoon, F., Noufi, R., Ward, S., and Ramanathan, K. (2002) Optimization of CBD CdS process in high-efficiency Cu(In,Ga)Se2-based solar cells. *Thin Solid Films*, **403**–**404**, 204–211.

53. Rau, U., and Schmidt, M. (2001) Electronic properties of ZnO/CdS/Cu(In,Ga)Se2 solar cells - aspects of heterojunction formation. *Thin Solid Films*, **387**, 141–146.

54. Baek, M., Zafar, M., Kim, S., Kim, D.H., Jeon, C.W., Lee, J., and Yong, K. (2018) Enhancing Durability and Photoelectrochemical Performance of the Earth Abundant Ni–Mo/TiO2/CdS/CIGS Photocathode under Various pH Conditions. *ChemSusChem*, **11** (20), 3679–3688.

55. Walter, M.G., Warren, E.L., McKone, J.R., Boettcher, S.W., Mi, Q., Santori, E.A., and Lewis, N.S. (2010) Solar water splitting cells. *Chem. Rev.*, **110** (11), 6446–6473.

56. Hibbert, D.B., and Churchill, C.R. (1984) Kinetics of the electrochemical evolution of isotopically enriched gases. Part 2.—18O16O evolution on NiCo2O4 and LixCo3–xO4 in alkaline solution. *J. Chem. Soc. Faraday Trans. 1 Phys. Chem. Condens. Phases*, **80** (7), 1965–1975.

57. Hibbert, D.B. (1980) The electrochemical evolution of O2 on NiCo2O4 in 18O-enriched KOH. *J. Chem. Soc. Chem. Commun.*, 202–203.

58. Willsau, J., Wolter, O., and Heitbaum, J. (1985) Does the oxide layer take part in the oxygen evolution reaction on platinum?: A DEMS study. *J. Electroanal. Chem. Interfacial Electrochem.*, **195** (2), 299–306.

59. Wohlfahrt-Mehrens, M., and Heitbaum, J. (1987) Oxygen evolution on Ru and RuO2 electrodes studied using isotope labelling and on-line mass spectrometry. *J. Electroanal.*

Chem. Interfacial Electrochem., **237** (2), 251–260.

60. Seabold, J.A., and Choi, K.-S. (2012) Efficient and Stable Photo-Oxidation of Water by a Bismuth Vanadate Photoanode Coupled with an Iron Oxyhydroxide Oxygen Evolution Catalyst. *J. Am. Chem. Soc.*, **134** (4), 2186–2192.

61. Steinmiller, E.M.P., and Choi, K.S. (2009) Photochemical deposition of cobalt-based oxygen evolving catalyst on a semiconductor photoanode for solar oxygen production. *Proc. Natl. Acad. Sci. U. S. A.*, **106** (49), 20633.

62. Duan, L., Bozoglian, F., Mandal, S., Stewart, B., Privalov, T., Llobet, A., and Sun, L. (2012) A molecular ruthenium catalyst with water-oxidation activity comparable to that of photosystem II. *Nat. Chem.*, **4** (5), 418–423.

63. Schipper, D.E., Zhao, Z., Leitner, A.P., Xie, L., Qin, F., Alam, M.K., Chen, S., Wang, D., Ren, Z., Wang, Z., Bao, J., and Whitmire, K.H. (2017) A TiO2/FeMnP Core/Shell Nanorod Array Photoanode for Efficient Photoelectrochemical Oxygen Evolution. *ACS Nano*, **11** (4), 4051–4059.

64. Poli, I., Hintermair, U., Regue, M., Kumar, S., Sackville, E. V., Baker, J., Watson, T.M., Eslava, S., and Cameron, P.J. (2019) Graphite-protected CsPbBr3 perovskite photoanodes functionalised with water oxidation catalyst for oxygen evolution in water. *Nat. Commun.*, **10**, 2097.

65. Sheehan, S.W., Thomsen, J.M., Hintermair, U., Crabtree, R.H., Brudvig, G.W., and Schmuttenmaer, C.A. (2015) A molecular catalyst for water oxidation that binds to metal oxide surfaces. *Nat. Commun.*, **6**, 6469.

66. Duan, L., Tong, L., Xu, Y., and Sun, L. (2011) Visible light-driven water oxidation - From molecular catalysts to photoelectrochemical cells. *Energy Environ. Sci.*, **4** (9), 3296–3313.

67. Chang, X., Wang, T., Zhang, P., Zhang, J., Li, A., and Gong, J. (2015) Enhanced Surface Reaction Kinetics and Charge Separation of p-n Heterojunction Co3O4/BiVO4 Photoanodes. *J. Am. Chem. Soc.*, **137** (26), 8356–8359.

68. Grewe, T., Deng, X., and Tüysüz, H. (2014) Influence of Fe doping on structure and water oxidation activity of nanocast Co3O4. *Chem. Mater.*, **26** (10), 3162–3168.

69. Laouini, E., Berghoute, Y., Douch, J., Mendonça, M.H., Hamdani, M., and Pereira, M.I.S. (2009) Electrochemical behaviour of Fe x Co3-x O4 with (x = 0, 1, 2 and 3) oxides thin film electrodes in alkaline medium. *J. Appl. Electrochem.*, **39** (12), 2469–2479.

70. Laouini, E., Hamdani, M., Pereira, M.I.S., Douch, J., Mendonça, M.H., Berghoute, Y., and Singh, R.N. (2008) Preparation and electrochemical characterization of spinel type Fe-Co3O4 thin film electrodes in alkaline medium. *Int. J. Hydrogen Energy*, **33** (19), 4936–4944.

71. Zhong, D.K., and Gamelin, D.R. (2010) Photo-electrochemical water oxidation by cobalt catalyst ("Co-Pi")/α-Fe2O3 composite photoanodes: Oxygen evolution and resolution of a kinetic bottleneck. *J. Am. Chem. Soc.*, **132** (12), 4202–4207.

72. Zhong, D.K., Cornuz, M., Sivula, K., Grätzel, M., and Gamelin, D.R. (2011) Photo-assisted electrodeposition of cobalt-phosphate (Co-Pi) catalyst on hematite photoanodes for solar water oxidation. *Energy Environ. Sci.*, **4** (5), 1759–1764.

73. Barroso, M., Cowan, A.J., Pendlebury, S.R., Grätzel, M., Klug, D.R., and Durrant, J.R. (2011) The role of cobalt phosphate in enhancing the photocatalytic activity of α-Fe 2O 3

toward water oxidation. *J. Am. Chem. Soc.*, **133** (38), 14868–14871.

74. Fan, X., Gao, B., Wang, T., Huang, X., Gong, H., Xue, H., Guo, H., Song, L., Xia, W., and He, J. (2016) Layered double hydroxide modified WO3 nanorod arrays for enhanced photoelectrochemical water splitting. *Appl. Catal. A Gen.*, **528**, 52–58.

75. Yuan, S.Y., Jiang, L.W., Hu, J.S., Liu, H., and Wang, J.J. (2023) Fully Dispersed IrOx Atomic Clusters Enable Record Photoelectrochemical Water Oxidation of Hematite in Acidic Media. *Nano Lett.*, **23** (6), 2354–2361.

76. Zachäus, C., Abdi, F.F., Peter, L.M., and Van De Krol, R. (2017) Photocurrent of BiVO4 is limited by surface recombination, not surface catalysis. *Chem. Sci.*, **8** (5), 3712–3719.

77. Dong, G., Hu, H., Wang, L., Zhang, Y., and Bi, Y. (2018) Remarkable enhancement on photoelectrochemical water splitting derived from well-crystallized Bi2WO6 and Co(OH)x with tunable oxidation state. *J. Catal.*, **366**, 258–265.

78. Wang, S., He, T., Yun, J.-H., Hu, Y., Xiao, M., Du, A., Wang, L., Wang, S., Yun, J., Hu, Y., Xiao, M., Wang, L., He, T., and Du, A. (2018) New Iron-Cobalt Oxide Catalysts Promoting BiVO4 Films for Photoelectrochemical Water Splitting. *Adv. Funct. Mater.*, **28** (34), 1802685.

79. Feng, T., Zhao, X.R., Dong, C.K., Liu, H., Du, X.W., and Yang, J. (2018) Boosting reversible oxygen electrocatalysis with enhanced interfacial pyridinic-N-Co bonding in cobalt oxide/mesoporous N-doped graphene hybrids. *Nanoscale*, **10** (47), 22140–22147.

80. Hao, J., Yang, W., Peng, Z., Zhang, C., Huang, Z., and Shi, W. (2017) A Nitrogen Doping Method for CoS2 Electrocatalysts with Enhanced Water Oxidation Performance. *ACS Catal.*, **7** (6), 4214–4220.

81. Galán-Mascarós, J.R. (2015) Water Oxidation at Electrodes Modified with Earth-Abundant Transition-Metal Catalysts. *ChemElectroChem*, **2** (1), 37–50.

82. Goberna-Ferrón, S., Hernández, W.Y., Rodríguez-García, B., and Galán-Mascarós, J.R. (2014) Light-driven water oxidation with metal hexacyanometallate heterogeneous catalysts. *ACS Catal.*, **4** (6), 1637–1641.

83. Pintado, S., Goberna-Ferrón, S., Escudero-Adán, E.C., and Galán-Mascarós, J.R. (2013) Fast and persistent electrocatalytic water oxidation by Co-Fe Prussian blue coordination polymers. *J. Am. Chem. Soc.*, **135** (36), 13270–13273.

84. Morales-Guio, C.G., Stern, L.A., and Hu, X. (2014) Nanostructured hydrotreating catalysts for electrochemical hydrogen evolution. *Chem. Soc. Rev.*, **43** (18), 6555–6569.

85. Gileadi, E. (2011) *Physical Electrochemistry. Fundamentals, Techniques and Applications*, Wiley-VCH Verlag GmbH & Co., Weinheim.

86. Greeley, J., Jaramillo, T.F., Bonde, J., Chorkendorff, I., and Nørskov, J.K. (2006) Computational high-throughput screening of electrocatalytic materials for hydrogen evolution. *Nat. Mater.*, **5** (11), 909–913.

87. Miles, M.H., and Thomason, M.A. (1976) Periodic Variations of Overvoltages for Water Electrolysis in Acid Solutions from Cyclic Voltammetric Studies. *J. Electrochem. Soc.*, **123**, 1459.

88. Xu, Y., and Xu, R. (2015) Nickel-based cocatalysts for photocatalytic hydrogen production. *Appl. Surf. Sci.*, **351**, 779–793.

89. Raj, I.A., and Vasu, K.I. (1990) Transition metal-based hydrogen electrodes in alkaline solution - electrocatalysis on nickel based binary alloy coatings. *J. Appl. Electrochem.*, **20** (1).

90. Huot, J.Y. (1989) Hydrogen Evolution and Interface Phenomena on a Nickel Cathode in 30 w/o KOH : I. Kinetics Parameters and Electrode Impedance Between 303 and 363 K. *J. Electrochem. Soc*, **136**, 1933.

91. G Rommal, H.E., and Moran, P.J. (1985) Time-Dependent Energy Efficiency Losses at Nickel Cathodes in Alkaline Water Electrolysis Systems. *J. Electrochem. Soc.*, **132**, 325–329.

92. Park, S.W., Kim, I., Oh, S.I., Kim, J.C., and Kim, D.W. (2018) Carbon-encapsulated NiFe nanoparticles as a bifunctional electrocatalyst for high-efficiency overall water splitting. *J. Catal.*, **366**, 266–274.

93. Kumar, B., M. Smieja, J., and P. Kubiak, C. (2010) Photoreduction of CO2 on p-type Silicon Using Re(bipy-But)(CO)3Cl: Photovoltages Exceeding 600 mV for the Selective Reduction of CO2 to CO. *J. Phys. Chem. C*, **114** (33), 14220–14223.

94. Hou, Y., Abrams, B.L., Vesborg, P.C.K., Björketun, M.E., Herbst, K., Setti, A.M., Damsgaard, C.D., Pedersen, T., Hansen, O., Rossmeisl, J., Dahl, S., Nørskov, J.K., and Chorkendorff, I. (2011) Bioinspired molecular co-catalysts bonded to a silicon photocathode for solar hydrogen evolution. *Nat. Mater.*, **10**, 434–438.

95. Gu, J., Yan, Y., Young, J.L., Steirer, K.X., Neale, N.R., and Turner, J.A. (2016) Water reduction by a p-GaInP 2 photoelectrode stabilized by an amorphous TiO 2 coating and a molecular cobalt catalyst. *Nat. Mater.*, **15**, 456–462.

96. Khusnutdinova, D., Beiler, A.M., Wadsworth, B.L., Jacob, S.I., and Moore, G.F. (2016) Metalloporphyrin-modified semiconductors for solar fuel production. *Chem. Sci.*, **8** (1), 253–259.

97. M. Gurrentz, J., and J. Rose, M. (2020) Non-Catalytic Benefits of Ni(II) Binding to an Si(111)-PNP Construct for Photoelectrochemical Hydrogen Evolution Reaction: Metal Ion Induced Flat Band Potential Modulation. *J. Am. Chem. Soc.*, **142** (12), 5657–5667.

98. Hanna, C.M., Pekarek, R.T., Miller, E.M., Yang, J.Y., and Neale, N.R. (2020) Decoupling Kinetics and Thermodynamics of Interfacial Catalysis at a Chemically Modified Black Silicon Semiconductor Photoelectrode. *ACS Energy Lett.*, **5** (6), 1848–1855.

99. L. Wadsworth, B., P. Nguyen, N., Nishiori, D., M. Beiler, A., and F. Moore, G. (2020) Addressing the Origin of Photocurrents and Fuel Production Activities in Catalyst-Modified Semiconductor Electrodes. *ACS Appl. Energy Mater.*, **3** (8), 7512–7519.

100. Laurans, M., Wells, J.A.L., and Ott, S. (2021) Immobilising molecular Ru complexes on a protective ultrathin oxide layer of p-Si electrodes towards photoelectrochemical CO2reduction. *Dalt. Trans.*, **50** (30), 10482–10492.

101. A. Reyes Cruz, E., Nishiori, D., L. Wadsworth, B., P. Nguyen, N., K. Hensleigh, L., Khusnutdinova, D., M. Beiler, A., and F. Moore, G. (2022) Molecular-Modified Photocathodes for Applications in Artificial Photosynthesis and Solar-to-Fuel Technologies. *Chem. Rev.*, **122** (21), 16051–16109.

102. Wen, Z., Xu, S., Zhu, Y., Liu, G., Gao, H., Sun, L., and Li, F. (2022) Aqueous CO2 Reduction on Si Photocathodes Functionalized by Cobalt Molecular Catalysts/Carbon

Nanotubes. *Angew. Chemie Int. Ed.*, **61** (24), e202201086.

103. Shang, B., Rooney, C.L., Gallagher, D.J., Wang, B.T., Krayev, A., Shema, H., Leitner, O., Harmon, N.J., Xiao, L., Sheehan, C., Bottum, S.R., Gross, E., Cahoon, J.F., Mallouk, T.E., and Wang, H. (2023) Aqueous Photoelectrochemical CO 2 Reduction to CO and Methanol over a Silicon Photocathode Functionalized with a Cobalt Phthalocyanine Molecular Catalyst. *Angew. Chem. Int. Ed*, **62**.

104. Marcus, R.A. (1965) On the Theory of Electron-Transfer Reactions. VI. Unified Treatment for Homogeneous and Electrode Reactions. *J. Chem. Phys.*, **43** (2), 679–701.

105. Gerischer, H. (1969) Charge transfer processes at semiconductor-electrolyte interfaces in connection with problems of catalysis. *Surf. Sci.*, **18** (1), 97–122.

106. Willig, F., and L., G. (2014) Redox Processes at Semiconductors-Gerischer Model and Beyond. , 10.1007/978-1-4419-6996-5_41, in *Encyclopedia of Applied Electrochemistry* (eds.Kreysa, G., Ota, K., and Savinell, R.F.), Springer, New York, pp. 1786–1798.

107. Memming, R. (2015) *Semiconductor Electrochemistry*, Wiley-VCH, Weinheim.

108. Ross, R.T., and Nozik, A.J. (1982) Efficiency of hot-carrier solar energy converters. *J. Appl. Phys.*, **53** (5), 3813.

109. Cooper, G., Turner, J.A., and Parkinson, B.A. (1983) Hot carrier injection of photogenerated electrons at indium phosphide-electrolyte interfaces. *J. Appl. Phys.*, **54** (11), 6463.

110. A. Koval, C., and R. Segar, P. (2002) Mechanistic aspects of reductions by hot electrons in p-indium phosphide/acetonitrile photoelectrochemical cells. *J. Phys. Chem.*, **94** (5), 2033–2039.

111. Tisdale, W.A., Williams, K.J., Timp, B.A., Norris, D.J., Aydil, E.S., and Zhu, X.Y. (2010) Hot-electron transfer from semiconductor nanocrystals. *Science (80-.).*, **328** (5985), 1543–1547.

112. Zhang, C., Fan, Y., and Huang, X. (2020) Hot-carrier transfer at photocatalytic silicon/platinum interfaces. *J. Chem. Phys*, **152**, 144705.

113. B. Bocarsly, A., C. Bookbinder, D., N. Dominey, R., S. Lewis, N., and S. Wrighton, M. (2002) Photoreduction at illuminated p-type semiconducting silicon photoelectrodes. Evidence for Fermi level pinning. *J. Am. Chem. Soc.*, **102** (11), 3683–3688.

114. S. Wrighton, M. (2002) Photoelectrochemical conversion of optical energy to electricity and fuels. *Acc. Chem. Res.*, **12** (9), 303–310.

115. Kohlrausch, R. (1854) Theorie des elektrischen Rückstandes in der Leidener Flasche. *Ann. Phys.*, **167** (1), 56–82.

116. Williams, G., and Watts, D.C. (1970) Non-symmetrical dielectric relaxation behaviour arising from a simple empirical decay function. *Trans. Faraday Soc.*, **66**, 80–85.

117. Toussaint, D., and Wilczek, F. (1983) Particle–antiparticle annihilation in diffusive motion. *J. Chem. Phys.*, **78** (5), 2642–2647.

118. Nelson, J., Haque, S.A., Klug, D.R., and Durrant, J.R. (2001) Trap-limited recombination in dye-sensitized nanocrystalline metal oxide electrodes. *Phys. Rev. B - Condens. Matter Mater. Phys.*, **63** (20).

119. Montanari, I., Nogueira, A.F., Nelson, J., Durrant, J.R., Winder, C., Loi, M.A., Sariciftci,

N.S., and Brabec, C. (2002) Transient optical studies of charge recombination dynamics in a polymer/fullerene composite at room temperature. *Appl. Phys. Lett.*, **81** (16), 3001–3003.

120. Ravensbergen, J., Abdi, F.F., Van Santen, J.H., Frese, R.N., Dam, B., Van De Krol, R., and Kennis, J.T.M. (2014) Unraveling the carrier dynamics of BiVO4: A femtosecond to microsecond transient absorption study. *J. Phys. Chem. C*, **118** (48), 27793–27800.

121. Ponomarev, E.A., and Peter, L.M. (1995) A generalized theory of intensity modulated photocurrent spectroscopy (IMPS). *J. Electroanal. Chem.*, **396** (1–2), 219–226.

122. Peat, R., and Peter, L.M. (1987) Intensity Modulated Photocurrent Spectroscopy of n-GaAs. *Berichte der Bunsengesellschaft/Physical Chem. Chem. Phys.*, **91** (4), 381–386.

123. Li, J., and Peter, L.M. (1985) Surface recombination at semiconductor electrodes: Part III. Steady-state and intensity modulated photocurrent response. *J. Electroanal. Chem. Interfacial Electrochem.*, **193** (1–2), 27–47.

124. Peter, L.M. (1990) Dynamic aspects of semiconductor photoelectrochemistry. *Chem. Rev.*, **90** (5), 753–769.

125. Peter, L.M., and Vanmaekelbergh, D. (2008) Time and frequency resolved studies of photoelectrochemical kinetics. *Adv. Electrochem. Sci. Eng.*, **6**, 77–163.

126. Peter, L.M. (2013) Energetics and kinetics of light-driven oxygen evolution at semiconductor electrodes: The example of hematite. *J. Solid State Electrochem.*, **17** (2), 315–326.

127. Klotz, D., Grave, D.A., Dotan, H., and Rothschild, A. (2018) Empirical Analysis of the Photoelectrochemical Impedance Response of Hematite Photoanodes for Water Photo-oxidation. *J. Phys. Chem. Lett.*, **9** (6), 1466–1472.

128. Fermín, D.J., Ponomarev, E.A., and Peter, L.M. (1999) Kinetic study of CdS photocorrosion by intensity modulated photocurrent and photoelectrochemical impedance spectroscopy. *J. Electroanal. Chem.*, **473** (1), 192–203.

129. Rodriguez-Gutierrez, I., Souza Junior, J.B., Leite, E.R., Vayssieres, L., and Souza, F.L. (2021) An intensity modulated photocurrent spectroscopy study of the role of titanium in thick hematite photoanodes. *Appl. Phys. Lett.*, **119** (7).

130. Rodríguez-Gutiérrez, I., Djatoubai, E., Su, J., Vega-Poot, A., Rodríguez-Gattorno, G., Souza, F.L., and Oskam, G. (2020) An intensity-modulated photocurrent spectroscopy study of the charge carrier dynamics of WO3/BiVO4 heterojunction systems. *Sol. Energy Mater. Sol. Cells*, **208**, 110378.

131. Hadamard, J. (1902) Sur les problèmes aux dérivées partielles et leur signification physique. *Princet. Univ. Bull.*, **13**, 49–52.

132. Saccoccio, M., Wan, T.H., Chen, C., and Ciucci, F. (2014) Optimal regularization in distribution of relaxation times applied to electrochemical impedance spectroscopy: Ridge and Lasso regression methods - A theoretical and experimental Study. *Electrochim. Acta*, **147**, 470–482.

133. Hahn, M., Schindler, S., Triebs, L.-C., and Danzer, M.A. (2019) Optimized Process Parameters for a Reproducible Distribution of Relaxation Times Analysis of Electrochemical Systems. *Batteries*, **5** (2), 43.

134. Pendlebury, S.R., Cowan, A.J., Barroso, M., Sivula, K., Ye, J., Grätzel, M., Klug, D.R., Tang, J., and Durrant, J.R. (2012) Correlating long-lived photogenerated hole populations

with photocurrent densities in hematite water oxidation photoanodes. *Energy Environ. Sci.*, **5** (4), 6304–6312.

135. El-Zohry, A.M., Turedi, B., Alsalloum, A., Maity, P., Bakr, O.M., Ooi, B.S., and Mohammed, O.F. (2022) Ultrafast transient infrared spectroscopy for probing trapping states in hybrid perovskite films. *Commun. Chem.*, **5** (1), 1–7.

136. Gärtner, W.W. (1959) Depletion-layer photoeffects in semiconductors. *Phys. Rev.*, **116** (1), 84–87.

137. Bedoya-Lora, F.E., Valencia-García, M.E., Hankin, A., Klotz, D., and Calderón, J.A. (2022) Determination of photon-driven charge transfer efficiency: Drawbacks, accuracy and precision of different methods using Hematite as case of study. *Electrochim. Acta*, **402**, 139559.

138. Hankin, A., Bedoya-Lora, F.E., Alexander, J.C., Regoutz, A., and Kelsall, G.H. (2019) Flat band potential determination: Avoiding the pitfalls. *J. Mater. Chem. A*, **7** (45), 26162–26176.

139. Sivula, K. (2021) Mott–Schottky Analysis of Photoelectrodes: Sanity Checks Are Needed. *ACS Energy Lett.*, **6** (7), 2549–2551.

140. Schroder, D.K., Thomas, R.N., and Swartz, J.C. (1978) Free Carrier Absorption in Silicon. *IEEE J. Solid-State Circuits*, **13** (1).

141. Dousmanis, G.C. (1959) Effects of Carrier Injection on the Recombination Velocity in Semiconductor Surfaces. *J. Appl. Phys.*, **30** (2), 180–184.

142. Memming, R. (1964) Surface recombination at higher injection levels. *Surf. Sci.*, **1** (1), 88–101.

143. Lewerenz, H.J. (1993) Surface states and Fermi level pinning at semiconductor/ electrolyte junctions. *J. Electroanal. Chem.*, **356** (1–2), 121–143.

144. J. Bard, A., B. Bocarsly, A., Ren F. Fan, F., G. Walton, E., and S. Wrighton, M. (2002) The concept of Fermi level pinning at semiconductor/liquid junctions. Consequences for energy conversion efficiency and selection of useful solution redox couples in solar devices. *J. Am. Chem. Soc.*, **102** (11), 3671–3677.

145. Hauser, J.R., and Littlejohn, M.A. (1968) Approximations for accumulation and inversion space-charge layers in semiconductors. *Solid State Electron.*, **11** (7), 667–674.

146. Demoulin, E., and van de Wiele, F. (1974) Inversion layer at the interface of Schottky diodes. *Solid State Electron.*, **17** (8), 825–833.

147. Turner, J.A., Manassen, J., and Nozik, A.J. (1980) Photoelectrochemistry with p-Si electrodes: Effects of inversion. *Appl. Phys. Lett.*, **37** (5), 488–491.

148. Lewis, N.S. (1984) A Quantitative Investigation of the Open-Circuit Photovoltage at the Semiconductor/Liquid Interface. *J. Electrochem. Soc.*, **131** (11).

149. Bard, A.J., Fan, F.R.F., Gioda, A.S., Nagasubramanian, G., and White, H.S. (1980) On the role of surface states in semiconductor electrode photoelectrochemical cells. *Faraday Discuss. Chem. Soc.*, **70**, 19–31.

150. Stevenson, D.T., and Keyes, R.J. (1954) Measurements of the recombination velocity at germanium surfaces. *Physica*, **20** (7–12), 1041–1046.

151. J. Michalak, D., Gstrein, F., and S. Lewis, N. (2008) The Role of Band Bending in Affecting

the Surface Recombination Velocities for Si(111) in Contact with Aqueous Acidic Electrolytes. *J. Phys. Chem. C*, **112** (15), 5911–5921.

152. Sinton, R.A., and Swanson, R.M. (1987) Recombination in Highly Injected Silicon. *IEEE Trans. Electron Devices*, **34** (6), 1380–1389.

153. Hangleiter, A., and Häcker, R. (1990) Enhancement of band-to-band Auger recombination by electron-hole correlations. *Phys. Rev. Lett.*, **65** (2), 215.

154. Schröder, D.K. (1997) Carrier lifetimes in silicon. *IEEE Trans. Electron Devices*, **44** (1), 160–170.

155. Singh, R., Green, M.A., and Rajkanan, K. (1981) Review of conductor-insulator-semiconductor (CIS) solar cells. *Sol. Cells*, **3** (2), 95–148.

156. K. Eggers, P., Darwish, N., N. Paddon-Row, M., and Justin Gooding, J. (2012) Surface-Bound Molecular Rulers for Probing the Electrical Double Layer. *J. Am. Chem. Soc.*, **134** (17), 7539–7544.

157. Kumar Bhowmick, D., Joe Urban, A., Bartsch, M., Braunschweig, B., and Zacharias, H. (2022) Near-UV-Induced Rapid Formation of Compact Self-Assembled Organophosphonate Monolayers on H-Terminated Si(111) Surfaces. *J. Phys. Chem. C*, **126** (47), 19978–19986.

158. Grimm, R.L., Bierman, M.J., O'Leary, L.E., Strandwitz, N.C., Brunschwig, B.S., and Lewis, N.S. (2012) Comparison of the photoelectrochemical behavior of h-terminated and methyl-terminated Si(111) surfaces in contact with a series of one-electron, outer-sphere redox couples in CH 3CN. *J. Phys. Chem. C*, **116** (44), 23569–23576.

159. G. Boucher, D., Kearney, K., Ertekin, E., and J. Rose, M. (2021) Tuning p-Si(111) Photovoltage via Molecule|Semiconductor Electronic Coupling. *J. Am. Chem. Soc.*, **143** (6), 2567–2580.

160. Reed, A.H., and Yeager, E. (1970) Infra-red internal reflexion studies of the germanium/electrolyte interface. *Electrochim. Acta*, **15** (8), 1345–1354.

161. Harrick, N.J. (1962) Optical Spectrum of the Semiconductor Surface States from Frustrated Total Internal Reflections. *Phys. Rev.*, **125** (4), 1165.

162. Ren F. Fan, F., and J. Bard, A. (2002) Semiconductor electrodes. 24. Behavior of photoelectrochemical cells based on p-type gallium arsenide in aqueous solutions. *J. Am. Chem. Soc.*, **102** (11), 3677–3683.

163. Dare-Edwards, M.P., Bard, A.J., Faulkner, L.R., Bockris, J.O.M., Khan, S.U.M., Uosaki, K., Gerischer, H., Nozik, A.J., Schumacher, R., Ellis, A.B., Harzion, Z., Albery, W.J., Davidson, R.S., Perone, S.P., Richardson, J.H., Archer, M.D., Gissler, W., Pichat, P., Ginley, D.S., Jarrett, H.S., Butler, M.A., Armstrong, N., Gomes, W.P., Peter, L.M., Froelicher, M., Malati, M.A., Lemasson, P., Potter, R., Hamnett, A., and Sprünken, H.R. (1980) General discussion. *Faraday Discuss. Chem. Soc.*, **70**, 93–132.

164. D. E. Forbes, M., and S. Lewis, N. (2002) Real-time measurements of interfacial charge transfer rates at silicon/liquid junctions. *J. Am. Chem. Soc.*, **112** (9), 3682–3683.

165. Swiatkowski, C., Sanders, A., and Buhre, K.-D. (1995) Charge-carrier kinetics in semiconductors by microwave conductivity measurements. *J. Appl. Phys.*, **78** (3), 1763.

166. M. Vasquez, R., Hlynchuk, S., and Maldonado, S. (2020) Effect of Covalent Surface Functionalization of Si on the Activity of Trifluoromethanesulfonic Anhydride for

Suppressing Surface Recombination. *ACS Appl. Mater. & Interfaces*, **12** (51), 57560–57568.

167. Dousmanis, G.C. (1958) Semiconductor Surface Potential and Surface States from Field-Induced Changes in Surface Recombination. *Phys. Rev.*, **112** (2), 369–380.

168. Adamowicz, B., and Hasegawa, H. (1998) Computer analysis of surface recombination process at Si and compound semiconductor surfaces and behavior of surface recombination velocity. *Japanese J. Appl. Physics, Part 1 Regul. Pap. Short Notes Rev. Pap.*, **37**, 1631–1637.

169. Nedeljkovic, M., Soref, R., and Mashanovich, G.Z. (2011) Free-carrier electrorefraction and electroabsorption modulation predictions for silicon over the 1-14-μm infrared wavelength range. *IEEE Photonics J.*, **3** (6), 1171–1180.

170. Iqbal, A., and Bevan, K.H. (2018) The impact of boundary conditions on calculated photovoltages and photocurrents at photocatalytic interfaces. *MRS Commun.*, **8** (2), 466–473.

171. Sampaio, R.N., Li, G., and J. Meyer, G. (2019) Flipping Molecules over on TiO2 Surfaces with Light and Electric Fields. *J. Am. Chem. Soc.*, **141** (35), 13898–13904.

172. Venkateswara Rao, A., Chazalviel, J.N., and Ozanam, F. (1986) In situ characterization of the n-Si/acetonitrile interface by electromodulated infrared internal-reflection spectroscopy. *J. Appl. Phys.*, **60** (2), 696–706.

173. F. Fan, F.-R., S. White, H., L. Wheeler, B., and J. Bard, A. (2002) Semiconductor electrodes. 31. Photoelectrochemistry and photovoltaic systems with n- and p-type tungsten selenide (WSe2) in aqueous solution. *J. Am. Chem. Soc.*, **102** (16), 5142–5148.

174. White, H.S., Fan, F.F., and Bard, A.J. (1981) Semiconductor Electrodes: XXXIII . Photoelectrochemistry of n-Type in Acetonitrile. *J. Electrochem. Soc.*, **128** (5), 1045–1055.

175. Lin, J., Han, X., Liu, S., Lv, Y., Li, X., Zhao, Y., Li, Y., Wang, L., and Zhu, S. (2023) Nitrogen-doped cobalt-iron oxide cocatalyst boosting photoelectrochemical water splitting of BiVO4 photoanodes. *Appl. Catal. B Environ.*, **320**, 121947.

176. Moss, B., Hegner, F.S., Corby, S., Selim, S., Francàs, L., López, N., Giménez, S., Galán-Mascarós, J.-R., and Durrant, J.R. (2019) Unraveling Charge Transfer in CoFe Prussian Blue Modified BiVO4 Photoanodes. *ACS Energy Lett.*, **4** (1), 337–342.

177. Grigioni, I., G. Stamplecoskie, K., Selli, E., and V. Kamat, P. (2015) Dynamics of Photogenerated Charge Carriers in WO3/BiVO4 Heterojunction Photoanodes. *J. Phys. Chem. C*, **119** (36), 20792–20800.

178. Selim, S., Francàs, L., García-Tecedor, M., Corby, S., Blackman, C., Gimenez, S., Durrant, J.R., and Kafizas, A. (2019) WO3/BiVO4: impact of charge separation at the timescale of water oxidation. *Chem. Sci.*, **10** (9), 2643–2652.

179. Ma, Y., Pendlebury, S.R., Reynal, A., Le Formal, F., and Durrant, J.R. (2014) Dynamics of photogenerated holes in undoped BiVO4 photoanodes for solar water oxidation. *Chem. Sci.*, **5** (8), 2964–2973.

180. Cowan, A.J., and Durrant, J.R. (2013) Long-lived charge separated states in nanostructured semiconductor photoelectrodes for the production of solar fuels. *Chem. Soc. Rev*, **42**, 2281.

181. Aiga, N., Jia, Q., Watanabe, K., Kudo, A., Sugimoto, T., and Matsumoto, Y. (2013) Electron–Phonon Coupling Dynamics at Oxygen Evolution Sites of Visible-Light-Driven

Photocatalyst: Bismuth Vanadate. *J. Phys. Chem. C*, **117** (19), 9881–9886.

182. M. Pesci, F., J. Cowan, A., D. Alexander, B., R. Durrant, J., and R. Klug, D. (2011) Charge Carrier Dynamics on Mesoporous WO3 during Water Splitting. *J. Phys. Chem. Lett.*, **2** (15), 1900–1903.

183. Corby, S., Francàs, L., Selim, S., Sachs, M., Blackman, C., Kafizas, A., and Durrant, J.R. (2018) Water Oxidation and Electron Extraction Kinetics in Nanostructured Tungsten Trioxide Photoanodes. *J. Am. Chem. Soc.*, **140** (47), 16168–16177.

184. Bochud, T., and Challet, D. (2007) Optimal approximations of power laws with exponentials: Application to volatility models with long memory. *Quant. Financ.*, **7** (6), 585–589.

185. Shi, Q., Murcia-López, S., Tang, P., Flox, C., R. Morante, J., Bian, Z., Wang, H., and Andreu, T. (2018) Role of Tungsten Doping on the Surface States in BiVO4 Photoanodes for Water Oxidation: Tuning the Electron Trapping Process. *ACS Catal.*, **8** (4), 3331–3342.

186. Hu, J., Zhao, X., Chen, W., Su, H., and Chen, Z. (2017) Theoretical Insight into the Mechanism of Photoelectrochemical Oxygen Evolution Reaction on BiVO4 Anode with Oxygen Vacancy. *J. Phys. Chem. C*, **121** (34), 18702–18709.

187. Yalavarthi, R., Zbořil, R., Schmuki, P., Naldoni, A., and Kment, S. (2021) Elucidating the role of surface states of BiVO 4 with Mo doping and a CoOOH co-catalyst for photoelectrochemical water splitting. *J. Power Sources*, **483**, 229080.

188. Tang, J., Durrant, J.R., and Klug, D.R. (2008) Mechanism of photocatalytic water splitting in TiO2. Reaction of water with photoholes, importance of charge carrier dynamics, and evidence for four-hole chemistry. *J. Am. Chem. Soc.*, **130** (42), 13885–13891.

189. Cowan, A.J., Tang, J., Leng, W., Durrant, J.R., and Klug, D.R. (2010) Water splitting by nanocrystalline TiO 2 in a complete photoelectrochemical cell exhibits efficiencies limited by charge recombination. *J. Phys. Chem. C*, **114** (9), 4208–4214.

190. Green, M.A., Dunlop, E.D., Yoshita, M., Kopidakis, N., Bothe, K., Siefer, G., and Hao, X. (2023) Solar cell efficiency tables (version 62). *Prog. Photovoltaics Res. Appl.*, **31** (7), 651–663.

191. Ramanathan, K., Contreras, M.A., Perkins, C.L., Asher, S., Hasoon, F.S., Keane, J., Young, D., Romero, M., Metzger, W., Noufi, R., Ward, J., and Duda, A. (2003) Properties of 19.2% efficiency ZnO/CdS/CuInGaSe2 thin-film solar cells. *Prog. Photovoltaics Res. Appl.*, **11** (4), 225–230.

192. Repins, I., Contreras, M.A., Egaas, B., DeHart, C., Scharf, J., Perkins, C.L., To, B., and Noufi, R. (2008) 19.9%-efficient ZnO/CdS/CuInGaSe2 solar cell with 81.2% fill factor. *Prog. Photovoltaics Res. Appl.*, **16** (3), 235–239.

193. Luo, J., Li, Z., Nishiwaki, S., Schreier, M., Mayer, M.T., Cendula, P., Lee, Y.H., Fu, K., Cao, A., Nazeeruddin, M.K., Romanyuk, Y.E., Buecheler, S., Tilley, S.D., Wong, L.H., Tiwari, A.N., and Grätzel, M. (2015) Targeting Ideal Dual-Absorber Tandem Water Splitting Using Perovskite Photovoltaics and CuInxGa1-xSe2 Photocathodes. *Adv. Energy Mater.*, **5** (24).

194. Kim, M. woo, Yoon, H., Ohm, T.Y., Mali, M.G., Choi, S.K., Park, H., Al-Deyab, S.S., Lim, D.C., Ahn, S.J., and Yoon, S.S. (2017) Platinum-decorated Cu(InGa)Se2/CdS photocathodes: Optimization of Pt electrodeposition time and pH level. *J. Alloys Compd.*, **692**, 294–300.

195. Peter, L.M., Ponomarev, E.A., Franco, G., and Shaw, N.J. (1999) Aspects of the photoelectrochemistry of nanocrystalline systems. *Electrochim. Acta*, **45**, 549–560.

196. Bou, A., Āboliņš, H., Ashoka, A., Cruanyes, H., Guerrero, A., Deschler, F., and Bisquert, J. (2021) Extracting in Situ Charge Carrier Diffusion Parameters in Perovskite Solar Cells with Light Modulated Techniques. *ACS Energy Lett.*, **6** (6), 2248–2255.